UNIVERSITY OF CALIFORNIA
SANTA CRUZ

BLACK HOLES AND BUBBLES: A PHENOMENOLOGICAL, FORMAL, AND NUMERICAL EXPLORATION

A dissertation submitted in partial satisfaction of the
requirements for the degree of

DOCTOR OF PHILOSOPHY

in

PHYSICS

by

Evan Frangipane

September 2024

The Dissertation of Evan Frangipane
is approved:

Professor Anthony Aguirre, Chair

Professor Michael Dine

Professor Stefano Profumo

Peter Biehl
Vice Provost and Dean of Graduate Studies

Contents

List of Figures

List of Tables

Abstract

Black Holes and Bubbles:

A phenomenological, formal, and numerical exploration

by

Evan Frangipane

This thesis is a compilation of my work on the phenomenology and formal theory of black holes and numerical work on bubble dynamics. The first project is a novel search for primordial black holes (PBHs) with the Nancy Grace Roman Space Telescope. The next project is a study on the mystery of black hole evaporation in an explicitly defined spacetime. The final project is a numerical simulation of bubble dynamics in general relativity.

Acknowledgments

I want to thank my committee, collaborators, family, and friends.

The text of this thesis includes reprints of the following previously published material:

William DeRocco, Evan Frangipane, Nick Hamer, Stefano Profumo, Nolan Smyth. Revealing terrestrial-mass primordial black holes with the Nancy Grace Roman Space Telescope. Phys.Rev.D 109 (2024) 2, 023013.

Joseph Schindler, Evan Frangipane, Anthony Aguirre. Unitarity and the information problem in an explicit model of black hole evaporation. Class.Quant.Grav. 38 (2021) 7, 075025.

The co-authors listed in these publications directed and supervised the research which forms the basis for the thesis.

Chapter 1

Introduction

Research in black hole physics is a broad and rich discipline. During my years as a graduate student, I worked on a variety of aspects of the field, including phenomenology, formal theory, and numerical simulation. This thesis is a compilation of my work toward the understanding of black holes. This paper is divided into two parts with Part I on my work directly on black hole physics, and Part II on my work toward the goal of simulating black hole production via vacuum bubbles.

In Chapter 2, I will introduce a phenomenological study of primordial black holes. In Chapter 3, I will consider the black hole information paradox. In Chapter 4, I will explore a numerical simulation of Coleman DeLuccia bubbles to create black holes in an asymptotically FLRW spacetime. In Chapter 5, I will tie the parts together and conclude.

Part I

Black Holes

Chapter 2

Primordial Black Holes

2.1 Introduction

The nature of dark matter remains one of the most pressing open questions in fundamental physics. While multiple lines of compelling evidence indicate its existence, its microphysical nature remains unknown (for a recent review and up to date references see e.g. Chapter 27 of Ref. [273]). Many models have been proposed to explain this additional matter content, with many such models introducing new fundamental particles with suppressed interaction cross-sections to populate the dark sector [273]. However, dark matter may instead be macroscopic and potentially possess large interaction cross-sections, escaping detection due to its low number density. Primordial black holes (PBHs) are a well-motivated candidate for such a macroscopic dark matter model [55, 56, 58, 126]. There are a wide variety of mechanisms that result in the formation of PBHs, from the collapse of overdensities sourced by inflation [58, 129] to phase transi-

tions [161] and topological defect collapse [71] in the early universe (see the discussion in Sec. 2.3.1 below). PBHs may form over a wide range of masses, from as low as asteroid masses up to thousands of solar masses and beyond.

The Earth-mass range, $\sim 10^{-6}\,M_{\odot}$, is of particular interest, as observations of excess short-duration microlensing events have been suggested to constitute a first hint of a population of PBHs at terrestrial masses [214]. However, there is another possible candidate to explain these events: free-floating planets (FFPs). These are planets that have been ejected from their parent star system by dynamical interactions during the chaotic early phases of system formation. Such FFPs are expected to dramatically outnumber bound exoplanets at sub-terrestrial masses [254, 257], constituting a large potential background for surveys seeking to observe PBHs at Earth masses and below.

Previously, constraints on the PBH abundance have been placed in regions of parameter space for which the expected contribution from FFPs is negligible. However, with the upcoming launch of the Nancy Grace Roman Space Telescope, this will change: over the course of its Galactic Bulge Time Domain Survey (GBTDS) [107], Roman is expected to observe hundreds of free-floating planets at roughly Mars mass and above [157]. This unprecedented sensitivity will also provide the opportunity to search for PBHs in new regions of parameter space. In these regions, FFPs constitute an irreducible background that must be taken into account in order to constrain or claim the discovery of PBHs.

FFPs and PBHs cannot generally be discriminated on an event-by-event basis, as their light curves are degenerate for identical masses. However, FFPs and PBHs are

expected to arise from different underlying mass distributions, permitting a statistical means of discrimination. In this chapter, we present a method by which a subpopulation of PBHs can be detected amidst a background of FFPs. We find that even in the presence of FFPs, Roman will be sensitive to PBHs at abundances well below existing constraints. In particular, Roman will be able to conclusively determine the nature of the Earth-mass "hint" of a PBH population claimed by [214].

The remainder of the Chapter is organized as follows. In Sec. 2.2, we discuss microlensing surveys and describe the observables associated with microlensing lightcurves. In Sec. 2.3, we review mechanisms for PBH/FFP formation and provide a fiducial mass function for the abundance of each population. In Sec. 2.4, we describe the implementation of our analysis framework and the associated statistical methodology for estimating Roman sensitivity. In Sec. 2.5, we present our results and discuss their implications before concluding in Sec. 2.6.

2.2 Microlensing

Gravitational lensing is a powerful technique to observe non-luminous massive objects at astronomical distances. Light rays passing in the vicinity of a massive object are bent by the gravitational field of the object, causing the light from background stars ("sources") to be distorted by massive objects ("lenses") that lie along the line of sight. For high mass lenses, this effect produces multiple images of the source; for low mass lenses, the images cannot be individually resolved and instead contribute to an overall

apparent magnification of the source. This effect is known as microlensing [219].

The duration and magnification of the source are determined by the mass of lens M, the distance to the lens and source, d_L and d_S, the relative proper motion of the source and the lens $\mu_{\rm rel}$, the impact parameter u, the angular diameter of the source θ_S, and the effective angular diameter of the lens θ_E. This final quantity is also known as the "Einstein angle" and is given by

$$\theta_E = \sqrt{\frac{4GM(1 - d_L/d_S)}{c^2 d_L}}. \tag{2.1}$$

When $\theta_S \ll \theta_E$, the angular extent of the source is negligible. This "point-source regime" is typical for large lens masses and distant sources, and the associated event duration is given by the time it takes for the source to cross the Einstein radius of the lens. This "Einstein crossing time" is defined as

$$t_E = \frac{\theta_E}{\mu_{\rm rel}}. \tag{2.2}$$

In the point-source regime, the apparent magnification is given by [211]

$$A_{\rm ps}(u) = \frac{u^2 + 2}{u\sqrt{u^2 + 4}}, \tag{2.3}$$

where $u \equiv u(t)$ is the impact parameter as a function of time. This yields a characteristic light curve consisting of a narrow peak.

When $\theta_S \gtrsim \theta_E$, however, the point-source approximation breaks down. In

this finite-source regime, the light curve saturates at a lower maximum magnification and the event duration is no longer set by t_E, but rather by the time for the *lens* to cross the finite angular extent of the *source*, a timescale of $\sim 2\theta_S/\mu_{\rm rel}$. Similarly, the magnification in this regime no longer diverges as $u \to 0$ and is instead given by an integral over the source disk, specified in polar coordinates (r, ϕ) as [192, 256, 272]

$$A_{\rm finite}(u, \rho) \equiv \frac{1}{\pi\rho^2} \int_0^{\rho} dr \int_0^{2\pi} d\phi \; r \; A_{\rm ps}\Big(\sqrt{r^2 + u^2 - 2ur\cos(\phi)}\Big), \tag{2.4}$$

where $\rho \equiv \theta_S/\theta_E$ and the origin has been chosen such that the lens center is located at a distance u from the origin along $\phi = 0$. The maximum impact parameter that produces a detectable event is defined implicitly via the relation $A_{\rm finite}(u_{\rm T}, \rho) = A_T$, where the minimum detectable magnification, A_T, is set by the photometric sensitivity of the microlensing survey, and u_T is the maximal impact parameter that results in a magnification of at least A_T. u_T defines the phase space for the expected event rate calculation (see Sec. 2.4.1) and can be calculated for a given d_L, d_S, and θ_S following the procedure given in [256].

For most events, the fundamental observable that can be measured from the light curve is the duration. We define this as the time over which the magnification is above detection threshold ($A > A_T$ or equivalently $u < u_T$):

$$t_{\rm dur} = 2\sqrt{u_T^2 - u_{\rm min}^2}\,\frac{\theta_E}{\mu_{\rm rel}}, \tag{2.5}$$

where $u_{\rm min}$ is the impact parameter at the point of closest approach. Assuming perfect photometry, $u_T \approx \rho$ in the extreme finite-source regime and ≈ 1 in the point-source regime; hence, for a trajectory that passes through the midplane of the source, $t_{\rm dur}$ approaches the expected $\sim 2\theta_S/\mu_{\rm rel}$ in the finite-source limit and $\sim 2t_E$ in the point-source regime.

Though finite-source effects reduce the peak magnification, which can reduce detectability, they introduce characteristic features in the light-curve that permit a measurement of θ_E. Coupled with a measurement of the lens distance, an estimate of the lens mass can be made. However, the extraction of θ_E is a challenge for many events, especially those that do not conform to simple single-lens models. Additionally, for low masses and short event durations, estimating d_L requires a simultaneous observation by another telescope in order to provide a parallax measurement, which is often unavailable. As such, the only observable quantity that can be robustly measured for most microlensing events is the event duration, $t_{\rm dur}$, and is therefore the quantity we choose to employ to discriminate amongst various subpopulations of lenses in Sec. 2.4.

2.3 Microlensing Targets

In this section, we discuss two primary targets for microlensing surveys in the terrestrial mass range and connect them to existing observations.

2.3.1 Primordial black holes

Black holes not originating from the collapse of massive stars are generically termed "primordial" black holes and appear in many extensions of the Standard Model. Most formation mechanisms rely upon the growth of large density fluctuations in the early universe that ultimately collapse. These may be seeded by features in the inflationary potential [21, 59, 101, 110, 138, 149, 277] or by other physical processes, such as the collapse of inhomogeneities during the matter-dominated era triggered by a sudden pressure reduction [47, 151, 161], collapse of cosmic string loops [127, 137, 150], bubble collisions [71, 172], a scalar condensate collapsing to Q-balls before decay [67–70], or domain walls [77, 109, 180, 235]. (See, e.g., [55, 56] for recent reviews.)

If the overdensities are seeded by inflationary features, the resulting PBH masses are related to the redshift of formation since PBHs acquire a mass of order the total energy within a Hubble volume at the time of collapse. The resulting mass distribution is often well-described by a log-normal distribution, which is a generic prediction for PBHs forming from smooth, symmetric peaks in the power spectrum of density fluctuations in the early universe [84]. Numerical and analytical evidence for this functional form was provided in [121] and [158], see also the recent Ref. [166]. For this reason, in the following, we will consider a fiducial PBH mass function of the form

$$f(M, \sigma, M_c) = \frac{f_{\rm PBH}}{\left(\sqrt{2\pi}\right)\sigma M} \exp\left(-\frac{\log^2\left(M/M_c\right)}{2\sigma^2}\right), \tag{2.6}$$

normalized such that

$$f_{\rm PBH} = \frac{\Omega_{\rm PBH}}{\Omega_{\rm DM}} = \int \mathrm{d}M f(M, \sigma, M_c) \tag{2.7}$$

where here $\Omega_{\rm PBH}$ and $\Omega_{\rm DM}$ are the fractional energy density of PBHs and of all dark matter, respectively. Here M_c is the mean value of M and σ is the standard deviation of the logarithmic mass.

PBHs are a compelling candidate for dark matter and have been searched for across a wide range of masses. In the mass range of $\approx 10^{-11}\,M_\odot - 10\,M_\odot$, gravitational lensing sets some of the strongest observational constraints on their abundance [10, 11, 51, 122, 159, 214, 275, 276] limiting the fractional energy density to $f_{\rm PBH} \approx 10^{-1} - 10^{-2}$. At terrestrial masses, the strongest limits are set by observations made by the Optical Gravitational Lensing Experiment (OGLE) [214]. However, this survey also revealed an anomalous excess of six short-duration events consistent with a population of Earth-mass PBHs at $f \approx 10^{-2}$. To date, the nature of these observations has not been resolved. As we will show in Sec. 2.5, upcoming observations by the Nancy Grace Roman Space Telescope will be able to establish whether a population of PBHs truly exists at these masses or whether these events were more likely caused by, e.g., free-floating planets.

2.3.2 Free-floating planets

The term "free-floating planets" is often used to describe two different classes of astrophysical objects. At masses near and above that of Jupiter, FFPs may form *in*

situ as the core of a failed star [199]. At lower masses, FFPs are expected to primarily form within young planetary systems before being ejected by dynamical processes onto unbound orbits. There is a wide variety of processes that can result in the ejection of a protoplanetary object, including stripping by nearby stars, gravitational scattering off of planetesimals, and interactions with an inner binary star system [94, 187, 232]. Both simulations and observations suggest that FFPs may dramatically outnumber bound planets at masses $\lesssim M_\oplus$ [204, 254, 257]. FFPs are therefore an exciting observational target for existing and upcoming microlensing surveys.

Ejection processes typically yield a distribution of FFPs that are well-described by a power law [204]. Here we adopt the form

$$\frac{dN}{d\log_{10}(M)} = \mathcal{N}\Big(\frac{M}{M_{\rm norm}}\Big)^{-p} \tag{2.8}$$

where $\mathcal{N}$ is the total number of FFPs per star at mass M scaled by a normalization mass $M_{\rm norm}$. Throughout the rest of the chapter, we take all logarithms to be base 10 and $M_{\rm norm} = M_\oplus$ unless otherwise noted.

At present, observational measurements of the FFP population do not place strong constraints on the values of $\mathcal{N}$ and p. Existing microlensing surveys have observed tens of FFPs, with only three events permitting a mass estimate placing the lens in the terrestrial range.[1] Based off these data, combined with the results from simulations of ejection [83, 106, 201] and observations of bound systems [174, 245, 254], the best

[1]The associated events are OGLE-2012-BLG-1323 [207], OGLE-2016-BLG-1928 [209], and MOA-9y-5919 [170].

estimates for p and $\mathcal{N}$ are of order $p \approx 1$ and $\mathcal{N} \approx 10$ with an uncertainty spanning $p \approx 0.66 - 1.33$ and $\mathcal{N} \approx 2 - 20$ [118, 204, 257]. We choose to adopt $p = 1$ and $\mathcal{N} = 10$ as our fiducial parameters and marginalize over the uncertainty on their values when computing our sensitivity (see Sec. 2.4.2).

2.4 Detecting PBHs with Roman

In this section, we describe our statistical methodology for detecting a subpopulation of PBH lenses within a background of FFPs. The key point is that though PBH and FFP events cannot be discriminated on an event-by-event basis, the two *populations* can be distinguished by the statistical distribution of their event durations, $t_{\rm dur}$ (Eq. 2.5). This distribution is predominantly controlled by the underlying mass function of the lensing population, which differs significantly between FFPs and PBHs (see Secs. 2.3.1 and 2.3.2). Additionally, the $t_{\rm dur}$ distribution is influenced by the distribution of lens distances and transverse velocities, both of which differ between FFPs and PBHs as well (see Sec. 2.4.1). As a result, the observed distribution of $t_{\rm dur}$ provides a robust means of identifying multiple populations of lenses within a set of microlensing events.[2]

While existing observations have not yet yielded a sufficient number of detections at terrestrial masses to resolve the underlying distribution of $t_{\rm dur}$, this will change in the coming years. The Galactic Bulge Time Domain Survey (GBTDS), one of three primary surveys to be conducted by the upcoming Nancy Grace Roman Space Telescope

[2] An alternate strategy, as suggested by Niikura et al. [214], would be to observe along different lines of sight, as FFPs and PBHs are expected to follow different spatial distributions. As this would require an additional dedicated survey, we leave the study of this topic to future work.

(set to launch in 2027), will observe seven fields tiling 2 square degrees of the Galactic bulge with a cadence of 15 minutes during six 72-day observing seasons [107]. This survey strategy has been designed specifically to meet core science requirements for the mission, including measuring the abundance of free-floating planets to within 25%. As such, the GBTDS is expected to yield hundreds of FFP microlensing events at Mars mass and above [157], providing the opportunity for distribution-level analyses.

In the following two subsections, we will describe our methodology for determining Roman's sensitivity to discriminating a PBH subpopulation from a background FFP population using the observed distribution of $t_{\rm dur}$ values. This is done in two steps. First, in Sec. 2.4.1, we compute the event rate for both of these populations given Roman's fiducial survey parameters to determine the $t_{\rm dur}$ distribution for both populations. Then, in Sec. 2.4.2, we perform a 2-Sample Anderson-Darling test to determine the statistical significance at which a combined FFP and PBH $t_{\rm dur}$ distribution differs from a FFP distribution without PBHs.

2.4.1 Event rate estimation

The key input to our statistical methodology is the distribution of event durations, $t_{\rm dur}$. In order to compute this, we integrate over the differential event rate given by [27, 213]

$$\frac{d\Gamma}{dM\, dd_L\, dt_{\rm dur}\, du_{\rm min}} = \frac{2}{\sqrt{u_T^2 - u_{\rm min}^2}} \frac{v_T^4}{v_c^2} \exp\Big[-\frac{v_T^2}{v_c^2}\Big] \frac{\rho_M}{M} f(M) \varepsilon(t_{\rm dur}), \tag{2.9}$$

where $f(M)$ is the probability distribution of lens masses (Eq. 2.6 or Eq. 2.8 for PBHs and FFPs, respectively), ρ_M is the mass density of the lens population, $\varepsilon(t_{\rm dur})$ is the detection efficiency, and v_T, the transverse velocity, is given by

$$v_T = 2\theta_E d_L \sqrt{u_T^2 - u_{\rm min}^2}/t_{\rm dur}. \tag{2.10}$$

We set u_T, the maximum impact parameter that produces a detectable event, according to the procedure discussed in Sec. 2.2, adopting $A_T = 1.34$ as our fiducial threshold magnification. This choice likely underestimates Roman's sensitivity, but is in keeping with the literature [157] (see also App. 2.A). The event rate, Γ, is then evaluated as

$$\Gamma = 2\int_{M_{\rm min}}^{M_{\rm max}} dM \int_0^{d_s} dd_L \int_0^{u_T} du_{\rm min} \int_{t_{\rm min}}^{t_{\rm max}} dt_{\rm dur} \frac{1}{\sqrt{u_T^2 - u_{\rm min}^2}} \frac{v_T^4}{v_c^2} \exp\Big[-\frac{v_T^2}{v_c^2}\Big] \frac{\rho_M}{M} f(M)\varepsilon(t_{\rm dur}), \tag{2.11}$$

which we calculate using `LensCalcPy`,[3] a package to semi-analytically calculate microlensing observables. We take $t_{\rm min}$ to be 15 min and $t_{\rm max}$ to be 6×72 days, corresponding to the proposed cadence and observational duration of the Roman GBTDS. By performing the integral and multiplying the resulting rate by the GBTDS observational duration, we compute the expected total number of events that Roman will detect, denoted $N_{\rm FFP}$ and $N_{\rm PBH}$ for FFPs and PBHs, respectively.

[3] https://github.com/NolanSmyth/LensCalcPy

In computing the event rate, we must specify the velocity and spatial distributions of the lenses. We assume that the FFP density tracks the stellar distribution of the galaxy, for which we adopt the exponential Koshimoto parametric model described in [169]. We take the PBH mass distribution to be a Navarro-Frenk-White profile given by

$$\rho_M = \frac{\rho_0}{(\frac{r}{r_s})(1+\frac{r}{r_s})^2}, \tag{2.12}$$

where $\rho_0 = 4.88 \times 10^6\ M_\odot\ \mathrm{kpc}^{-3}$ and $r_s = 21.5$ kpc [167]. While the relative source-lens velocity depends in general on the positions of both source and lens, we take $v_c = 220$ km/s for PBHs and $v_c = 200$ km/s for FFPs. The former is a typical value for a virialized DM halo [167], and the latter is approximately the average transverse velocity in the stellar disk (see e.g. [214] for a more complete description). As the majority of sources are in the Galactic Bulge, finite-source effects imply that the low-mass lenses we consider must be sufficiently far from the source in order to be detectable, making this simplification appropriate for the scope of this work. Ultimately, our results are fairly insensitive to changes in these choices of parameters, as the dominant uncertainty in our analysis arises from the normalization of the FFP mass function (see Sec. 2.5). However, we have compared our yields to those computed by [157], which employ a different Galactic model and mass function, and find $\mathcal{O}(1)$ agreement (see App. 2.A).

For the mass function of PBHs, we assume a log-normal distribution (Eq. 2.6), while for FFPs, we adopt a power-law (Eq. 2.8) truncated at $M_{\mathrm{min}} = 10^{-13}\,M_\odot$ and $M_{\mathrm{max}} = 0.1\,M_\odot$ for computational purposes. These cutoffs have been chosen to lie well

outside the mass range of Roman's sensitivity ($\approx 10^{-8}\,M_\odot - 10^{-3}\,M_\odot$) and we have verified numerically that they do not have an effect on the results.

The resulting yields for PBHs and FFPs are shown in Figs. 2.1 and 2.2. Fig. 2.1 shows the number of PBH events Roman is expected to see during its proposed observational duration as a function of $M_{\rm PBH}$ for $f_{\rm PBH} = 1$. The various curves correspond to different widths of the log-normal distribution, σ. Note that a $f_{\rm PBH} = 1$ abundance has already been ruled out by other microlensing surveys, hence the yields in unconstrained parameter space are necessarily smaller than the values in Fig. 2.1. We see that in unconstrained parameter space ($f \lesssim 10^{-2}$), Roman is expected to observe up to $\approx 10^4$ PBH events.[4]

Fig. 2.2 shows the number of FFP events Roman is expected to see during its proposed observational duration as a function of p, the power-law index of the FFP mass distribution. The various curves correspond to various normalizations of the power law, with $\mathcal{N} = 10$ the fiducial value. The yield is only weakly-dependent on p, with our fiducial distribution yielding ≈ 400 events for a broad range of p.

2.4.2 Subpopulation identification

Our statistical analysis relies upon discriminating between $t_{\rm dur}$ distributions sourced by either purely FFPs or a combination of FFPs and PBHs. We will define the true distributions from which a particular set of detected events are sampled as

[4] We note that though distinguishing FFPs from PBHs requires a statistical characterization when the observed yields of each are comparable, there are regions of parameter space in which PBH observations would well exceed the expected FFP yield, hence an identification of this population would be much simpler. Interestingly, this includes the parameter space in which PBHs explain the short-duration OGLE events, making their interpretation as FFPs more challenging.

$\mathcal{T}_{\rm dur}^{\rm FFP}$ and $\mathcal{T}_{\rm dur}^{\rm FFP+PBH}$. These distributions depend on a complex combination of several input parameters, including the power-law index of FFPs (p), the central mass of the PBH distribution ($M_{\rm PBH}$), and the overall number of observed FFPs and PBHs ($N_{\rm FFP}$ and $N_{\rm PBH}$). As such, they cannot be computed in a closed analytic form. We therefore choose to employ a test that discriminates based purely on empirical distribution functions without relying on an underlying analytic background model. The two-sample Anderson-Darling (AD) test is an effective choice for this situation[5], as it is non-parameteric, hence requires no model input, and outperforms the Komolgorov-Smirnov test in the amount of data required for significance, see [89].

The AD test computes the significance at which two test distributions are sampled from the same underlying distribution. Given two distributions of size m, n sampled from the true distributions $\mathcal{T}_{\rm dur}^{\rm FFP}$ and $\mathcal{T}_{\rm dur}^{\rm FFP+PBH}$, we construct two empirical distribution functions, denoted $\mathcal{T}_{{\rm dur},m}^{\rm FFP}$ and $\mathcal{T}_{{\rm dur},n}^{\rm FFP+PBH}$, respectively. In the context of our analysis, $m = N_{\rm FFP}$ and $n = N_{\rm FFP} + N_{\rm PBH}$, where $N_{\rm FFP}$ and $N_{\rm PBH}$ are calculated as described in the previous subsection. In terms of these empirical distribution functions, the AD test statistic can be written as [242]:

$$A_{mn}^2 = \frac{mn}{N} \int_{-\infty}^{\infty} \frac{(\mathcal{T}_{{\rm dur},m}^{\rm FFP} - \mathcal{T}_{{\rm dur},n}^{\rm FFP+PBH})^2}{\mathcal{K}_N(1-\mathcal{K}_N)}\, d\mathcal{K}_N \tag{2.13}$$

[5]In practice, Roman will likely perform a Bayesian analysis to estimate the parameters controlling the lens distribution, which will be more sensitive than the methodology we employ here. However, the AD test provides a robust, if conservative, estimate of Roman's sensitivity.

where

$$\mathcal{K}_N = \frac{1}{N}(m\mathcal{T}_{\mathrm{dur},m}^{\mathrm{FFP}} + n\mathcal{T}_{\mathrm{dur},n}^{\mathrm{FFP+PBH}}) \tag{2.14}$$

and $N \equiv m + n$. Note that by performing this test, we do not necessarily learn the PBH mass or abundance; merely that the distributions are separable.

To determine the sensitivity, we fix $\mathcal{N}$, p, M_{PBH}, and σ and allow $r \equiv N_{\mathrm{PBH}}/N_{\mathrm{FFP}}$ to vary. We set our limit at the value of r such that the AD test rejects the null hypothesis (i.e. both distributions are sampled from a pure FFP distribution) at 95% confidence. Representative examples of distributions that are distinguishable and indistinguishable by the AD test are displayed in Figs. 2.3 and 2.4, respectively. In Fig. 2.3, the PBH distribution peaks at t_{dur} values well above the majority of FFPs, hence is readily distinguishable. In Fig. 2.4, despite having the same number of observed FFPs and PBHs as in Fig. 2.3, the two peaks overlap and the PBH population cannot be discriminated from background.

The weakness of this test is that in the low-statistics regime, two distributions may appear to have been drawn from different underlying distributions purely due to random fluctuations. In order to mitigate this effect, we perform our analysis 10 times and take the mean of the results, which we have verified numerically is sufficient for suppressing statistical fluctuation throughout our parameter space.

The analysis described above solely sets a limit on r, the *ratio* of observed PBH yield to FFP yield. In order to connect this to a physical density, we must calculate these yields. To do so, we employ `LensCalcPy` and produce two reference yield curves.

The first is the expected yield of observable PBHs as a function of $M_{\rm PBH}$ for $f_{\rm PBH} = 1$, which we denote $N_{\rm PBH}^{f=1}(M_{\rm PBH})$ and appears in Fig. 2.1. The second is the expected yield of observable FFPs for $\mathcal{N} = 10$ as a function of p, which we denote $N_{\rm FFP}^{\mathcal{N}=10}(p)$ and appears in Fig. 2.2. The $f_{\rm PBH}$ corresponding to a particular r is therefore simply given by $f_{\rm PBH}(M_{\rm PBH}, p) = r \times [N_{\rm FFP}^{\mathcal{N}=10}(p)/N_{\rm PBH}^{f=1}(M_{\rm PBH})]$.

Our results depend implicitly on $\mathcal{N}$ and p, the true values of which are unknown. Existing observations suggest possible values in the range $p \approx 0.66 - 1.33$ and $\mathcal{N} \approx 2-20$ [117, 157, 204, 257]. We therefore choose to marginalize over this uncertainty by determining, for a given $M_{\rm PBH}$ and σ, the $p \in [0.66, 1.33]$ for which our analysis is weakest and adopting the corresponding $f_{\rm PBH}$ as our limit. To capture the uncertainty on $\mathcal{N}$, we choose to display three results: our fiducial results ($\mathcal{N} = 10$), as well as results in which $\mathcal{N}$ has been taken to be larger/smaller than our fiducial value by an order of magnitude. This likely dramatically overestimates the uncertainty on this parameter given current constraints. However, by adopting this range, we encapsulate both the intrinsic uncertainty on its value as well as the uncertainty induced by our Galactic model (see App. 2.A).

2.5 Results

We display our ultimate sensitivity curves in Fig. 2.5. Existing constraints are shown in gray [160]. Additionally, we have included a dotted region ("OGLE hint") corresponding to the parameter space in which the short-timescale events observed by

OGLE can be explained by a population of PBHs [214]. The solid curves correspond to a fiducial FFP normalization of $\mathcal{N} = 10$ and varying width of the log-normal PBH distribution, while the dashed and dot-dashed curves correspond to $\mathcal{N} = 1$ and 100, respectively for a monochromatic PBH mass distribution. As described in Sec. 2.4.2, these extreme values of $\mathcal{N}$ likely significantly overestimate the uncertainty on the FFP distribution, however, as can be seen in Fig. 2.5, even these variations only induce changes to the sensitivity at the sub-magnitude level. Note that the largest number density of FFPs corresponds to the *weakest* sensitivity, as a larger FFP yield requires a correspondingly larger PBH yield to achieve the same significance of discrimination. All curves displayed have been marginalized over p via the methodology described in 2.4.2.

Roman's sensitivity to identifying a subpopulation of PBHs peaks at $f_{\rm PBH} \sim 10^{-4}$ in the mass range $M_{\rm PBH} \approx 10^{-8}\,M_\odot - 10^{-6}\,M_\odot$. Both the location of this peak and the corresponding value of $f_{\rm PBH}$ can be understood simply. Since the number density of PBHs scales as $1/M_{\rm PBH}$ for fixed $f_{\rm PBH}$, the location of peak sensitivity corresponds to the lowest possible mass before finite-source effects reduce detectability. As discussed in Sec. 2.2, finite-source effects become relevant when $\theta_S \approx \theta_E$, a condition that can be rewritten in terms of mass to yield [80]

$$M_{\rm finite} \approx \frac{\theta_S^2 c^2 d_L}{4G(1-\frac{d_L}{d_S})}\Big(\frac{d_L}{d_S}\Big). \tag{2.15}$$

Assuming the source to have a radius comparable to that of the Sun and taking $d_S =$

8.5 kpc and $d_L = 7.0$ kpc as typical distances for lensing events in the Galactic Bulge, one finds $M_{\text{finite}} \approx 10^{-6} M_\odot$, which corresponds with the mass at which the sensitivity peaks in Fig. 2.5.

Similarly, f_{PBH} can be estimated at this peak. We find that at terrestrial masses, a PBH yield of roughly 10% N_{FFP} is sufficient to identify the PBH subpopulation. Figs. 2.1 and 2.2 show that Roman's expected yield for FFPs and PBHs (at $\mathcal{N} = 10$ and $f_{\text{PBH}} = 1$) are $\mathcal{O}(1000)$ and $\mathcal{O}(10^6)$, respectively. We therefore see immediately that $N_{\text{PBH}} \approx 10\% \, N_{\text{FFP}}$ corresponds to $f_{\text{PBH}} \sim 10^{-4}$, which matches onto the maximal sensitivity shown in Fig. 2.5.

In the region of peak sensitivity, we find that sensitivity weakens with increasing width of the log-normal PBH distribution. This is not due to the fact that broader PBH distributions appear more akin to the FFP power law, but rather because broadening the PBH distribution pushes PBHs outside the observable window and lowers the overall yield of observable PBH events. This can be seen in Fig. 2.1, where broadening the distribution causes a monotonic decrease in the number of detected events in the region of peak sensitivity.[6] For a fixed number of PBHs required for discrimination, this reduced detection rate must be compensated for by an increase in f_{PBH}.

The small decrease in sensitivity at $M_{\text{PBH}} \approx 10^{-7} \, M_\odot$ is due to the peak of the PBH t_{dur} distribution coinciding with the peak of the FFP t_{dur} distribution, as can be seen in Fig. 2.4. At slightly higher and lower M_{PBH}, the two distributions peak at slightly different t_{dur}, improving sensitivity. However, this effect is small, as the

[6] Note that well outside this region, the opposite effect can actually improve sensitivity marginally for broad distributions by pushing events into the observable window.

sensitivity is predominantly governed by the PBH yield, which decreases rapidly at masses much above $10^{-6}\,M_\odot$ and below $10^{-8}\,M_\odot$.

In summary, our results show that even under conservative assumptions about Roman's detection threshold (Sec. 2.4.1) and the underlying background of FFPs (Sec 2.4.2), the Galactic Bulge Time Domain Survey will be highly sensitive to detecting a population of PBHs in new regions of parameter space. Excitingly, these regions include the parameter space in which existing short-timescale events have been suggested to hint at a subpopulation of PBHs at terrestrial masses [214]. Roman is therefore poised not only to make the first precise measurements of the FFP mass distribution, but to possibly uncover a subpopulation of PBHs lying within it as well.

2.6 Discussion

The launch of the Nancy Grace Roman Space Telescope will open a new window into low-mass astrophysical bodies. Though its Galactic Bulge Time Domain Survey targets bound and unbound exoplanets, we have shown that it will have unprecedented sensitivity to physics beyond the Standard Model as well. In particular, it will probe the fraction of dark matter composed of primordial black holes at abundances as low as $f_{\rm PBH} \approx 10^{-4}$ at PBH masses of roughly $10^{-6}\,M_\odot$, with a sensitivity that decreases as $\approx M_{\rm PBH}^{1/3}$ towards higher masses. Its region of sensitivity extends up to three orders of magnitude below existing constraints. This region fully encompasses the parameter space in which an excess of short-duration microlensing events observed by

OGLE have been suggested to hint at a population of PBHs [214]. Therefore, Roman will conclusively determine the nature of these events, whether it be rogue worlds or our first glimpse of what lies on the dark side of the universe.

2.A Comparison of Estimated Yields

In this Appendix, we compare the fiducial FFP yield calculated in our analysis to that of [157]. The authors of [157] calculate their expected FFP yield for the Roman GBTDS using the code *Gravitational microlensing Using Large Lensed Sources* (GULLS) [226]. GULLS draws explicit sources and lenses from a Bescançon galactic model (version 1106 [95]) and simulates individual microlensing events by generating realistic photometry using synthetic images. This approach is significantly different from the semi-analytic approach we employ in our work. `LensCalcPy`, the code used to compute our FFP yields, is designed to provide simple estimates of lensing event rates, not to model individual events or generate associated photometry. However, its speed and flexibility makes it well-suited to population-level studies with large numbers of events.

While our approach and that of [157] differ significantly in implementation, we find that they produce very similar ultimate FFP yields. In order to see this, we compare to Table 2 of [157], where the authors have displayed their fiducial FFP yield for a log-uniform mass distribution ($\frac{dN}{d\log M} = 1$ dex^{-1}) as a function of FFP mass. Performing the equivalent analysis with `LensCalcPy` and adopting the normalization of

1 dex^{-1} results in the yields shown in Table 2.1. We see that at masses $> M_{\oplus}$, our yields differ from those of [157] by less than a factor of two. At lower masses, the discrepancy between the approaches grows, reaching a value of ≈ 6 at the lowest observable masses.

Table 2.1: FFP yield comparison for Log-Uniform Mass distribution

Mass ($M_{\oplus}$)	**Johnson et al.** [157]	**This work**
0.01	0.31	0.05
0.1	4.49	1.75
1	22.1	19.0
10	87.1	72.6
100	313	234
1000	1025	744
10,000	3300	2370

We see that our results tend to underestimate the total FFP yield compared to GULLS, particularly for low-mass objects. A primary source of this discrepancy stems from differences between the definition of maximum detectable impact parameter in the two analyses, which we compare in Fig. 2.6. In [157], $u_{\rm min}$ is drawn uniformly from $[0, \max(1, 2\rho)]$ when generating an event. This effectively sets

$$u_T = \begin{cases} 1 & \rho < 0.5 \text{ (point-source regime)} \\ 2\rho & \rho > 0.5 \text{ (finite-source regime)} \end{cases} \tag{2.16}$$

resulting in the orange curve shown in Fig. 2.6. As described in Sec. 2.4.1, in our analysis, we instead determine the maximal impact parameter by solving the implicit equation $A_{\rm finite}(u_T, \rho) = A_T$. This yields the blue curve in Fig. 2.6. We choose to adopt $A_T = 1.34$ as our fiducial threshold throughout our analysis. This agrees with [157] in the point-source regime, however in the finite-source regime (which is most relevant for

low-mass objects), their approach yields generically larger values of u_T than ours, as can be seen in Fig. 2.6. Thus, their effective threshold magnification is < 1.34, resulting in the increased yields at low masses seen in Table 2.1. While we have chosen to use $A_T = 1.34$ throughout our analysis, this is likely an underestimate of Roman's ultimate detection threshold, which has been suggested to reach values of $\lesssim 1\%$ increases in flux for sufficiently bright sources [157]. We therefore note that depending on the photometric sensitivity achieved by Roman, our current yield predictions may underestimate the number of detected FFP events. This uncertainty is, however, encapsulated by the range of normalizations in the mass functions considered and thus in the curves shown in Figure 2.5.

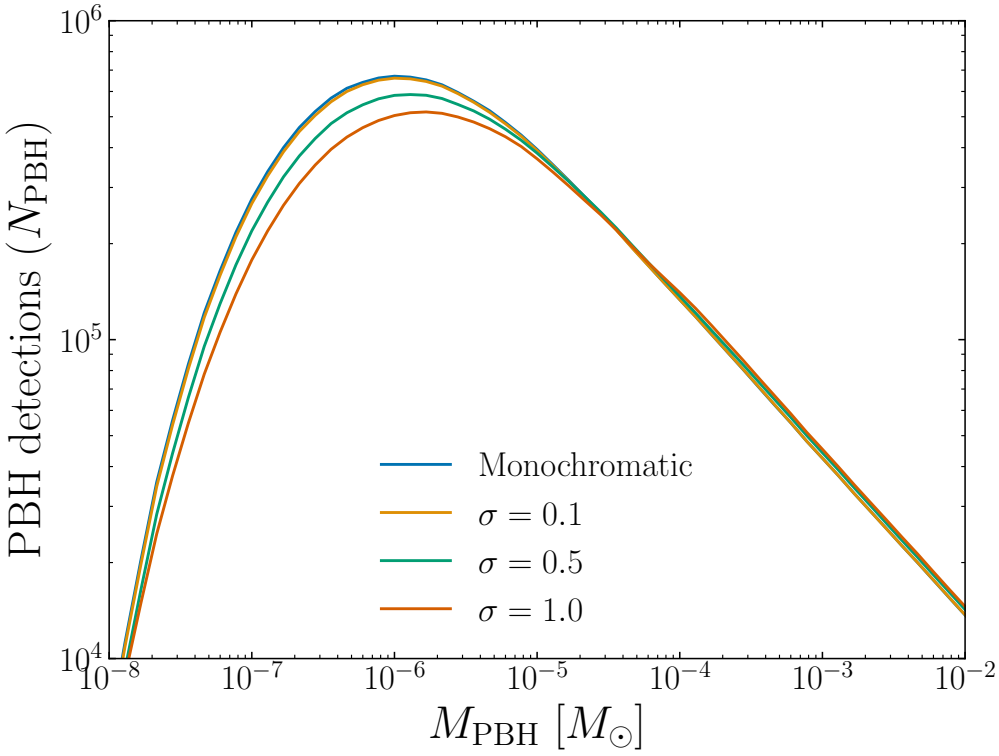

Figure 2.1: The total number of PBH microlensing events detectable by Roman for $f_{\rm PBH} = 1$ as a function of $M_{\rm PBH}$. The different curves correspond to different widths of the PBH mass distribution (see Sec. 2.3.1).

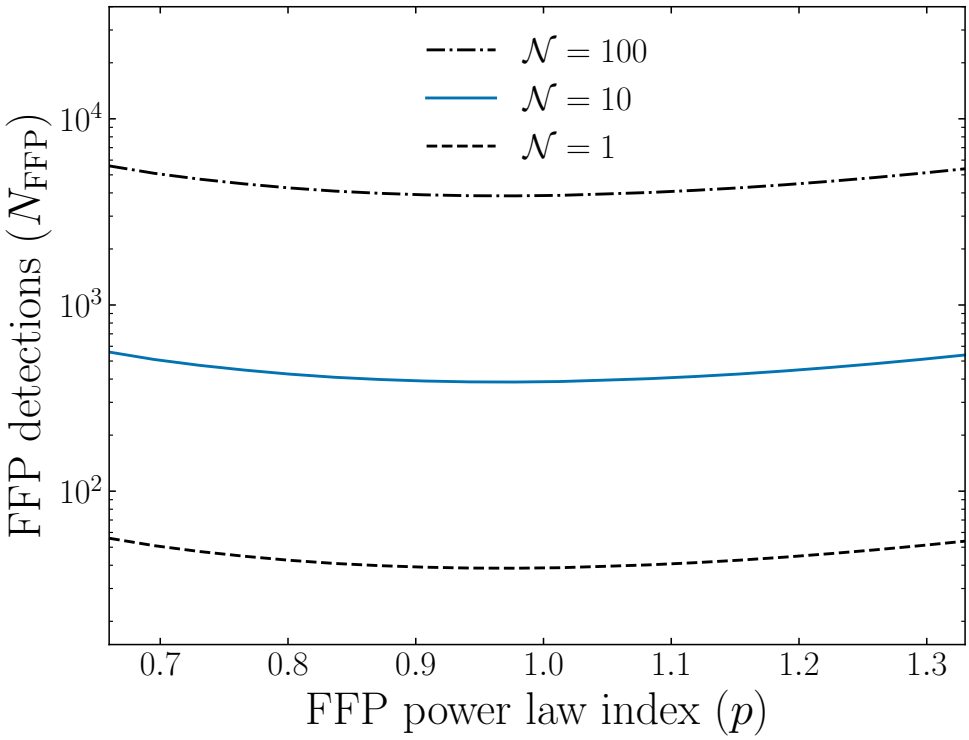

Figure 2.2: The total number of FFP microlensing events detectable by Roman as a function of p. The fiducial normalization $\mathcal{N} = 10$ is shown as a solid blue line, with $\mathcal{N} = 1$ and 100 shown as dashed and dash-dotted curves, respectively.

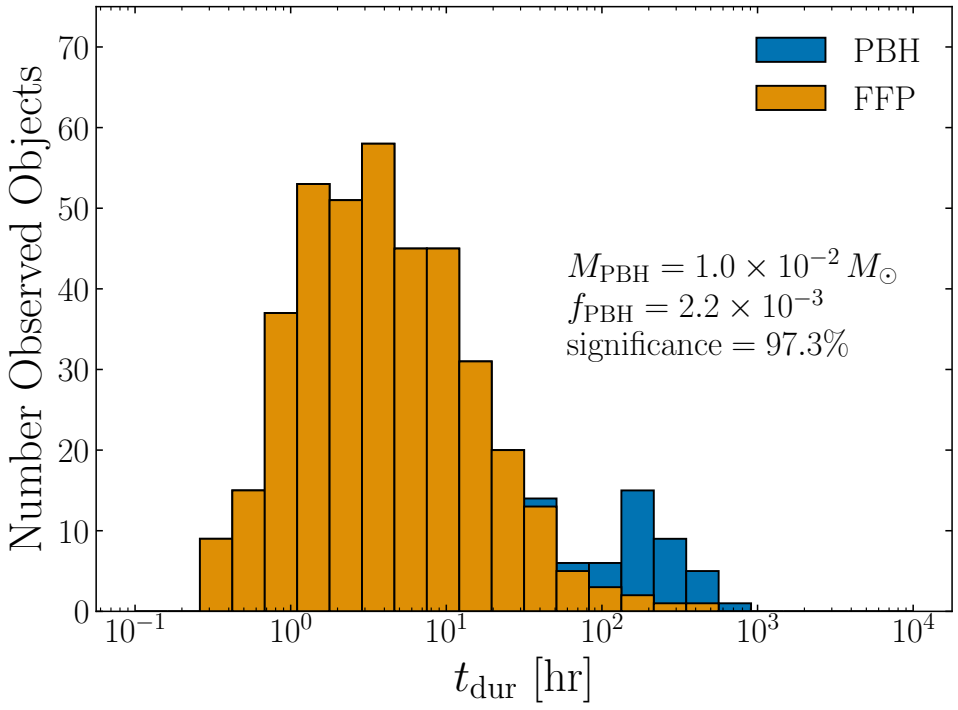

Figure 2.3: A stacked histogram of FFP and FFP+PBH distributions that are *distinguishable* at 95% confidence. These distributions correspond to parameter values of $\mathcal{N} = 10$, $p = 1.0$. The associated observable yields at this point in parameter space are $N_{\rm FFP} = 389$, $N_{\rm PBH} = 8\%\ N_{\rm FFP}$.

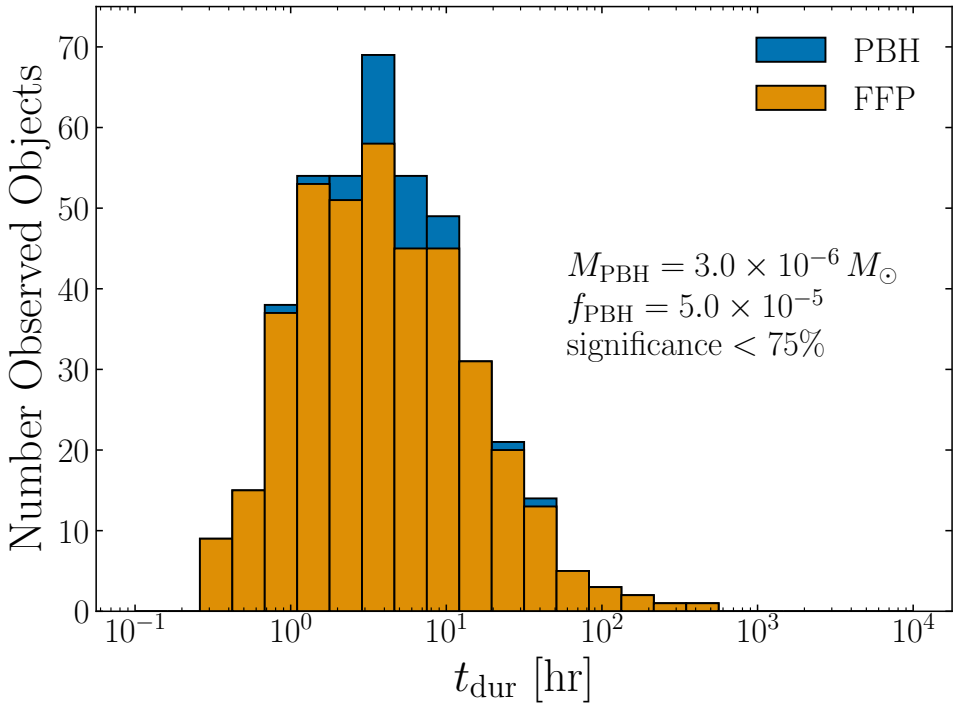

Figure 2.4: A stacked histogram of FFP and FFP+PBH distributions that are *indistinguishable* at 95% confidence. These distributions correspond to parameter values of $\mathcal{N} = 10$, $p = 1.0$. These parameters were chosen to yield the same observable yields as Fig. 2.3, $N_{\rm FFP} = 389$, $N_{\rm PBH} = 8\%\ N_{\rm FFP}$, however with a different location of the PBH peak.

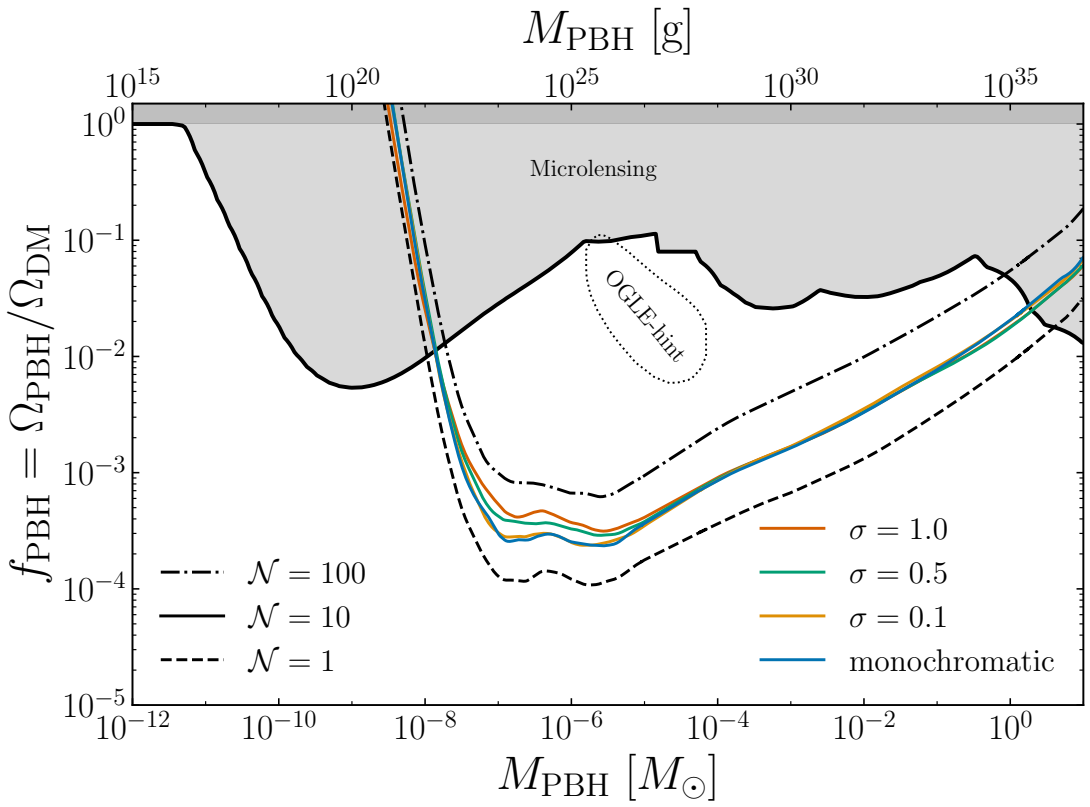

Figure 2.5: Roman sensitivity to detecting a population of PBHs in a background of FFPs. The solid curves correspond to $\mathcal{N} = 10$ and varying width σ of the log-normal PBH distribution, while the dashed and dot-dashed curves correspond to $\mathcal{N} = 1$ and 100, respectively. Existing constraints on the PBH abundance are shown in gray [160] and the region in which existing observations hint at a population of PBHs [214] is denoted "OGLE hint." See text for details.

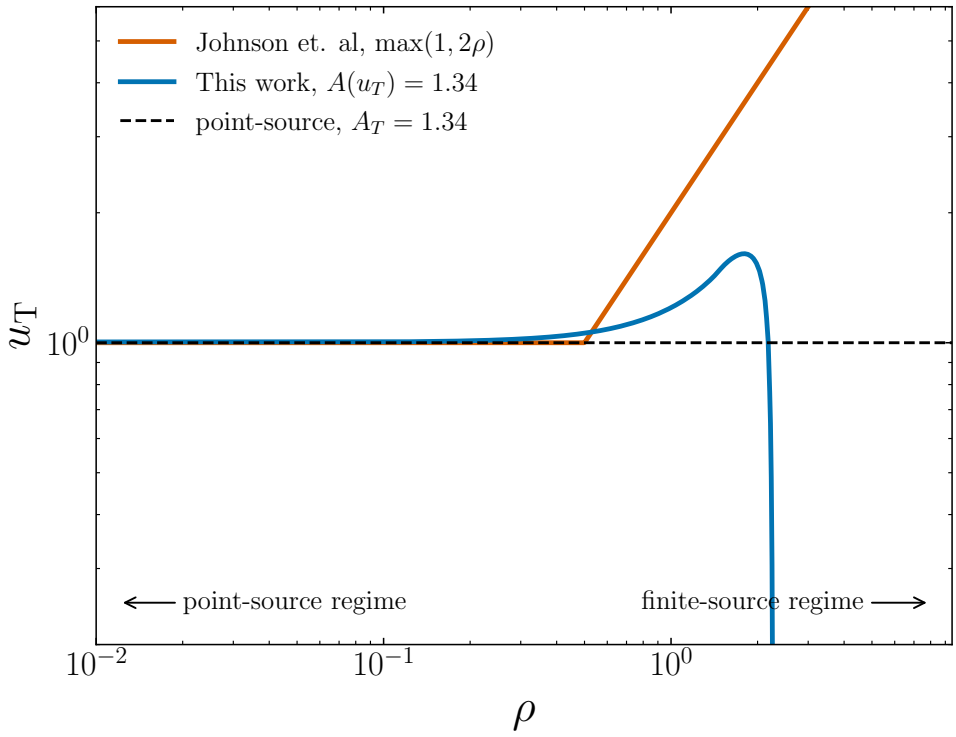

Figure 2.6: The threshold impact parameter as a function of $\rho = \theta_S/\theta_E$. The methodology of Johnson et al. [157] (orange) results in larger threshold impact parameters in the finite-source regime than our analysis (blue), increasing their relative yields.

Chapter 3

Black Hole Information

3.1 Introduction

Whether information is preserved or lost during black hole evaporation has now remained an unresolved question for several decades [9, 12–17, 19, 23, 24, 30, 34, 42, 46, 48, 53, 61–63, 99, 100, 108, 112–116, 123–125, 130–135, 142–145, 162, 171, 182, 185, 188–191, 197, 198, 216, 220–224, 227–229, 234, 236, 241, 251, 253, 255, 258, 259, 263, 270, 278]. At the center of this issue is the principle of unitarity.

The precise statement of this principle depends on how a system is described. At the level of semiclassical gravity, there must be unitary evolution between the state of quantum fields on a family of Cauchy surfaces Σ_u foliating some classical domain of dependence.[1] At the level of quantum gravity, there must be unitary evolution

[1] This form of unitarity holds by definition within a semiclassical theory, but is undefined when quantum gravity is not well described by a semiclassical approximation (*e.g.* due to correlations between matter and geometry). A semiclassical approximation is often used within standard discussions of black hole evaporation.

between states in some underlying Hilbert space $\mathcal{H}^{\text{QM}}$ from which spacetime and gravity may emerge. These statements are core principles of the quantum description of an information-preserving system, and we will assume them both to hold.

These core statements are not, however, the forms of "unitarity" usually invoked in relation to black hole information loss and the related firewall paradox. More commonly one asks:

- Is there a unitary scattering matrix from past to future null infinity?
- Is the Hawking radiation in a pure state when evaporation ends?
- Does the entropy of Hawking radiation decrease at late times during evaporation?

We call these the questions of "long term," "evaporation time," and "Page time" unitarity, respectively; they will be made precise later.

Each of these questions is traditionally framed, by definition, in the context of semiclassical gravity—that is, in terms of quantum fields on a classical background. One reason they are difficult to resolve is that, since black hole physics involves strong quantum gravity effects, it is not clear what background spacetime (if any) can be used to model the process.

Lacking a known semiclassical solution, assumptions about a background spacetime generally come in the form of Fig. 3.1. This diagram depicts a global causal structure and is useful for many purposes. Yet it is also problematic, in that it does not represent any particular physical model of the formation/evaporation process. For this reason it is difficult to make concrete statements about the geometry, and diagrams of

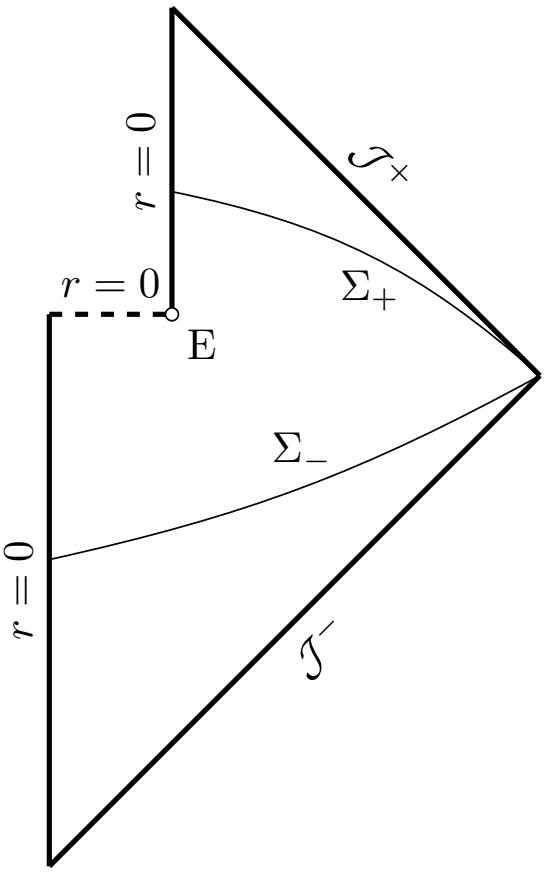

Figure 3.1: A Penrose diagram often associated with the process of black hole formation and evaporation.

this type are free to reflect biases of the artist.

In this article we will consider basic aspects of the black hole information problem, focusing on analyzing the various forms of "unitarity," in the context of a particular background model for an evaporating black hole. While not an exact semiclassical solution, this model is at least a concretely defined metric that is likely similar to one (see Sec. 3.3 for further discussion). Our hope is that framing these basic issues within a concretely defined context will help clarify their essential aspects, and provide a clearer

grounds to confirm or refute assumptions and results about the evaporation process.

Much of the content of the article is review presented in a somewhat pedagogical manner. This is intentional. Our view is that subtle differences in understanding about foundational assumptions of the theory can propagate misunderstanding about the information issue, and therefore that we should clarify the framework being used. In this direction we make a particular effort to be clear about what Hilbert spaces define the quantum theory, what decompositions of the total Hilbert space are used when, and precisely what is meant by "entropy of the black hole" in various circumstances.

In the course of reviewing the basic issues in this context, we draw some conclusions that are not yet as widely accepted in the literature as we think they should be. We will argue that even assuming the fundamental notions of semiclassical and quantum gravitational unitarity do both hold, the more common notions of long term, evaporation time, and Page time unitarity can nonetheless fail. And while long term unitarity may be restored by appealing to regular (nonsingular) black hole models, the latter two cannot. These failures are sometimes said to represent "information loss," but they in no way violate the underlying principles of unitarity.

An essential aspect of our arguments is the distinction between the semiclassical[2] Hilbert space $\mathcal{H}(\Sigma_u)$ and an underlying quantum gravitational Hilbert space $\mathcal{H}^{\rm QM}$. In particular we argue that the Page curve arises in the quantum gravitational Hilbert space, but not necessarily in the semiclassical one. In Sec. 3.7 we consider further how

[2]By "semiclassical Hilbert space" throughout the chapter, we really mean the Hilbert space of quantum field theory on the classical background $\mathcal{M}$ (of Sec. 3.3), which resembles but is not a solution of semiclassical gravity. The word semiclassical in this context denotes the space of quantum fields on a background metric, distinguishing this space from a truly quantum gravitational one.

these two levels of description are related, comparing our results to some recent results based on holography [13, 14, 224] and arguing that they are mutually compatible.

We are not the first to conclude that long term, evaporation time, and Page time "unitarity" can all be violated in a unitary theory, even if this conclusion has yet to be widely accepted in the literature. And discussions akin to ours have appeared before in various places [19, 100, 145, 234, 253, 263, 270]. The primary novelty of this work is its meticulous framing and detailed presentation in a new, explicitly defined, background. Given the persistent controversy surrounding these topics, we hope this can be a useful step towards consensus.

3.2 Quantum framework

3.2.1 Hilbert space of a partial Cauchy surface

The Hilbert space of a quantum field theory in curved spacetime is generally defined (taking Birrell and Davies [35] as a canonical reference) as a Fock space of mode solutions to the free part of the classical field equation [35, 36, 81, 111]. Here we will extend the standard formalism straightforwardly to consider partial (as opposed to global) Cauchy surfaces.

The basic approach is as follows. To each (orthonormal, positive frequency) complete set of classical modes ξ_k on (the domain of dependence of) a hypersurface Σ is associated a Fock space $\mathcal{H}_\xi(\Sigma)$ on which the quantum field theory can be defined. Given any two sets of modes ξ, ξ', complete on hypersurfaces Σ, Σ' respectively, we say

the Hilbert spaces

$$\mathcal{H}_\xi(\Sigma) \sim \mathcal{H}_{\xi'}(\Sigma') \tag{3.1}$$

are physically equivalent whenever the domains of dependence $D(\Sigma) = D(\Sigma')$ are equal. The space

$$\mathcal{H}(\Sigma) \tag{3.2}$$

is then defined as the equivalence class of all $\mathcal{H}_\xi(\Sigma)$. One expects unitary transformations between semiclassical Hilbert spaces only when they are physically equivalent.

The requirement that a set of modes defining the Hilbert space be complete is essential. For instance, the set of outgoing Hawking modes is not complete on any relevant Cauchy surface, and must be embedded within a larger set of modes when analyzing the final state.

Some parts of this construction (e.g. continuous tensor product below) are only mathematically well-defined after a UV or IR cutoff is included. We assume such cutoffs can be applied where necessary.

3.2.2 Hilbert space details

The Hilbert space construction outlined above is a simple formalization of (sometimes implicitly used) standard methods. Nonetheless, we elaborate the details here for maximal clarity. For concreteness, consider the matter action

$$S = \tfrac{1}{2} \int d^4x \sqrt{|g|}\, \partial_\mu \phi\, \partial^\mu \phi \tag{3.3}$$

defining a free real massless scalar field.

Consider a spatial hypersurface Σ in spacetime, which is a Cauchy surface for its domain of dependence $D(\Sigma)$ (which may or may not be the entire spacetime).

Let ξ_k denote an orthonormal complete set of positive frequency modes[3] on Σ. To each mode are associated creation and annihilation operators $a_k^\dagger$ and a_k with canonical commutation relations $[a_k, a_k^\dagger] = 1$.

The Hilbert space $\mathcal{H}_{\xi_k}$ of each mode is generated from a vacuum state $|0_k\rangle$ (defined by $a_k|0_k\rangle = 0$) by the creation operators. Explicitly, for the bosonic field,[4]

$$\mathcal{H}_{\xi_k} = \text{span}\left(\{|n_k\rangle,\, n_k \in \mathbb{N}\}\right) \tag{3.4}$$

where $|n_k\rangle \propto (a_k^\dagger)^n|0_k\rangle$. This basis obeys $N_k|n_k\rangle = n_k|n_k\rangle$ for the number operator $N_k = a_k^\dagger a_k$.

Denote by $\mathcal{H}_\xi(\Sigma)$ the total Hilbert space of the modes ξ on Σ, defined as the tensor product over modes

$$\mathcal{H}_\xi(\Sigma) = \otimes_k\, \mathcal{H}_{\xi_k}. \tag{3.5}$$

A basis for this space can be written $|n_{k_1} n_{k_2} \ldots\rangle$ (if the modes have a discrete index),

[3]By "a complete set of orthonormal positive frequency modes on Σ" we mean: a set ξ_k of complex-valued solutions to the classical field equation such that $\varphi = \sum_k \left(c_k\, \xi_k + d_k\, \xi_k^*\right)$ is a classical solution matching arbitrary complex Cauchy data on Σ, where c_k and d_k are complex coefficients, and such that $(\xi_{k'}, \xi_k) = \delta_{k'k}$ and $(\xi_{k'}, \xi_k^*) = 0$ in the inner product induced by the equations of motion (*i.e.* the Klein-Gordon norm). The inner product is linear in the first argument and obeys $(\varphi_1, \varphi_2) = (\varphi_2, \varphi_1)^* = -(\varphi_2^*, \varphi_1^*)$. One way to find a suitable set of modes is to require $\omega > 0$ relative to some timelike Killing vector field, if one exists. More broadly these conditions have little to do with frequency, but rather relate the classical symplectic to the quantum structure. See [18, 35, 81].

[4]For a fermionic field one uses canonical anticommutation relations, resulting in $\mathcal{H}_{\xi_k} = \text{span}\left(\{|0_k\rangle, |1_k\rangle\}\right)$, a two-level system at each mode (in contrast to the bosonic case of a harmonic oscillator at each mode).

which can also be translated to an equivalent Fock state notation. In the product space, the canonical commutation laws extend to $[a^\dagger_{k'}, a^\dagger_k] = [a_{k'}, a_k] = 0$ and $[a_{k'}, a^\dagger_k] = \delta_{k'k}$. The quantum operator ϕ at each point then acts on this Hilbert space as

$$\phi = \sum_k \left(a_k\, \xi_k + a^\dagger_k\, \xi^*_k\right), \tag{3.6}$$

defining the quantum theory. Bogoliubov transformations derive from requiring (3.6) be equal in two sets of modes. The orthonormal positive frequency condition ensures commutators are preserved in the transformation. The above statements translate to the case of a continuous index by standard methods [35].

Consider now a partial Cauchy surface $\Sigma_{AB} = \Sigma_A \cup \Sigma_B$ that is the union of two disjoint subsurfaces. Choose a set of modes $\xi_{AB} = \xi_A \oplus \xi_B$ (here $\oplus$ is merely a suggestive notation for the union of two sets of modes) where ξ_A is a set of modes on Σ_{AB} with Cauchy data equal to zero everywhere on Σ_B (and likewise for ξ_B). Given such a set of modes, it follows from (3.5) immediately that

$$\mathcal{H}_{\xi_A \oplus \xi_B}(\Sigma_{AB}) = \mathcal{H}_{\xi_A} \otimes \mathcal{H}_{\xi_B}. \tag{3.7}$$

But as ξ_A alone forms a complete set of modes on Σ_A, there is a natural identification of $\mathcal{H}_{\xi_A}$ with $\mathcal{H}_{\xi_A}(\Sigma_A)$, and likewise for B. Thus we can write, in the sense of (3.1–3.2), that

$$\mathcal{H}(\Sigma_{AB}) = \mathcal{H}(\Sigma_A) \otimes \mathcal{H}(\Sigma_B). \tag{3.8}$$

So even in the mode construction, Hilbert space may be built up as the tensor product of local subsystems.[5]

3.3 (Semi-)Classical framework

Ideally one would study the information problem in a classical spacetime background that is an exact solution ($G_{\mu\nu} = 8\pi\langle T_{\mu\nu}\rangle_{\rm ren}$) of semiclassical gravity with some quantum matter fields.[6] But due to the difficulty of incorporating the Hawking radiation backreaction, such a solution is not available.

Nonetheless, one can obtain approximations to such a solution using facts known from partial semiclassical calculations. For concreteness we continue to work with the massless scalar field (3.3), although the exact fields considered should not be essential to the picture.

We therefore define a spacetime $\mathcal{M}$ (described below), which is one such approximation, to serve as a classical background for quantum fields in an approximately semiclassical context.

While the global causal structure of $\mathcal{M}$ is the same as of Fig. 3.1, the benefit of using an explicit model is that one may make definite statements about internal

[5] One complete set of orthonormal positive-frequency modes on Σ is given by a set $h_{x'}(x) = f_{x'}(x) + ig_{x'}(x)$, labelled by $x' \in \Sigma$, where $f_{x'}$ and $g_{x'}$ are classical solutions with δ-function initial data at x' in the field value and time-derivative respectively. (These are propagators of the homogeneous field equation, related to Wightman functions [35].) Then for $x \in \Sigma$, in terms of these modes, $\phi(x) = a_x^\dagger + a_x$. These modes give meaning to the expression $\mathcal{H}(\Sigma) = \otimes_{x\in\Sigma}\mathcal{H}_x$, a fully local decomposition of the Hilbert space. One can decompose $\mathcal{H}(\Sigma_A \cup \Sigma_B) = \mathcal{H}(\Sigma_A) \otimes \mathcal{H}(\Sigma_B)$ in the same way—this is the construction usually implicitly or explicitly used in calculations of local von Neumann entropy.

[6] $\langle T_{\mu\nu}\rangle_{\rm ren}$ is a renormalized expectation value $\langle\psi|T_{\mu\nu}|\psi\rangle$ of the stress tensor for the matter fields in whatever quantum state $|\psi\rangle$ the fields are in. $G_{\mu\nu}$ is the usual classical Einstein tensor.

structure—in particular clarifying the status of the apparent and event horizons, the energy flux due to Hawking radiation, and the Schwarzschild mass at each spacetime point, within the model. These details allow one to construct a physically meaningful foliation in which to discuss the evaporation process, and provide additional intuition about how quantum calculations may be interpreted within the classical background. Equally importantly, the use of a concrete model precludes one from introducing potentially biased or self-contradictory assumptions about a background spacetime. So while $\mathcal{M}$ is by no means assumed to exactly represent the spacetime structure of an evaporating black hole, it provides an explicit representation that is likely more useful than the vague model used implicitly in figures like Fig. 3.1.

3.3.1 The spacetime $\mathcal{M}$

To avoid a full technical treatment, we formally define $\mathcal{M}$ as follows: let $\mathcal{M}$ be the spacetime defined by Sec. VI of [241] but with $l = 0$ (Schwarzschild interior). Presently we will give a more useful description.

The structure of $\mathcal{M}$ is depicted in Fig. 3.2. Locally the metric has the Schwarzschild form[7]

$$ds^2 = -\left(1 - \tfrac{2m(u,v)}{r(u,v)}\right) du\, dv + r(u,v)^2\, d\Omega^2 \tag{3.9}$$

with a Schwarzschild mass $m(u, v)$ varying as a function of some null coordinates. The

[7]The most conceptually simple representation of the metric is the local form (3.9), but there is no global coordinate system with this metric. For this reason we cannot simply write down $m(u, v)$ in a closed form. One can, however, parameterize future and past null infinity by continuous parameters that are locally u, v. The full metric is discussed in [241].

mass is a piecewise constant function forming an arbitrarily good stepwise approximation to some continuous dynamics. This leads to a shell (δ-function) approximation to a smooth $G_{\mu\nu}$.

The mass function $m(u, v)$ is then chosen as follows (but see the caveat in Footnote 7):

- Formation occurs by collapse of a sequence of spherical shells, approximating a continuous accretion dynamics $m_\infty(v)$ as viewed from past null infinity. The total mass is $m_\infty(v \to \infty) = M$.

- Shells of outgoing radiation are emitted from (a Planck length outside of)[8] the apparent horizon, approximating a continuous evaporation dynamics $m_\infty(u)$ as measured by an observer receiving the radiation at future null infinity. Corresponding shells of ingoing negative mass radiation fall in from (a Planck length outside of) the apparent horizon and are absorbed by the singularity. This model roughly approximates the DFU (Davies, Fulling, and Unruh [74]) stress tensor for black hole evaporation.

- The Schwarzschild mass changes across shells as dictated by standard junction conditions and the DTR (Dray–'t Hooft–Redmount [25, 86, 233]) relation.

This is in essence a discretized version of the model studied first by Hiscock [139].

Note two subtle points about this spacetime. First, it is the apparent horizon,

[8]Self-consistency of the classical model does not allow emission to originate either inside of or further away from the apparent horizon at $r = 2m$, see [241]. For this reason radiation must be emitted from near the apparent, and not the event, horizon.

and not the event horizon, which lies at $r = 2m$. The apparent horizon is spacelike during accretion and timelike during evaporation. Second, shells emitted from the horizon arise from an approximation to the DFU [74] stress tensor. They are not chosen to directly model Hawking pairs. In particular, the Hawking modes behind the event horizon propagate parallel to it (as illustrated later), while the negative energy flux modelled by shells is directed transversely into the horizons.

3.3.2 Globally hyperbolic subdomains

$\mathcal{M}$ is not globally hyperbolic.[9] As depicted in Fig. 3.3, early and late spatial slices have unequal domains of dependence.

An initial state describing collapsing matter on an early slice like Σ_- can be propagated throughout the domain of dependence $D(\Sigma_-)$. Since this region contains the entire process of black hole formation and evaporation (up to the final moments), it is sufficient to focus on this region for much of the discussion of information loss. In particular the evaporation time and Page time unitarity questions depend only on this region.

3.3.3 Foliation Σ_u of $D(\Sigma_-)$

Consider the domain of dependence $D(\Sigma_-)$ in Fig. 3.3. This region is globally hyperbolic, and therefore can be foliated by a family of surfaces Σ_u (each a Cauchy surface for $D(\Sigma_-)$) as depicted in Fig. 3.4. This region contains the entire process of

[9] See [241] for discussion of why no spacetime with the general structure of Fig. 3.1 is globally hyperbolic.

formation and evaporation, including all the Hawking radiation.

A surface $\mathcal{S}_{\text{ext}}$ (the "exterior surface of the collapsing matter/black hole") separates $\mathcal{M}$ into "in" and "out" regions. This surface is defined to coincide with the outermost accreting shell until it intersects the apparent horizon, after which it coincides with the outer part of the apparent horizon. Each

$$\Sigma_u = \Sigma_u^{\text{in}} \cup \Sigma_u^{\text{out}} \tag{3.10}$$

decomposes into "in" and "out" surfaces accordingly.

Each Σ_u is labelled by the time u at future null infinity when it intersects $\mathcal{S}_{\text{ext}}$. (One extrapolates the intersection to infinity along radial null curves.) By convention let $u = 0$ denote the time when the outermost shell crosses the apparent horizon. The end of evaporation occurs some finite time U later. Thus $u \in (-\infty, U)$ foliates the entire domain. Let Σ_U denote some Σ_u arbitrarily close to $u = U$.

3.3.4 Hilbert space, modes, and states

As in Sec. 3.2, Hilbert spaces are defined as Fock spaces of classical modes. As is standard (see *e.g.* [115, 131, 132]), we work in terms of modes describing classical wavepackets. Each set of modes ξ we define is implicitly taken to represent a set ξ_{ijlm} describing wavepackets centered at time t_i and frequency f_j with temporal width scale σ (times and frequencies being relative to a relevant coordinate system), and with angular harmonic component Y_{lm}. To obtain standard pair creation of Hawking modes requires

appropriately coordinating wavepacket spectra across sets of modes. This can be done for static black holes [131, 132] and we assume something analogous can be done here.

Several relevant sets of modes are depicted in Fig. 3.5.

The modes ξ^- are orthonormal positive frequency ingoing wavepackets with respect to asymptotically flat coordinates at past null infinity. These provide a complete set on all Σ_u and define $\mathcal{H}(\Sigma_u)$.

The relevant quantum state[10] on $\mathcal{H}(\Sigma_u)$ is usually taken to be an initial vacuum state $|0_-\rangle \equiv |0\rangle_{\xi^-}$. However we can just as well allow for the more general state (splitting ξ^- into sets of wavepackets before, during, and after the presence of collapsing shells)

$$|\psi\rangle \quad = \quad |0\rangle_{\xi^-_{\rm before}} \quad \otimes \quad |\psi\rangle_{\xi^-_{\rm collapse}} \quad \otimes \quad |0\rangle_{\xi^-_{\rm after}} \tag{3.11}$$

to include a description of the collapsing matter. Particle creation in excited states such as this is closely related to that in vacuum [52].

The modes ξ^+ and $\xi^{\rm EH}$ (Fig. 3.5) will also be relevant. ξ^+ are purely outgoing positive frequency wavepackets relative to asymptotically flat coordinates at future null infinity, with zero Cauchy data at the event horizon. $\xi^{\rm EH}$ have purely ingoing Cauchy data at the event horizon, with zero Cauchy data at future null infinity. $\xi^{\rm EH}$ modes can be formed into "wavepackets" with a particular correspondence to those in ξ^+ (at least in the quasistatic approximation [132]).

To analyze particle creation by the metric, one performs a Bogoliubov trans-

[10] We are in the Heisenberg picture where the state $|\psi\rangle$ is fixed. Time dependence arises both in operators, and when the state is described in terms of a time-dependent mode decomposition.

formation from the modes ξ^- defining $|\psi\rangle$ to some other complete set of orthonormal positive-frequency modes. Technically $EH \cup \mathcal{J}^+$ is not a Cauchy surface for $D(\Sigma_u)$ due to causal curves propagating from Σ_u to the singular point at the endpoint of evaporation. But (as discussed in Sec. 3.3.7), as is commonly done, let us ignore this technicality and assert that $\xi^{\rm EH} \oplus \xi^+$ forms a complete set of modes on Σ_u that can be used for this purpose.

In analogy with the standard Hawking calculation [131, 132], one expects that in terms of $\xi^{\rm EH} \oplus \xi^+$, the state $|\psi\rangle$ contains entangled pairs of ingoing (in $\xi^{\rm EH}$) and outgoing (in ξ^+) Hawking modes.

3.3.5 "In" and "Out" Hilbert spaces

To define a decomposition

$$\mathcal{H}(\Sigma_u) = \mathcal{H}(\Sigma_u^{\rm in}) \otimes \mathcal{H}(\Sigma_u^{\rm out}) \tag{3.12}$$

into time-dependent *in* and *out* Hilbert spaces requires a set of modes $\eta_u = \eta_u^{\rm in} \oplus \eta_u^{\rm out}$, where each mode only has support in the relevant subregion (see Sec. 3.2).

The usual way to construct this set is from modes with Cauchy data localized at each point (see Footnote 5). However the same can be achieved using wavepackets from infinity, cut off to have support only in the relevant region. This method makes the local and global Hilbert space constructions more similar.

Thus define modes η_u as follows (see Fig. 3.6). From complete sets of oscil-

lating modes with limited support (the support is a function of u as illustrated in the figure) at past and future null infinity, construct sets of orthonormal positive frequency wavepackets $\eta^-_{\rm in}(u)$, $\eta^-_{\rm out}(u)$, and $\eta^+_{\rm out}(u)$. Then

$$\begin{aligned} \eta^{\rm in}_u &\equiv \eta^-_{\rm in}(u), \\ \eta^{\rm out}_u &\equiv \eta^-_{\rm out}(u) \oplus \eta^+_{\rm out}(u), \end{aligned} \tag{3.13}$$

are complete on $\Sigma^{\rm in}_u$, $\Sigma^{\rm out}_u$ respectively (*cf.* Fig. 3.6 and Eq. (3.8)). This suffices to define (3.12).

The η modes can be taken to be similar to the ξ modes except near the boundaries where support is cut off, where η modes are non-analytic.

3.3.6 Apparent vs. event horizon

One may be tempted to use the event horizon, rather than the apparent horizon, to define the horizon area and *in* and *out* regions. In addition to the fact that the apparent horizon (at $r = 2m$) has local properties while the event horizon is global, there are a few reasons not to do so.

First, as the event horizon lies entirely at $u = U$, there is no meaningful way to relate times at future infinity (*i.e.* for an observer receiving Hawking radiation) to areas on the event horizon. And second, if $\Sigma^{\rm out}_u$ were defined by the event horizon, the "out" region would contain all the Hawking radiation at all times. We will not consider this possibility further.

3.3.7 Pathology at future null infinity

We have taken the Hawking modes to be a subset of the complete set $\xi^{\rm EH} \oplus \xi^+$ (Fig. 3.5), implicitly assuming that $EH \cup \mathcal{J}^+$ is a Cauchy surface for $D(\Sigma_u)$ in $\mathcal{M}$. This choice of modes is motivated by the requirement that late time modes be regular for observers at $\mathcal{J}^+$ (future null infinity). Its validity is usually justified by analogy with the standard Hawking calculation (for a static black hole formed by collapse) where $EH \cup \mathcal{J}^+$ is a global Cauchy surface.

We must emphasize, however, that $EH \cup \mathcal{J}^+$ is *not* a Cauchy surface for $D(\Sigma_u)$ in $\mathcal{M}$ (nor for $\mathcal{M}$ globally), due to curves terminating at the open singular point at the end of evaporation. Therefore $\xi^{\rm EH} \oplus \xi^+$ is technically not a valid complete set of modes on $D(\Sigma_u)$. Despite this pathology, we proceed as if it were valid, in order to connect to existing parts of the literature. Modified versions of the arguments below can be made to apply to a more correct mode decomposition, but we will not do so here.[11]

Not only is $EH \cup \mathcal{J}^+$ not technically a Cauchy surface, it fails badly at being one. If one tries to "fill in" the open singular point at the endpoint of evaporation (*e.g.* by regularizing the singularity), the surface fails to remain achronal. If one tries to deform it to avoid the singular point, the same occurs. And it is not the limit of any set of rigorous Cauchy surfaces. This pathology may be more than a benign technicality; for instance it shows that $\mathcal{M}$ (and likely all its close relatives) is a counterexample to the "PS Assumption" of [189].

[11] It would be more correct to regard Hawking modes in $\mathcal{M}$ as part of a complete set defined on Σ' in Fig. 3.5. Technically Σ' is also not a Cauchy surface for $D(\Sigma_u)$, but as the limit of a set of Cauchy surfaces it is admissible. Modes on Σ' are genuinely different from $\xi^{\rm EH} \oplus \xi^+$, since each mode will have support in only a limited subset of $\mathcal{J}^+$, and thus be nonanalytic on $\mathcal{J}^+$ as a whole.

In Sec. 3.4 we will discuss how "long term unitarity" violation is inherent to the spacetime structure of $\mathcal{M}$. The pathology at future null infinity discussed above is another, more subtle, manifestation of the same effect. In order to obtain a non-pathological $\mathcal{J}^+$, one can regularize the singularity as in Fig. 3.7. Then ξ^+ alone are a complete set of modes. In that case $\xi^{\rm EH} \oplus \xi^+$ double-counts event horizon modes, as $EH \cup \mathcal{J}^+$ is not achronal.

3.3.8 Unitarity questions

The principle of unitarity in a semiclassical context implies unitary evolution between the state of quantum fields on set Σ_u of Cauchy surfaces.[12] This principle holds absolutely within the present semiclassical framework.

However, several different forms of "unitarity," arising on different time scales, are often considered relevant to discussions of black hole information loss. Assuming an initial pure state $|\psi\rangle$ on Σ_- (Fig. 3.3), we say that evaporation is

- Long term unitary if there is a pure state on surfaces like Σ_+ (Fig. 3.3).
- Evaporation time unitary if Hawking radiation is in a pure state at the end of evaporation.
- Page time unitary if the entropy of Hawking radiation is decreasing with $S \leq A/4$

[12] Given the Hilbert space construction above, this notion is almost trivial: the (Heisenberg) state $|\psi\rangle$ is fixed, while a choice of modes ξ complete on Σ_u, used to define the Hilbert space basis, may vary with time. Unitarity then merely states that a unitary transformation relates valid complete bases. If one transforms to a Schrodinger wavefunctional picture (say through the local modes of Footnote 5), this reduces to a standard statement of unitary evolution of states. This also ensures Heisenberg operators like (3.6) evolve unitarily in a time dependent mode basis.

at late times.

In the following two sections we make these ideas mathematically precise, considering each in turn, and argue that none of them is expected to hold in $\mathcal{M}$ at the semiclassical level. Moreover, regularizing the singularity in $\mathcal{M}$ can restore the possiblility of long term unitarity, but not evaporation time or Page time unitarity.

One can frame these statements in terms of either the Hilbert space of Hawking modes, or in terms the Hilbert space of the *out* region. We first consider the former, then return to the latter in Sec. 3.6.

3.4 Long term unitarity

The "long term" unitarity question is the following: Is there necessarily a unitary evolution from quantum states on Σ_- to quantum states on Σ_+ in Fig. 3.3?[13]

3.4.1 In $\mathcal{M}$

If physics is accurately described by semiclassical gravity on a background spacetime like $\mathcal{M}$, the answer is clear: there is no reason to expect long term unitarity. The domains of dependence $D(\Sigma_-) \neq D(\Sigma_+)$ are unequal, and therefore, as discussed in Sec. 3.2, the Hilbert spaces

$$\mathcal{H}(\Sigma_-) \neq \mathcal{H}(\Sigma_+) \tag{3.14}$$

[13]This deals with the state of semiclassical matter fields. A separate question is whether evaporation can be described by a unitary S matrix in quantum gravity, *e.g.* in a path integral approach. These are not equivalent, in part because correlations may arise between the matter and geometry, but also because one might sum over geometries where the initial and final surfaces have different domains of dependence.

are physically inequivalent. Unitary evolution is not expected between physically inequivalent Hilbert spaces. Likewise, one does not expect invertible evolution of classical fields between surfaces with unequal domains of dependence.

It must be emphasized that there is no guarantee that black hole evaporation is accurately described by semiclassical gravity on a background spacetime like $\mathcal{M}$. However, if one gives up the assumption that something like $\mathcal{M}$ is correct—for example by demanding Σ_- and Σ_+ have a unitary relation—one must also give up on using the spacetime diagram for $\mathcal{M}$ to analyze the problem. (Or at least, provide some other justification for using such a diagram.) On occasion in the literature, studies will implicitly argue that the semiclassical description is incomplete or incorrect, yet at the same time continue making essential use of diagrams based on semiclassical spacetimes like $\mathcal{M}$ or Fig. 3.1. The self-consistency of such arguments must be called into question.

3.4.2 With a regularized singularity

Models like $\mathcal{M}$ have long term unitarity violation "baked into" their structure. One way to circumvent this issue is to replace $\mathcal{M}$ with a globally hyperbolic spacetime obtained by regularizing the $r = 0$ singularity.

One example of a regularized nonsingular background (based on a Hayward model [136, 241]) is depicted in Fig. 3.7. Models of this type are useful in that they include—rather than relegating to a singularity—a region of extreme density/curvature where quantum gravitational effects are important and known physics may fail.[14] For

[14]Regular models also introduce other issues associated with the inner horizon and exposed core [241]. Note however that the future surface of the dense region, which appears large due to conformal trans-

the same reason, semiclassical statements about such models must be taken with a grain of salt. The quantum gravity region may be thought of as a core that sources the gravitational field after collapse has completed.

The regularized model Fig. 3.7 does predict, at the semiclassical level, that long term unitary holds. The mechanism is uncertain, however, as semiclassical initial data would propagate through the quantum gravity region.

Unlike the long term issue, the evaporation time and Page time unitarity questions are framed entirely within the foliation Σ_u of the early region (blue outline) in Fig. 3.7. In this region the geometry is effectively identical to the singular case [241]. The discussion of evaporation time and Page time issues is therefore unaffected by regularizing the singularity. However entropy at infinity may then be purified after evaporation ends in such models.

3.5 Evaporation time and Page time unitarity

This section discusses the "evaporation time" unitarity issue, which relates to the von Neumann entropy of Hawking modes at the end of evaporation, and the "Page time" information issue, which tracks the time dependence of this entropy throughout the evaporation process.

Arguments for a firewall usually assume that unitarity implies the von Neumann entropy of Hawking modes must follow a Page curve. We will argue that this is

formations in the diagram, is actually Planckian in size—not so different from the naked singularity in $\mathcal{M}$—and that the inner horizon is hidden within the dense quantum gravity region.

not the case: in the manifestly unitary semiclassical theory of fields on $\mathcal{M}$, one should *not* expect a Page curve for the entropy of Hawking modes.

There is an important distinction here: a Page curve *should* be expected to arise in quantum gravitational descriptions—in particular, we do not disagree with recent holographic derivations [13, 14, 224] of the Page curve. But a Page curve in the underlying quantum gravity theory does not imply a Page curve for semiclassical Hawking modes—and it is the entropy of semiclassical modes whose Page curve implies a firewall. The connection to quantum gravity is explored further in Sec. 3.7.

3.5.1 Entropy of Hawking modes

Of interest here is the von Neumann entropy of Hawking modes as a function of time. We denote this entropy $S_{\rm rad}(u)$, a function of time u at future null infinity, and define it as follows.

The modes labelled $\xi^{\rm rad}_u$ in Fig. 3.8 are the "Hawking modes up to time u." These are a subset of the wavepacket modes ξ^+ in Fig. 3.5, specifically, the subset with wavepackets centered before time u. The "Hilbert space of Hawking radiation at time u" is the Hilbert space of these modes,

$$\mathcal{H}^{\rm rad}_u \equiv \mathcal{H}_{\xi^{\rm rad}_u}. \tag{3.15}$$

This Hilbert space can be written as the tensor product of Hilbert spaces describing wavepacket modes, defined at each time u', over times $u' < u$. Note that $\mathcal{H}^{\rm rad}_u$ is

distinct from the Hilbert space of the *out* region $\mathcal{H}(\Sigma_u^{\rm out})$, which will be discussed in Sec. 3.6.

The modes $\xi_u^{\rm rad}$ are a subset of ξ^+ and therefore of the full set $\xi^{\rm EH} \oplus \xi^+$ (*cf.* Sec. 3.3.4). In this way the Hawking radiation Hilbert space $\mathcal{H}_u^{\rm rad}$ is a subspace of the full semiclassical Hilbert space $\mathcal{H}(\Sigma_u)$. Since the global state $|\psi\rangle$ in $\mathcal{H}(\Sigma_u)$ is pure, the reduced state in $\mathcal{H}_u^{\rm rad}$ will generically be mixed, with density matrix $\rho_u^{\rm rad}$.

The entropy of Hawking modes at time u is then

$$S_{\rm rad}(u) \equiv S(\rho_u^{\rm rad}), \tag{3.16}$$

the von Neumann entropy in the Hawking radiation subspace of the semiclassical Hilbert space of fields.

3.5.2 Evaporation time unitarity

"Evaporation time unitary" holds if

$$S_{\rm rad}(U) = 0, \tag{3.17}$$

in other words, if the Hawking modes are in a pure state at the time U when evaporation completes. This form of unitarity is assumed in, *e.g.*, the well known "AMPS" firewall paper [15].

Taken as an assumption in its own right, this would simply not be a correct application of the general principle of unitarity to semiclassical fields in the spacetime $\mathcal{M}$.

One expects unitary evolution between the total Hilbert spaces $\mathcal{H}(\Sigma_u)$. It is clear that

$$\mathcal{H}(\Sigma_u) \neq \mathcal{H}_U^{\rm rad}, \tag{3.18}$$

because the outgoing Hawking modes do not form a complete set of modes on Σ_u, and $\mathcal{H}_U^{\rm rad}$ is only a subspace of $\mathcal{H}(\Sigma_u)$. That is, the full Hilbert space consists of more than just the outgoing Hawking modes, even at the end of evaporation. (As a subset of the complete set $\xi^{\rm EH} \oplus \xi^+$, the outgoing Hawking modes ($\xi_U^{\rm rad}$) are missing both the ingoing Hawking modes ($\xi^{\rm EH}$) and the postevaporation outgoing subset of ξ^+.) Therefore there is no a priori reason to think the Hawking radiation state $\rho_U^{\rm rad}$ should be pure.[15]

Nonetheless, it could still be reasonable to justify the evaporation time unitarity condition based on the time evolution of $S_{\rm rad}(u)$. If Page time unitarity were to hold, then so would evaporation time unitarity. Whether this holds is discussed next.

3.5.3 Page time unitarity

The "Page time" unitarity issue involves the time-dependence of $S_{\rm rad}(u)$ in relation to the semiclassical horizon area in the foliation Σ_u (Fig. 3.4).

In this foliation $A(u)$, defined as the area of the (outer) apparent horizon on Σ_u, starts at $A(0) \propto M^2$ and decreases to $A(U) = 0$ when evaporation completes.

[15] Given this failure one might suggest an alternate condition $S_{\rm rad}(\infty) = 0$ would hold. But this reduces to the question of long term unitarity discussed earlier, as ξ^+ are a complete set of modes on Σ_+.

Page time unitarity will be said to hold if

$$S_{\text{rad}}(u) \leq A(u)/4 \tag{3.19}$$

at all times.

When Page time unitarity holds, it is usually argued that $S_{\text{rad}}(u)$ first increases according to Hawking's prediction of thermal emission, until a time (the "Page time") when it would surpass $A(u)/4$, after which it decreases according to $S_{\text{rad}}(u) = A(u)/4$. Then $S_{\text{rad}}(u)$ is said to follow the "Page curve" [223].

3.5.3.1 Argument in favor

The total Hilbert space $\mathcal{H}$ consists of "the black hole plus the Hawking radiation," so decomposes as

$$\mathcal{H} = \mathcal{H}_u^{\text{bh}} \otimes \mathcal{H}_u^{\text{rad}}, \tag{3.20}$$

with reduced densities ρ_u^{bh} and ρ_u^{rad} in the subsystems. The total system is in a pure state, so

$$S(\rho_u^{\text{bh}}) = S(\rho_u^{\text{rad}}). \tag{3.21}$$

But the thermodynamic (Bekenstein-Hawking) entropy of the black hole is $S_{\text{th}}(u) = A(u)/4$. Since thermodynamic entropy is a coarse-grained entropy of the black hole (see

e.g. [13, 125, 223, 228, 240, 265, 266]), it follows that[16]

$$S(\rho_u^{\rm bh}) \leq A(u)/4. \tag{3.22}$$

Thus $S_{\rm rad}(u) \leq A(u)/4$.

3.5.3.2 The problematic assumption

The problematic assumption in the preceding argument is the decomposition

$$\mathcal{H} = \mathcal{H}_u^{\rm bh} \otimes \mathcal{H}_u^{\rm rad}, \tag{3.23}$$

where neither $\mathcal{H}_u^{\rm bh}$ nor $\rho_u^{\rm bh}$ were given a concrete definition. There are various ways to interpret this statement, depending whether one treats it as a semiclassical or quantum gravitational equation. Each gives a different meaning to "the entropy of the black hole." But none provides a strong justification for

$$S_{\rm rad}(u) \leq A(u)/4, \tag{3.24}$$

if $S_{\rm rad}(u)$ is the von Neumann entropy of semiclassical Hawking modes.

One key point is that the bound $S(\rho_u^{\rm bh}) \leq A(u)/4$ derived from coarse-graining is likely to be valid only if $\rho_u^{\rm bh}$ represents a full quantum gravitational state—applying this bound in the semiclassical theory requires justifying an identification between "the

[16] An alternate justification, that $\log \dim \mathcal{H}_u^{\rm bh} = A(u)/4$, is sometimes assumed to the same effect.

Hilbert space of the black hole" and some space of semiclassical modes.

We analyze the possible interpretations, and their implications, in the following subsections 3.5.3.3–3.5.3.5.

3.5.3.3 Purely semiclassical interpretation

If one works purely within the semiclassical framework, then (3.23) reads

$$\mathcal{H}(\Sigma_u) = \mathcal{H}_{\chi_u} \otimes \mathcal{H}_u^{\rm rad}, \tag{3.25}$$

where $\mathcal{H}_u^{\rm bh} = \mathcal{H}_{\chi_u}$ is the Hilbert space of "all the modes except the Hawking modes" (that is, of χ_u where $\chi_u \oplus \xi_u^{\rm rad}$ is some complete set of modes on Σ_u).

In this case $\mathcal{H}_u^{\rm bh}$ is the Hilbert space of modes $\xi^{\rm EH} \oplus \overline{\xi_u^{\rm rad}}$, where $\overline{\xi_u^{\rm rad}}$ is the complement in ξ^+ of $\xi_u^{\rm rad}$ (*cf.* Figs. 3.5, 3.8). This is not the Hilbert space of any relevant partial Cauchy surface, and in particular it is not $\mathcal{H}(\Sigma_u^{\rm in})$. Moreover, there is no clear relationship between the modes defining $\mathcal{H}_u^{\rm bh}$ and the horizon area $A(u)$. Indeed, there is no meaningful sense in which the so-called $\mathcal{H}_u^{\rm bh}$ is "the Hilbert space of the black hole." There is no justification for $S(\rho_{\chi_u}) \leq A(u)/4$, and no reason for Page time unitarity to hold.

Moreover, Bogoliubov transformations from the modes ξ^- to $\xi^{\rm EH} \oplus \xi^+$ in $\mathcal{M}$ could in principle be directly evaluated, giving a direct calculation of $S_{\rm rad}(u)$ under unitary semiclassical evolution. It is unlikely, both in analogy with the standard Hawking calculation, and due to the presence of ξ^- modes straddling the event horizon, that this

could lead to a pure state $S_{\rm rad}(U) = 0$ at the end of evaporation.

3.5.3.4 Partially semiclassical interpretation

Suppose one interprets $\mathcal{H}_u^{\rm rad}$ as the semiclassical Hilbert space of Hawking modes, but interprets $\mathcal{H}_u^{\rm bh}$ as some quantum gravitational "full description" of the black hole (let us denote quantum gravitational Hilbert spaces with a tilde, in this case $\mathcal{H}_u^{\rm bh} = \tilde{\mathcal{H}}_u^{\rm bh}$). Now there is a fair justification for $S(\tilde{\rho}_u^{\rm bh}) \leq A(u)/4$. But another part of the argument breaks down.

There are two cases, depending whether or not one claims that the quantum gravitational Hilbert space $\tilde{\mathcal{H}}_u^{\rm bh}$ is equivalent to a semiclassical Hilbert space of modes.

If one does not make such an identification, then there is no guarantee that the Hilbert spaces $\tilde{\mathcal{H}}_u^{\rm bh} \otimes \mathcal{H}_u^{\rm rad}$ and $\mathcal{H}(\Sigma_u)$ are equivalent. If one starts with a pure state $|\psi\rangle$ in $\mathcal{H}(\Sigma_u)$, as is typically done, there is no reason for a state in $\mathcal{H}$ to be pure—if such a state is even defined.

More reasonably, one may claim (perhaps through holography) that the quantum gravitational Hilbert space $\tilde{\mathcal{H}}_u^{\rm bh}$ is equivalent to the Hilbert space of some semiclassical modes $\chi_u^{\rm bh}$. These must be part of a complete set $\chi_u^{\rm bh} \oplus \chi_u^{\rm other} \oplus \xi_u^{\rm rad}$, so that

$$\mathcal{H}(\Sigma_u) = \tilde{\mathcal{H}}_u^{\rm bh} \otimes \mathcal{H}_{\chi_u^{\rm other}} \otimes \mathcal{H}_u^{\rm rad} \tag{3.26}$$

with $\tilde{\mathcal{H}}_u^{\rm bh} = \mathcal{H}_{\chi_u^{\rm bh}}$. We have allowed for the presence of some modes $\chi_u^{\rm other}$ that are part of neither the radiation nor the black hole (these could include, for example, outgoing

modes after evaporation ends, but we leave them unspecified as they depend on the choice of $\chi_u^{\rm bh}$).

If one assumes these $\chi_u^{\rm other}$ are totally uncorrelated from the rest of the system (schematically, that $|\psi\rangle = |\psi\rangle_{\rm bh,rad} \otimes |\psi\rangle_{\rm other}$) then, by adapting the earlier argument, there is a strong justification for $S_{\rm rad}(u) \leq A(u)/4$ and Page time unitarity holds.

If one wants to make this claim they should lay out clearly what the modes $\chi_u^{\rm bh}$ and $\chi_u^{\rm other}$ are, explain in precisely what sense $\tilde{\mathcal{H}}_u^{\rm bh} = \mathcal{H}_{\chi_u^{\rm bh}}$, and explain why $\chi_u^{\rm other}$ are uncorrelated from the rest of the system.

Lacking a clear and explicit case for this identification, applying the entropy bound $A(u)/4$ to a subset of the semiclassical modes is insufficiently justified.

Nonetheless, the idea that the quantum gravitational Hilbert space $\tilde{\mathcal{H}}_u^{\rm bh}$ can be identified with a space of semiclassical modes is not unreasonable. Later we will return to identifications of this type motivated by holography. In those cases, however, the conclusion $S_{\rm rad}(u) \leq A(u)/4$ still does not necessarily follow. This is because—in the language of this section—either there is no decomposition $\chi_u^{\rm bh} \oplus \chi_u^{\rm other} \oplus \xi_u^{\rm rad}$ (as would also be the case if one naively identified the quantum gravitational space with the semiclassical *in* region), or because $\chi_u^{\rm other}$ are not uncorrelated from the rest of the system.

3.5.3.5 Fully quantum gravitational interpretation

If one interprets both pieces of the decomposition as quantum gravitational Hilbert spaces then (3.23) reads

$$\tilde{\mathcal{H}} = \tilde{\mathcal{H}}_u^{\text{bh}} \otimes \tilde{\mathcal{H}}_u^{\text{rad}}. \tag{3.27}$$

This is the case when the black hole Hilbert space is described through AdS/CFT.

In this case there is justification for $S(\tilde{\rho}_u^{\text{rad}}) \leq A(u)/4$. However, now it is not clear that the quantum gravitational space $\tilde{\mathcal{H}}_u^{\text{rad}}$ relates to the space of semiclassical Hawking modes $\mathcal{H}_u^{\text{rad}}$. In other words, with this interpretation, $S(\tilde{\rho}_u^{\text{rad}}) \neq S_{\text{rad}}(u)$.

So while the Page curve likely arises in quantum gravity, that may not imply the same for the semiclassical modes. Understanding that correspondence requires further investigating the relationship of the semiclassical and quantum gravitational Hilbert spaces, which will be considered in Sec. 3.7.

3.5.3.6 Summary

Naively decomposing $\mathcal{H}(\Sigma_u) = \mathcal{H}_u^{\text{bh}} \otimes \mathcal{H}_u^{\text{rad}}$ leads to the conclusion $S_{\text{rad}}(u) \leq A(u)/4$, implying that $S_{\text{rad}}(u)$ follows a Page curve. But closer inspection reveals that if $S_{\text{rad}}(u)$ is meant to be the von Neumann entropy of semiclassical Hawking modes, then in any interpretation either the decomposition itself is invalid, or the conclusion does not follow from it. Thus the claim that $S_{\text{rad}}(u)$ follows a Page curve is weak, and other curves for the semiclassical $S_{\text{rad}}(u)$, including the traditional Hawking curve,

may be consistent with unitarity. On the other hand, entropies describing quantum gravitational degrees of freedom may still follow a Page curve, as discussed later.

3.6 Entropy of the "In/Out" regions

In the previous section, questions of unitarity were framed in terms of $S_{\rm rad}(u)$, the von Neumann entropy of Hawking modes at future infinity. That entropy is distinct from, though sometimes conflated with, the von Neumann entropy

$$S_{\rm out}(u) \equiv S(\rho_u^{\rm out}) \tag{3.28}$$

of fields in the *out* region. Here $\rho_u^{\rm out}$ is the reduced density matrix on $\Sigma_u^{\rm out}$ (Fig. 3.4). Each is defined in terms of a different mode decomposition: $S_{\rm rad}(u)$ in terms of $\xi^{\rm EH} \oplus \xi^+$ (Fig. 3.5), and $S_{\rm out}(u)$ in terms of $\eta_u^{\rm in} \oplus \eta_u^{\rm out}$ (Fig. 3.6).

These entropies, $S_{\rm rad}(u)$ and $S_{\rm out}(u)$, have vastly different character, as can be seen in the simple Minkowski space example of Fig. 3.9. In that example, $S_{\rm rad}(u)$ begins at zero, increases as entangled modes arrive at infinity, then is purified back to zero by the later radiation. Meanwhile, $S_{\rm out}(u)$ is infinite at all times, with a UV-divergent leading order ("vacuum") contribution proportional to the area of its boundary [50, 140, 250].

Despite this basic difference, these entropies may be related. There exist in

the literature a number of plausible arguments [13, 140, 223] (see also [60]) that

$$S_{\rm out}(u) \approx S_{\rm vac}(u) + S_{\rm rad}(u), \tag{3.29}$$

or equivalently, that $S^{\rm ren}_{\rm out}(u) \approx S_{\rm rad}(u)$ after renormalizing by subtracting out the vacuum term.[17]

Such arguments are generally based on the idea that, if one partner in a pair of Hawking modes has significant support only in the *out* region, that mode contributes its entropy to the *out* region. As $u \to U$ more outgoing Hawking partners emerge into the *out* region causing an evolution of $S_{\rm out}(u)$. This scenario is depicted in Fig. 3.10. One can make an analogous argument in the Minkowski space example of Fig. 3.9.[18]

Now we return to the question of Page/evaporation time unitarity, and its relation to the firewall problem, this time in the context of $S_{\rm out}(u)$.

3.6.1 Page time unitarity again

Suppose one identifies the quantum gravitational black hole Hilbert space with the semiclassical Hilbert space of modes behind the horizon, $\tilde{\mathcal{H}}^{\rm bh}_u = \mathcal{H}(\Sigma^{\rm in}_u)$. Then, since von Neumann entropy is not greater than thermodynamic (coarse-grained) entropy, one would expect $S(\rho^{\rm in}_u) \leq A(u)/4$. Since the total bipartite state is pure, this also implies $S_{\rm out}(u) \leq A(u)/4$, suggesting that $S_{\rm out}(u)$ would follow a Page curve. If this were true it

[17] If one displaces the *in/out* boundary surface outward to a line of constant radius outside the horizon, as done for instance in [13], this renormalization should amount to subtracting a divergent constant (proportional to the constant area of the boundary).

[18] In that example the argument would suggest that $S_{\rm out}(u) = S_{\rm vac}(u) + 1$ bits for $u_1 < u < u_2$, and $S_{\rm out}(u) = S_{\rm vac}(u)$ otherwise. Note that this cannot be exactly true as the entangled modes each have finite width.

would imply a product state $|\psi\rangle_{\text{in}} \otimes |\psi\rangle_{\text{out}}$ at the end of evaporation, and thus a firewall at the late time apparent horizon.

As with the discussions in Sec. 3.5, the identification $\tilde{\mathcal{H}}_u^{\text{bh}} = \mathcal{H}(\Sigma_u^{\text{in}})$ must be called into question, and requires a more concrete justification. Naively applying holographic principles may suggest this identification, but more detailed studies based on entanglement wedge reconstruction suggest a different one (see Sec. 3.7).

The bound $S(\rho_u^{\text{in}}) \leq A(u)/4$ also cannot be directly justified through a Bousso bound [41] (or Bekenstein bound [29]), since the only converging lightsheet from a point on the apparent horizon terminates at the spacelike singularity. This was pointed out earlier by Rovelli [234].

Moreover, $S(\rho_u^{\text{in}})$ is formally infinite, so the thermodynamic bound must be applied either after a UV cutoff, or after renormalizing by subtracting the vacuum term. In the first case the bound seems to be a statement mainly about the dominant vacuum term, and not about the entropy of Hawking radiation. Moreover, the fact that the Page curve begins at zero seems to preclude it from including the vacuum entropy. In the second case, it is not clear why the coarse-grained bound on von Neumann entropy should still be relevant after renormalization.

In this light, evaporation time and Page time unitarity can be expected for neither $S_{\text{out}}(u)$ nor $S_{\text{rad}}(u)$, barring some improved justification.

3.7 Connection to holographic quantum gravity

Throughout earlier sections, the question was raised of what correspondence exists between semiclassical Hilbert spaces and underlying quantum gravitational ones. Recent holographic studies [12–14, 224] (based on the AdS/CFT correspondence [186]) suggest a solution.

Given a quantum "boundary" theory on $\mathcal{H}^{\mathrm{QM}} = \mathcal{H}^{\mathrm{QM}}_{\mathrm{bh}} \otimes \mathcal{H}^{\mathrm{QM}}_{\mathrm{out}}$ whose semiclassical "bulk" dual is a forming and evaporating black hole, the boundary Hilbert spaces $\mathcal{H}^{\mathrm{QM}}_{\mathrm{bh}}$ and $\mathcal{H}^{\mathrm{QM}}_{\mathrm{out}}$ each determine an entanglement wedge in the bulk. These entanglement wedges are illustrated (based on the calculations of [13, 14]), during evaporation after the Page time, in Fig. 3.11.

In this context one may calculate boundary von Neumann entropies $S(\rho^{\mathrm{QM}}_{\mathrm{bh}})$ and $S(\rho^{\mathrm{QM}}_{\mathrm{out}})$, and show that they are equal and follow a Page curve [13, 14, 224]. These boundary entropies are related to bulk entropy in their entanglement wedge through a quantum extremal surface (quantum Ryu-Takayanagi) prescription [85, 87, 146, 237]. In particular,

$$S(\rho^{\mathrm{QM}}_{\mathrm{out}}) = S_{\mathrm{bulk}}(\Sigma^{\mathrm{QM}}_{\mathrm{out}}) + \tfrac{A_{\mathrm{QES}}}{4}, \tag{3.30}$$

where $S_{\mathrm{bulk}}(\Sigma^{\mathrm{QM}}_{\mathrm{out}})$ is the von Neumann entropy of bulk fields on any surface $\Sigma^{\mathrm{QM}}_{\mathrm{out}}$ that is a Cauchy surface for the entanglement wedge of $\mathcal{H}^{\mathrm{QM}}_{\mathrm{out}}$. (That is, on a Cauchy surface for just the blue region in Fig. 3.11, including both the exterior region and island. The intersection of the black line with both parts of the blue region is one such surface.) A_{QES} is the area (in Planck units) of the appropriate quantum extremal surface.

Thus the boundary entropies, which follow the Page curve, do dictate the semiclassical entropy in certain regions—but these regions are not the ones usually naively identified as *in* and *out*. That is, $S(\rho_{\rm out}^{\rm QM})$ does follow the Page curve, but the entropy $S_{\rm out}(u)$ in the bulk *out* region need not.[19]

In particular, these studies suggest that, after the Page time, the bulk fields in each entanglement wedge (Fig. 3.11) have negligible von Neumann entropy (after subtracting a vacuum term) to leading order. This is consistent with a semiclassical Hawking curve in the bulk *out* region, arising from entanglement between the *out* region and the island.

Moreover, as depicted in Fig. 18 of [13], after evaporation ends the entanglement wedge of $\mathcal{H}_{\rm out}^{\rm QM}$ contains the region behind the event horizon. Thus the semiclassical state on a late spatial slice like Σ_+ (Fig. 3.3) need not be pure, even though $\mathcal{H}_{\rm out}^{\rm QM}$ is in a pure state.

This suggests that semiclassical long term, evaporation time, and Page time unitarity may all fail, even when a Page curve arises in an underlying unitary theory of quantum gravity.[20,21]

Given these two levels of description, what will be measured by an observer at

[19] The *out* region in the holographic calculations is defined by a fixed radius surface outside all horizons, rather than by our $\mathcal{S}_{\rm ext}$, but the conclusion is the same.

[20] Some other studies (*e.g.* [9]) have suggested that the boundary Page curve and bulk Hawking curve are contradictory. This relies on identifying the bulk and boundary entropies in a way that does not follow from entanglement wedge reconstruction. This also assumes that a bulk Hawking curve in $\mathcal{M}$ fundamentally violates unitarity, which we have argued against.

[21] Recently it has also been argued [189], based on the path-integral quantum gravity of an ensemble of black holes, that a version of Page time unitarity arises effectively within superselection sectors of the theory. In that approach the notion of quantum gravitational unitarity for an individual black hole may differ somewhat from the above discussions.

infinity? This depends on precisely what is meant by "observer at infinity," in particular whether such an observer interacts locally with bulk or boundary operators. Clearly an observer with access to all boundary observables can deduce all information about the state.[22] However, if one conceives of an observer at infinity as one that observes itself outside a spatially distant gravitating object, it seems implicit that such an observer is interacting with bulk observables. In contrast, it is not clear in precisely what sense an observer in the boundary theory can be described as being outside a spatially distant gravitating object, given the nonlocal boundary encoding of interior and exterior bulk degrees of freedom (see *e.g.* [62]). Further clarifying what bulk or boundary observables might be realistically measured in experiments (*i.e.* which type of operators can "we" measure) is a useful topic of continued study.

3.8 Discussion

The correct statement of the principle of unitarity depends at what level a theory is described. In semiclassical gravity, it demands a unitary evolution between states in $\mathcal{H}(\Sigma_u)$, the Hilbert space of quantum fields on a series of Cauchy surfaces. In quantum gravity, it demands unitary evolution of states in $\mathcal{H}^{\text{QM}}$, an underlying quantum mechanical Hilbert space from which spacetime and gravity may emerge.

We have argued that even if unitarity holds in both senses described above, the more commonly invoked notions of long term, evaporation time, and Page time

[22] As with any quantum system, an observer with access to these observables would still need to reconstruct the state through tomography on an ensemble in order to gain full information about the state.

"unitarity" may all be violated. In other words, neither "information loss at infinity" nor a semiclassical "Hawking curve" necessarily signify unitarity violation.[23]

One key aspect of the argument was the distinction between semiclassical and quantum gravitational degrees of freedom—holographic calculations suggest that a Page curve is present at the quantum gravitational level, but not necessarily at the semiclassical level.

We see four ways to refute our conclusions about unitarity. One could claim that: (1) No semiclassical theory accurately describes black hole formation and evaporation; (2) There is a useful semiclassical theory but $\mathcal{M}$ is a poor approximation of it; (3) The semiclassical framework above contains faulty assumptions or unjustified steps; (4) Within the above framework, there is a stronger justification for long term, evaporation time, or Page time unitarity that was not considered. It would be useful to distinguish between these possibilities in claims that these forms of unitarity are restored.

On occasion other entropies are studied besides the ones considered here. In that context, one might introduce some entropy related to black hole evaporation, find that it deviates from a Page curve, and claim that this signifies an information problem. Then, one can introduce some other (perhaps very different) quantity, also called "entropy," which does follow a Page curve, thereby resolving the problem. Generalizing the present work, we suggest that an entropy deviating from a Page curve is not necessarily problematic, and any unitarity problem that arises should be made clear and explicit. Further, any entropies introduced in these analyses should be carefully related

[23] As these are the forms of "unitarity" usually assumed in the argument for firewalls, this implies there is no need for firewalls to form.

to a particular meaning of the black hole Hilbert space.

Here we studied the problem in a spacetime $\mathcal{M}$ with singularity. A number of other papers have argued for nonsingular models (like Fig. 3.7), where quantum effects regulate the singularity. The common objection to such models is the claim: *A unitarity problem arises at the Page time, when singular and nonsingular models are equivalent.* If that were true, regularized models would be irrelevant to the information problem.

Our conclusions amount to an argument against this objection, affirming the viability of regular models. Similar arguments were made recently by Ashtekar [19] using a regular model inspired by loop quantum gravity that coincides with $\mathcal{M}$ in the semiclassical region (our $D(\Sigma_-)$). In that paper another form of the Page time argument based on "energy budget per mode" was also refuted. In regular spacetimes one expects long term unitarity to be restored, while evaporation time and Page time unitarity remain violated.

Ultimately there is no guarantee that *any* semiclassical spacetime can fully represent the black hole evaporation process. Nonetheless, use of spacetimes like $\mathcal{M}$ is prevalent in the literature.

We emphasize that even if one does believe $\mathcal{M}$ is a useful evaporation model, black hole evaporation is not paradoxical. There is no fundamental contradiction between unitarity and relativity. A contradiction only arises if one considers limited forms of semiclassical unitarity that, on closer inspection, are poorly motivated.

On the other hand, the fact that long term unitarity is given up in $\mathcal{M}$ is a sign of its pathologies (lack of global hyperbolicity and the pathology of future null infinity).

It does seem reasonable to hope evaporation will be described by a semiclassical theory with a scattering matrix from past to future infinity (unless there arise significant correlations between matter and geometry, or matter and sub-Planckian degrees of freedom). But such a theory will not include something like $\mathcal{M}$ as a background.

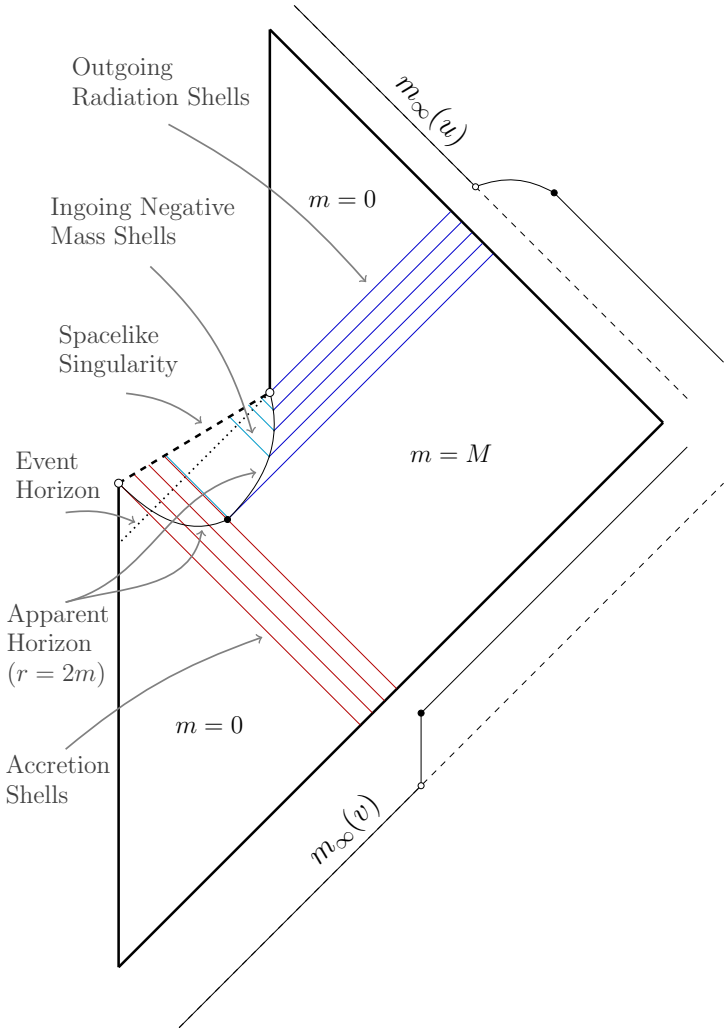

Figure 3.2: The spacetime $\mathcal{M}$ used as a background for quantum fields. This schematic causal diagram for $\mathcal{M}$ is known to be qualitatively correct based on Penrose diagrams that were computed numerically in previous work [239, 241].

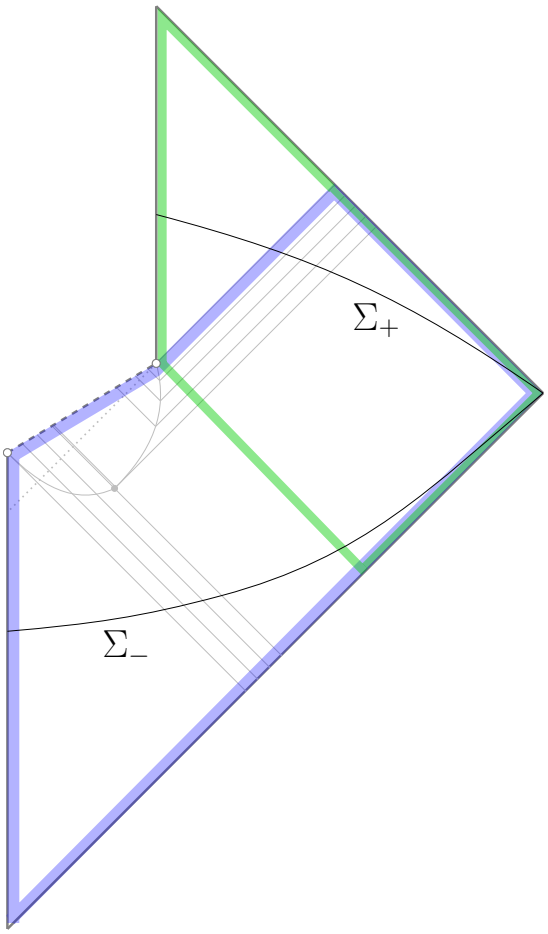

Figure 3.3: Early (Σ_-) and late (Σ_+) partial Cauchy surfaces in $\mathcal{M}$. The domains of dependence $D(\Sigma_-)$ (blue outline) and $D(\Sigma_+)$ (green outline) are not equal.

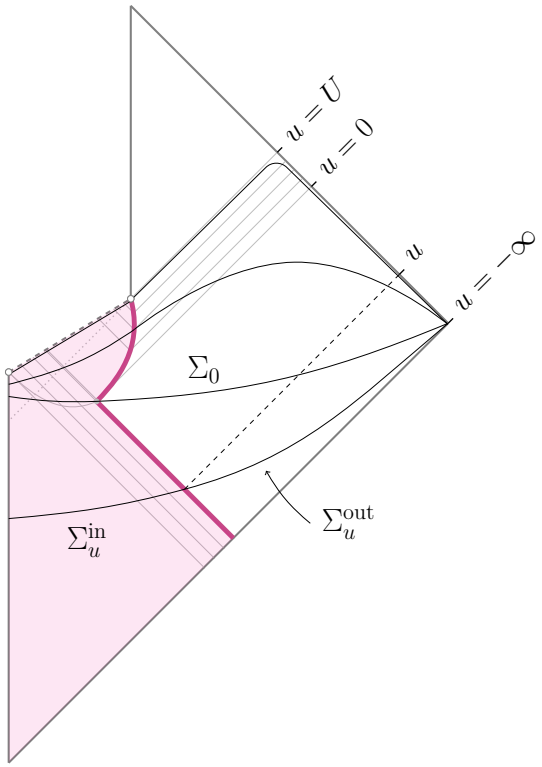

Figure 3.4: Foliation Σ_u of the region $D(\Sigma_-)$ in $\mathcal{M}$. The surface $\mathcal{S}_{\text{ext}}$ (magenta), which coincides with the outermost accreting shell for $u \leq 0$ and with the outermost apparent horizon for $u \geq 0$ (and with both at $u = 0$ where they meet), separates $D(\Sigma_-)$ into "in" (magenta fill) and "out" regions. Each $\Sigma_u = \Sigma_u^{\text{in}} \cup \Sigma_u^{\text{out}}$ decomposes accordingly. The label u is the time at future null infinity (extrapolated along radial null curves) when each Σ_u intersects $\mathcal{S}_{\text{ext}}$. Evaporation begins at $u = 0$ and ends at $u = U$.

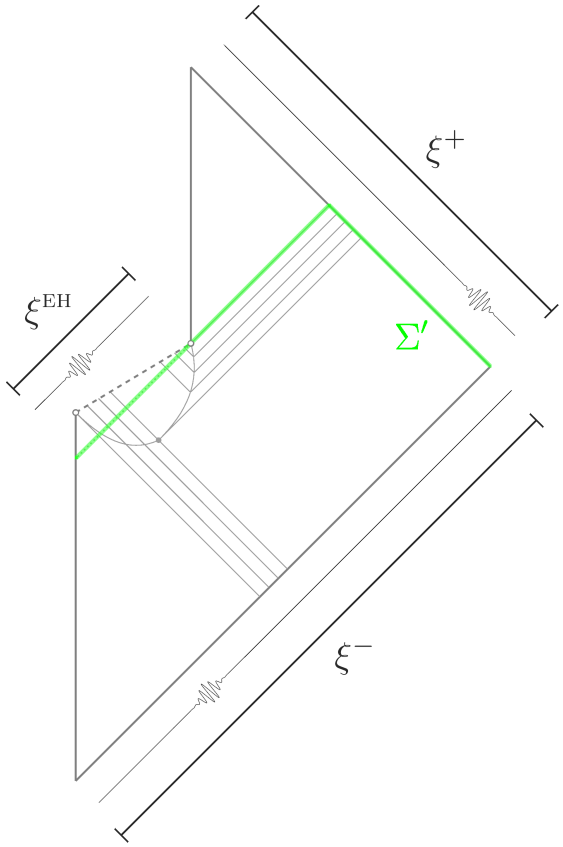

Figure 3.5: Sets of modes can be defined on various partial Cauchy surfaces in $\mathcal{M}$. Modes on each surface are taken to represent classical wavepackets, as can be achieved by appropriate transformations from oscillating modes. Modes ξ^- at past null infinity define the quantum state $|\psi\rangle$. Transforming to another set $\xi^{\mathrm{EH}} \oplus \xi^+$ dictates particle creation. Modes defined on Σ' (green) can help resolve a pathology of the modes $\xi^{\mathrm{EH}} \oplus \xi^+$, which are technically not a valid complete set in $\mathcal{M}$.

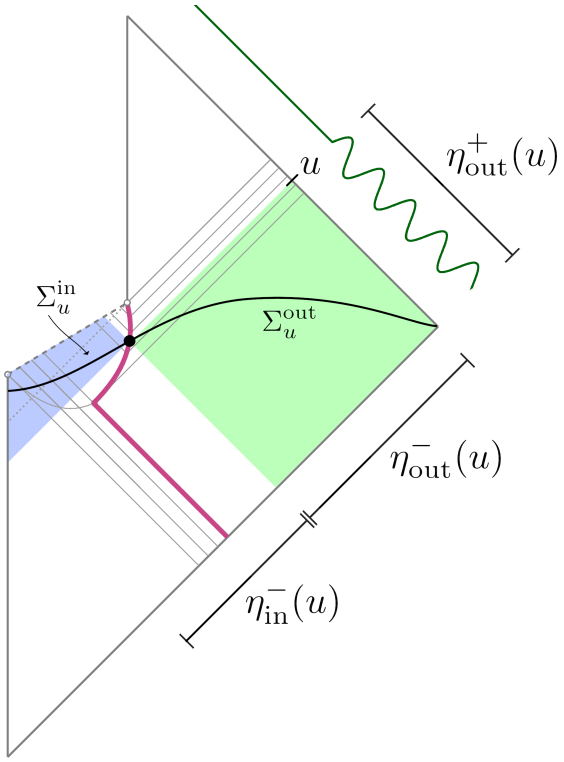

Figure 3.6: Splitting $\mathcal{H}(\Sigma_u)$ into time-dependent *in* and *out* subspaces. The η modes are wavepackets with limited support (support illustrated by green curve). Modes η_u^{in} and η_u^{out} (see (3.13)) are respectively complete on the *in* (blue fill) and *out* (green fill) domains of dependence. All these spaces are time-dependent, with the boundaries and mode support regions sliding around as functions of u. As $u \to U$ the *in* domain becomes the region behind the event horizon.

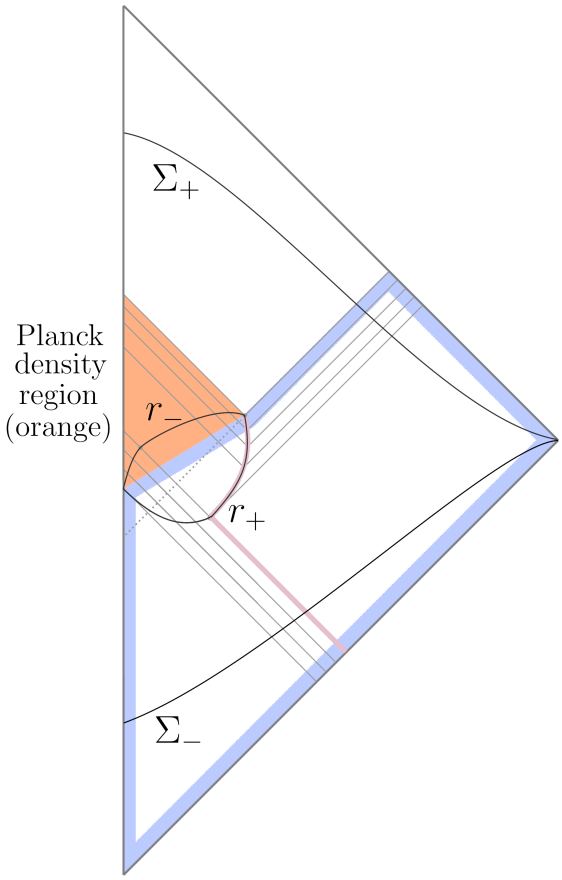

Figure 3.7: A spacetime like $\mathcal{M}$ but with a regular (nonsingular) center (see [241] for a detailed exposition with numerically computed causal diagrams). An inner apparent horizon (r_-) lies within a Planck density core (orange). The evaporation time and Page time unitarity problems, which are described entirely within the foliation Σ_u covering the early region (blue outline), are exactly the same here as in the singular case. Long term unitarity is viable in this background, unlike in $\mathcal{M}$, but depends on how initial data propagates through the strong quantum gravity region.

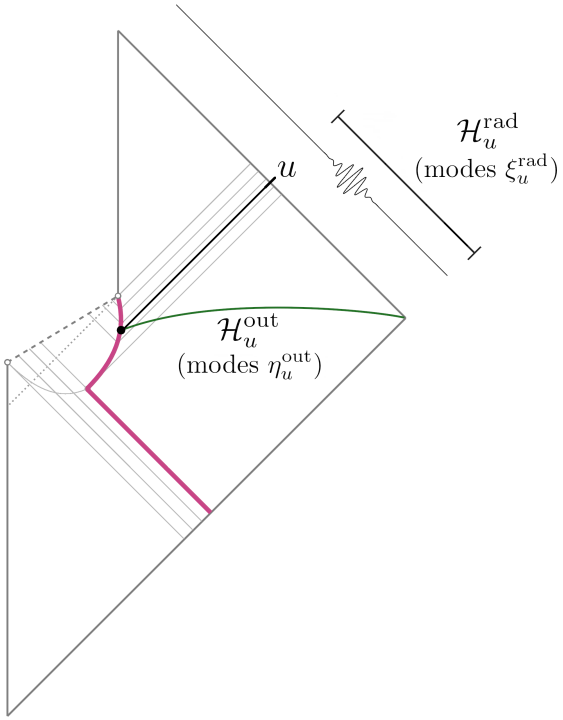

Figure 3.8: The entropy $S_{\text{rad}}(u)$ of outgoing Hawking modes up to time u is defined as von Neumann entropy in $\mathcal{H}_u^{\text{rad}}$, which is the Hilbert space of the modes ξ_u^{rad}. These ξ_u^{rad} are the subset of ξ^+ (Fig. 3.5) with wavepackets centered before time u. A different entropy, the von Neumann entropy in the out region $\mathcal{H}_u^{\text{out}} \equiv \mathcal{H}(\Sigma_u^{\text{out}})$, is discussed later.

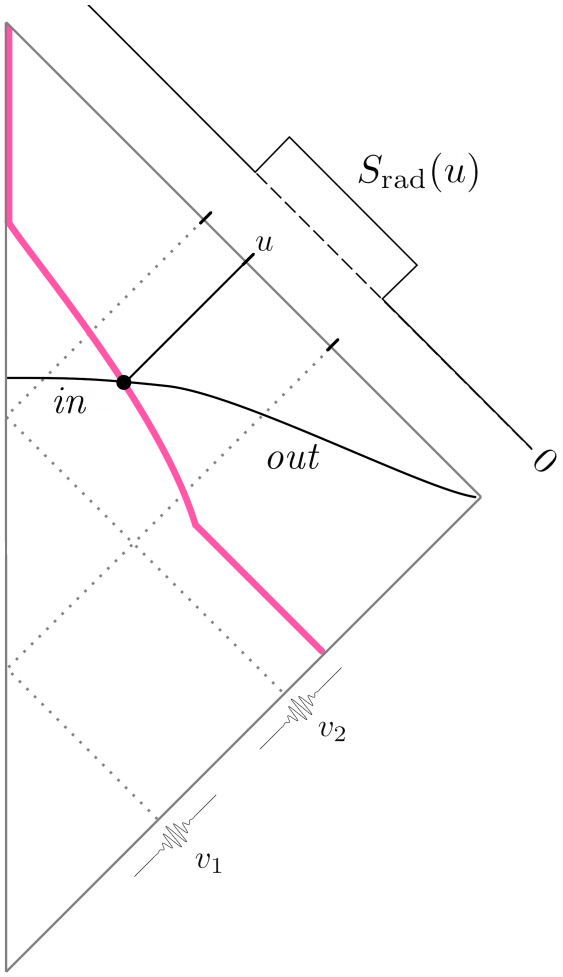

Figure 3.9: Minkowski space with fields in a state $|\psi\rangle = |1_{v_1} 1_{v_2}\rangle$ in terms of wavepacket modes similar to ξ^-. $S_{\mathrm{rad}}(u)$ rises when an entangled mode reaches infinity, then is purified to zero when its partner arrives. $S_{\mathrm{out}}(u)$, the von Neumann entropy in the *out* region (whose boundary is chosen to be analogous to $\mathcal{S}_{\mathrm{ext}}$ in $\mathcal{M}$), is UV-divergent due to vacuum entanglement, but can be argued to be related to $S_{\mathrm{rad}}(u)$ after renormalizing.

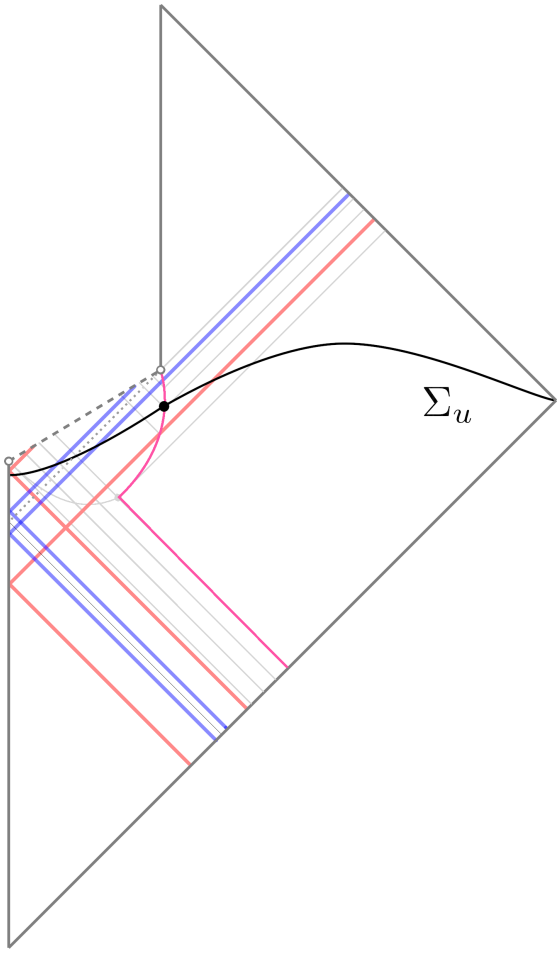

Figure 3.10: Early (red) and late (blue) pairs of entangled Hawking modes. As $u \to U$, later outgoing Hawking partners emerge into the *out* region, similar to the Minkowski space example of Fig. 3.9.

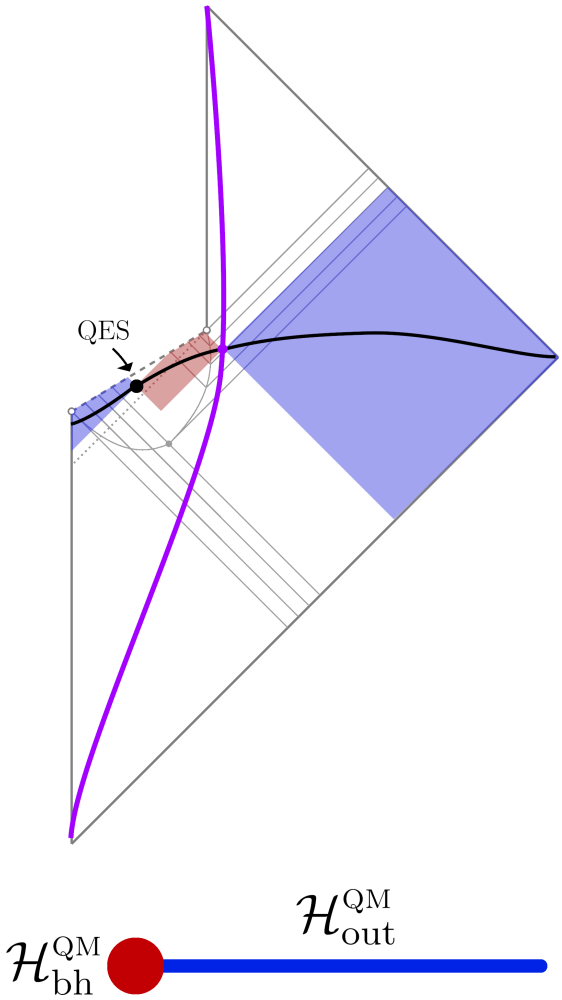

Figure 3.11: A "boundary" theory on $\mathcal{H}^{\mathrm{QM}} = \mathcal{H}^{\mathrm{QM}}_{\mathrm{bh}} \otimes \mathcal{H}^{\mathrm{QM}}_{\mathrm{out}}$ with a semiclassical "bulk" dual. Depicted is a time after the Page time during evaporation. The entanglement wedge of $\mathcal{H}^{\mathrm{QM}}_{\mathrm{bh}}$ (red fill) is bounded by a cutoff surface (purple line) and quantum extremal surface (QES). The entanglement wedge of $\mathcal{H}^{\mathrm{QM}}_{\mathrm{out}}$ (blue fill) includes an exterior region and an "island" near $r = 0$. Below is an illustration of the boundary theory where the holographic black hole Hilbert space (red dot) is coupled to a CFT (blue line). See Fig. 18 of [13] and Fig. 2 of [14], on which this picture is based, for details.

Part II

Numerical Simulation

Chapter 4

Bubble Dynamics

4.1 Introduction

This work aims to explore the behavior of the Coleman De Luccia (CDL) instanton [22, 65, 66] in coordinates inspired by the flat de Sitter slicing. Evolving the initial instanton in this coordinate system is of great interest because of recent proposals of multi-field scalar dynamics to create black holes and wormholes [75–77, 90, 105]. Our flat(ish) coordinates are a good choice for modeling this type of spacetime because of manifest spherical symmetry and limits to the flat Friedman-Lemaître-Robertson-Walker (FLRW) metric. These limits allow us to embed bubble nucleation and evolution into a realistic cosmology. A desire for a reasonable cosmology is the impetus for the use of this coordinate system over a global (compact) coordinate system as was described in [8].

There has been much work on bubble evolution and collision, see [4, 5, 37, 39,

54, 92, 97, 102–104, 148, 184] for a summary of the field. Several authors have (semi) analytically or numerically described scalar fields and especially colliding bubbles using the CDL instanton in hyperbolic coordinates [7, 128, 155, 274]. Because of our desire to retain spherical symmetry and limits to flat de Sitter, we will be simulating bubble walls in a novel coordinate system. In this work, we adapt the numerical code developed and used in [156, 268, 269] for the simulation of the spacetime of a single scalar field to observe and validate the behavior of the bubble wall. With this validation completed, future work can be done to simulate multi-field potentials and more interesting dynamics.

In Section 4.2, we discuss the scalar potential, the resulting instanton, and scale factor in Euclidean coordinates. In Section 4.3, we define the Lorentzian coordinate systems used throughout this paper. In Section 4.4, we introduce the equations of motion and solve for the initial state of our system. In Section 4.5, we present the simulation results and discuss the validation and convergence of our results. In Section 4.6, we present concluding thoughts and potential research avenues.

4.2 Finding the Instanton

We begin with the Euclidean instanton metric:

$$H_F^2\, ds^2 = dr_E^2 + \rho(r_E)^2\, d\Omega_3^2. \tag{4.1}$$

Here the radial coordinate is $r_E \in [0, \pi]$. $\rho(r_E)$ is the radius of the 3-sphere

and is zero at $r_E = 0, \pi$. This metric has $O(4)$ symmetry and is scaled by the false vacuum de Sitter radius, H_F^{-1}.[1] The instanton field $\varphi(r_E)$, like ρ, is simply a function of the radial coordinate r_E.

We use `CosmoTransitions` [267] with the addition of gravitational effects [269] to compute the instanton from our choice of scalar potential, shown in Fig. 4.1. This potential is from [173] with equation:

$$\begin{aligned} V(\varphi,\chi) = m^2(\varphi^2+\chi^2) - a(\varphi^2+\chi^2)^2 + \frac{c}{M_{\rm Pl}^2}(\varphi^2+\chi^2)^3 \\ + gM_{\rm Pl}^4 \sin\left(\frac{\varphi}{M_{\rm Pl}}\right) - jM_{\rm Pl}^4 \sin\left(\frac{\chi}{M_{\rm Pl}}\right) + hM_{\rm Pl}^4 \end{aligned} \tag{4.2}$$

We tabulate our choice of potential variables in Table 4.2 in Appendix 4.A.

For this work, we choose to make the second field, χ, constant to validate our simulation with previous single-field simulations. However, the coordinate system and numerical code allow both fields to evolve for more interesting dynamics. For the simulation, we rescale the potential such that the true vacuum value is $\frac{3}{8\pi}M_{\rm Pl}^4$. This results in the instanton profile and scale factor shown in Fig. 4.2.

4.3 Defining the Coordinates

4.3.1 Transforming the Instanton

The CDL instanton interpolates from true vacuum to false vacuum with a wall region in-between. It is useful and conventional to describe these regions with different

[1] For increasingly large bubbles, especially V3 and V4 (Table 4.2), we note that $r_E^{max} \lesssim \pi$ for this specific potential.

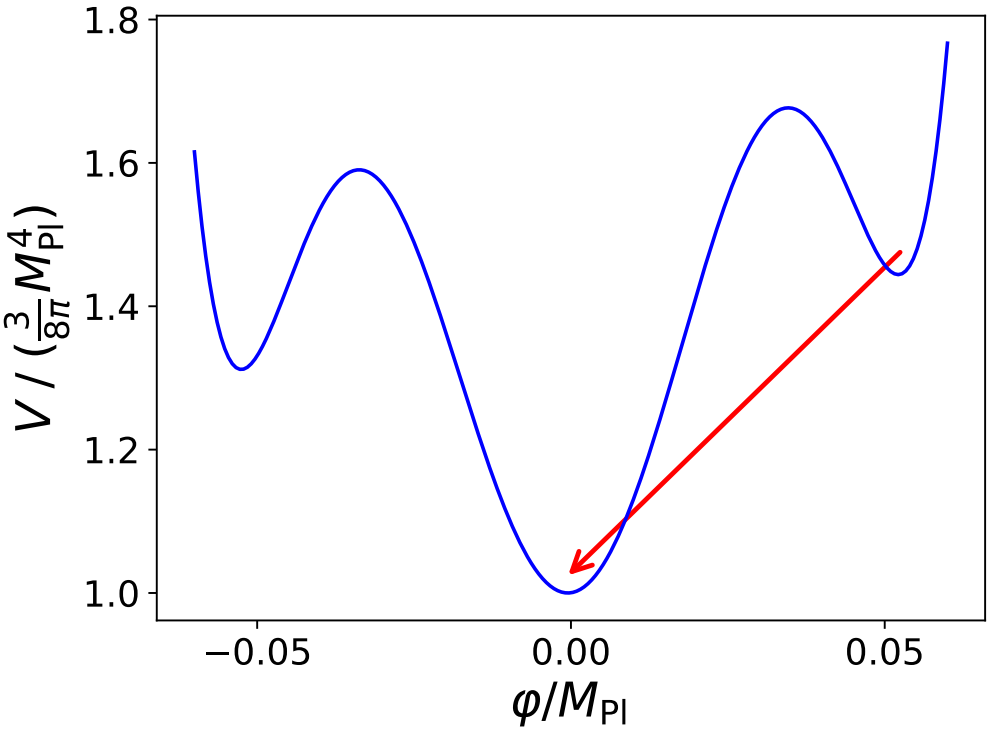

Figure 4.1: Scalar potential with true vacuum at $\varphi \sim 0.0\, M_{\rm Pl}$, $V_{\rm min} = \frac{3}{8\pi} M_{\rm Pl}^4$ giving $H_T^{-1} = M_{\rm Pl}^{-1}$. The instanton tunnels from the false vacuum $\varphi \sim 0.053\, M_{\rm Pl}$. This is the potential V1 of Table 4.2.

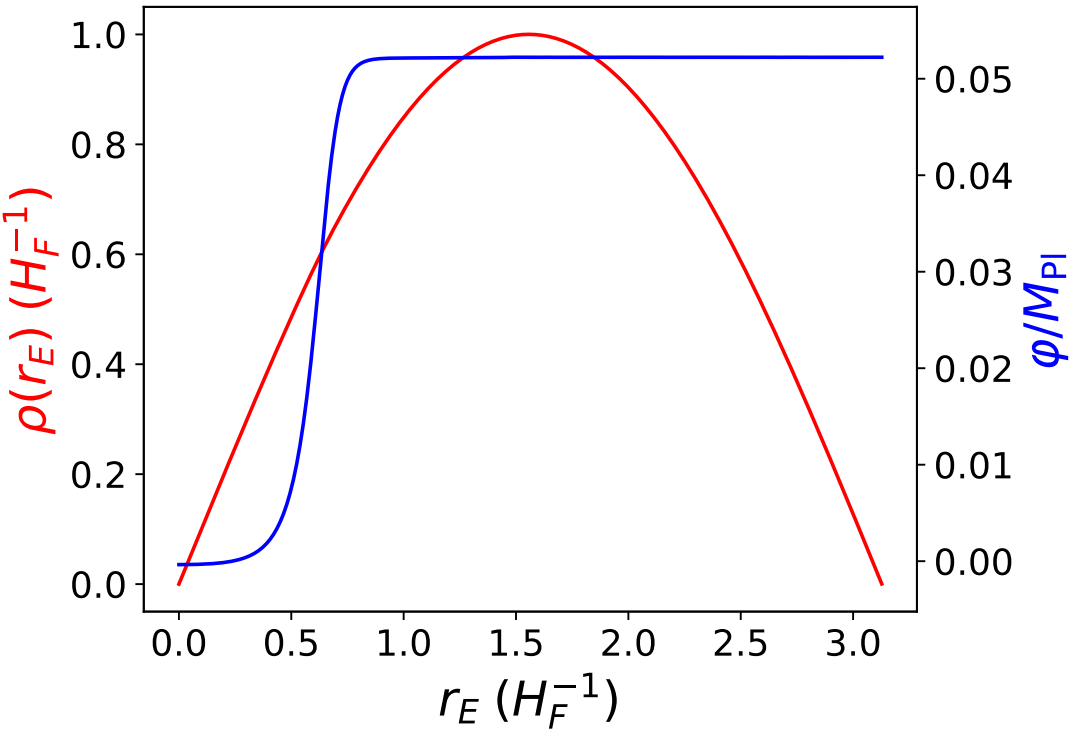

Figure 4.2: Scale factor and instanton profile for V1 of Table 4.2.

coordinate systems. To get the *true vacuum* coordinates with spherical symmetry, we follow [7] and write the metric with the appropriate scale factor to match the wall region[2] at $\tau = r_E = 0$:

$$ds^2 = -d\tau^2 + a(\tau)^2 \left[d\xi^2 + \sinh^2 \xi \, d\Omega_2^2\right] \tag{4.3}$$

These coordinates are the familiar open coordinates in de Sitter space (for the particular choice of $a(\tau) \propto \sinh \tau$).

Now for the *wall region* we take [7]:

$$\theta \to i\xi + 3\pi/2 \tag{4.4}$$

in the instanton metric Eq. 4.1, giving a wall-region metric of:

$$H_F^2 \, ds^2 = -\rho(r_E)^2 d\xi^2 + dr_E^2 + \rho(r_E)^2 \cosh^2 \xi \, d\Omega_2^2. \tag{4.5}$$

Here we have a new time coordinate ξ, and the $3\pi/2$ results in a $\cosh \xi$ from the angular coordinate on the initial 3-sphere. r_E remains the radial coordinate.

The *false vacuum* region can be covered by coordinates analogous to the open slicing used in the true vacuum, beginning at $r_E = \pi$ ($r_E^{\max}$) rather than $r_E = 0$.

While this patchwork of coordinates is useful for understanding the individual regions, for a numerical simulation of the full spacetime of a bubble nucleation we need

[2]The authors of [7] note that $\{r_E \to i\tau, \theta \to i\xi\}$ of Eq. 4.1 gives Eq. 4.3.

coordinates that cover all three regions at once; constructing this single coordinate system and tying it to the three patches so that the results can be understood is a core challenge of this work. In the next section we connect the three coordinate systems through their embedding in higher-dimensional Minkowski space, then in Sec. 4.3.3 we describe the global coordinates we use for the numerical calculation.

4.3.2 Minkowski Space Embedding

We start with 5D Minkowski:

$$ds^2 = -dX_0^2 + dX_4^2 + \sum_i dX_i^2. \tag{4.6}$$

In our application, we need to consider two different vacuum energies and, thus, two different hyperboloids, each inducing a de Sitter space metric with a different scale. To determine the radii of the hyperboloids, we calculate the Hubble radii with $V_{T,F}$, the minima for true and false vacua, respectively:

$$H_{T,F}^{-1} = \sqrt{\frac{3M_{\rm Pl}^2}{8\pi V_{T,F}}}. \tag{4.7}$$

We consider an initial false hyperboloid and glue a true hyperboloid along constant $X_4^W = H_F^{-1}\sqrt{1-R_0^2}$ [104], a timelike slice, starting at $X_0 = 0$. Where R_0 is the initial radius of curvature of the bubble in units of H_F^{-1}. See Fig. 4.3 for a picture of the gluing. This choice of X_4 breaks pure de Sitter's SO(4,1) symmetry to SO(3,1). With this glued hyperboloid, we can match our three coordinate regions from

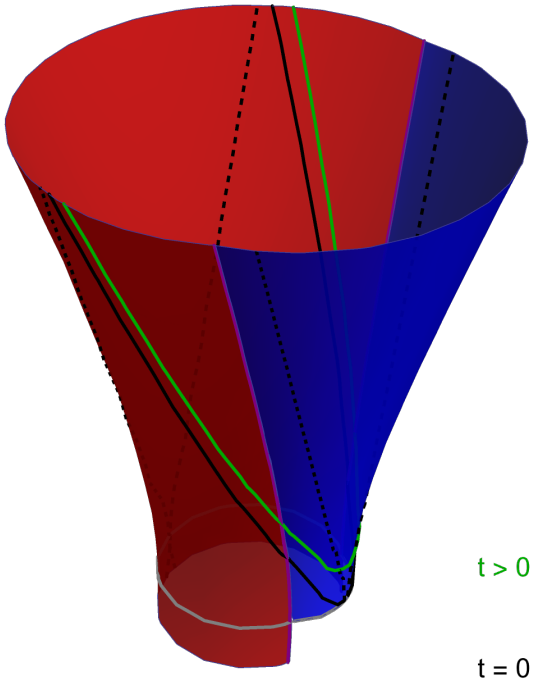

Figure 4.3: 3D True (blue) and False (red) Hyperboloids glued together with $H_F^{-1} = 0.7H_T^{-1}$. Two flat time slices $t = 0$, $t > 0$, a gray deformed circle at $X_0 = 0$, and dashed black boundaries of the wall region are drawn. Two additional dimensions are hidden.

Section 4.2.

To smoothly match the glued hyperboloids at X_4^W, we must shift the true vacuum hyperboloid by $X_4^S = X_4^W - \sqrt{H_T^{-2} - H_F^{-2}R_0^2}$. This shift aligns the R_0 radius of curvature region of the two hyperboloids at X_4^W when $X_0 = 0$. In the limit of vanishing bubble radius, we obtain $X_4^W = H_F^{-1}$ and $X_4^S = -H_T^{-1} + H_F^{-1}$, where both hyperboloids are aligned at $X_4 = H_F^{-1}$ at zero radius of curvature. In Fig. 4.4, we can see that the red *false* vacuum hyperbola is centered at $X_4 = 0$, while the blue *true* vacuum hyperbola is shifted by X_4^S.

While Figs. 4.3, 4.4 represent the same spacetime, they tell a slightly different

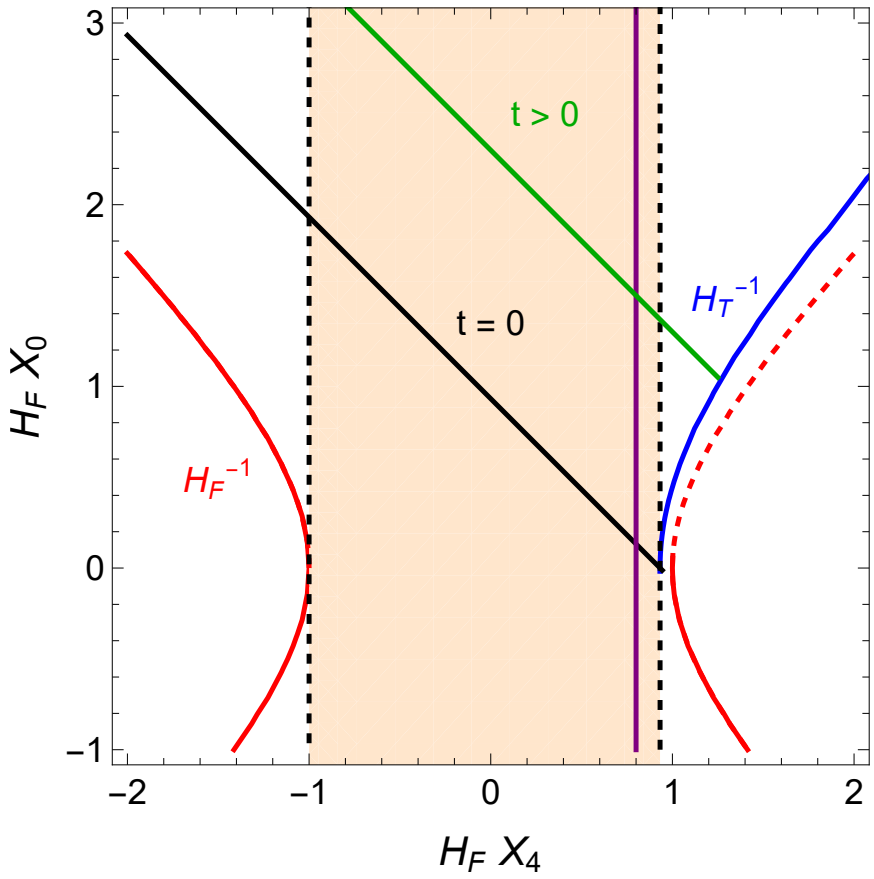

Figure 4.4: True (blue) and False (red) Hyperboloids glued together at $H_F X_4 = 0.6$ in purple, with $H_F^{-1} = 0.7 H_T^{-1}$. Two flat time slices are drawn at $t = 0$, $t > 0$, and the wall region is shaded in orange. Three additional dimensions are hidden.

story. Fig. 4.3 highlights the two hyperboloids with different radii glued together. It would be easy to believe this figure is telling us there are actually two physical regions rather than three, but we caution the reader from this conclusion. Fig. 4.4 does a better job of conveying the three regions of the Lorentzian instanton. Outside of the orange wall region, we are in pure de Sitter space (true or false), while inside the orange region, the curvature varies with radius. The bubble wall (instanton radius) is centered around the purple line (hyperbola), and this is where the curvature changes from false to true de Sitter. Naturally, the wall region contains the bubble wall, but away from the bubble wall, the curvature in the wall region is very close to either false or true de Sitter.

The wall region is the bounded area between the two open-slicing vacuum regions. Its boundaries are shown in Fig. 4.4 as the black vertical lines and it is shaded in orange. To embed it in our Minkowski space we need an embedding that has zero radius of curvature on the boundaries, $X_4 = \left\{ H_T^{-1} + X_4^S = H_T^{-1} + \sqrt{H_F^{-2} - R_0^2} - \sqrt{H_T^{-2} - R_0^2}, -H_F^{-1} \right\}$ at $X_0 = 0$. We reproduce the wall region metric using the embedding[3]

$$\begin{aligned} X_0 &= H_F^{-1} \rho(r_E) \sinh(\xi), \\ X_4 &= H_F^{-1} h(r_E), \\ X_i &= H_F^{-1} \rho(r_E) \cosh(\xi)\, \omega_i, \end{aligned} \tag{4.8}$$

where h is a function to be solved for that makes X_4 depend on (only) r_E. Due to the instanton symmetry, $\rho(r_E)$ and $\varphi(r_E)$ must both be functions of only r_E. The mapping

[3]The embedding coordinates are constructed to match Eq. 4.5 when substituted into Eq. 4.6 [8].

$h(r_E)$ can then be solved for by using Eqs. 4.5, 4.6, and 4.8 to give $h'(r_E)^2 = 1 - \rho'(r_E)^2$. Solving this differential equation provides invertible mapping, $r_E \leftrightarrow X_4$.

Having all three coordinate patches in the same embedding now allows us to construct a global coordinate system by slicing through this patched-together embedded spacetime in a manner analogous to the construction of the flat slicing coordinates of standard de Sitter spacetime.

4.3.3 Flat(ish) slicing

Although flat-slicing coordinates are not the ones perfectly adapted to the metric in any of the three regions, they cover all three. Moreover, far away from the bubble wall at both large and small radius, we have constant vacuum energy, and in these limits, a (truly) flat slicing is accurate and also provides a clear interpretation.

For the simulation, we will be considering general spherically-symmetric metrics of the form:

$$H_T^2\, ds^2 = -\alpha(t,r)^2 dt^2 + e^{2H_T t} \times [a(t,r)^2\, dr^2 + b(t,r)^2\, r^2\, d\Omega^2] \tag{4.9}$$

On our initial surface, $t = 0$, to agree with flat-sliced de Sitter in the small-

and large-r regimes, we expect limits:

$$\begin{aligned} \alpha_{r\to 0} &= 1, \\ \alpha_{r\to\infty} &= H_F^{-1} H_T, \\ a &= 1, \\ b &= 1. \end{aligned} \tag{4.10}$$

This choice of metric is spherically symmetric and already in the Arnowitt–Deser–Misner (ADM) decomposition with the shift vector set to zero (see Sec. 4.4.1). Note that we removed the exponential from the definitions of a, b.

4.3.3.1 Naive Flat Embedding

The true vacuum flat slicing in the embedding coordinates is [8]:

$$\begin{aligned} X_0 &= H_T^{-1} \sinh(H_T t) + \frac{H_T^{-1}}{2} e^{H_T t} r^2, \\ X_4 &= X_4^S + H_T^{-1} \cosh(H_T t) - \frac{H_T^{-1}}{2} e^{H_T t} r^2, \\ X_i &= H_T^{-1} r e^{H_T t} \omega_i. \end{aligned} \tag{4.11}$$

Notice that a shift by X_4^S in X_4 has been applied to make the hyperboloid joining surface smooth, as seen in Fig. 4.3. The Hubble radius is chosen to match the true vacuum to align the $r = 0$ surface with the true vacuum hyperboloid, see $t = 0$ black line in Fig. 4.4. Also, the coordinate r is in units of H_T^{-1}.

Eq. 4.11 results in a de Sitter space metric, Eq. 4.9, with $\{\alpha = 1, a = 1, b = 1\}$. This solution only really holds in the limit of degenerate minima ($H_T \sim H_F$) and no wall, as Eq. 4.11 assumes the entire spacetime is true vacuum. Now we need an embedding with similar properties, but that allows for more freedom in the metric functions so that we can interpolate from true to false vacuum.

4.3.3.2 Picturing Naive Flat Coordinates

Although the naive embedding is not satisfactory for representing the initial state of this system, we can use it to build intuition for the relations between coordinates.

We plot two spacetimes in Figs. 4.5, 4.6 where the first assumes the naive embedding, Eq. 4.11, and the second uses the compact coordinates of reference [8]. Both of these pictures require degenerate vacua, and in this work, we will only consider down to 2% different de Sitter radii (sample V4). In practice, this means that we can only trust the picture for $r < r^{\text{wall}}$, where we are closer to the true vacuum. For this shape potential (Eq. 4.2), we note that as the false vacuum is raised further from true vacuum, we get smaller radius instantons. As this picture requires nearly degenerate vacua, the approximation becomes worse as our instanton becomes smaller radius. The compact picture is included to give the reader a more familiar picture of the bubble spacetime before continuing with the trickier flat(ish) coordinates.

In Fig. 4.5 we plot the wall region boundaries, $X_4 = \left\{H_T^{-1} + \sqrt{H_F^{-2} - R_0^2} - \sqrt{H_T^{-2} - R_0^2}, -H_F^{-1}\right\}$ with thick black lines as function of flat coordinates (these are also the thick black lines in Fig. 4.6). In the wall coordinates, these values remain at

$r_E = \{0, \pi\}$, and the wall radius is fixed at $r_E = r_E^{\text{wall}}$. Note that in Fig. 4.5, r is *not* compact like η in Fig. 4.6 and thus increases without bound. As t increases, the constant X_4 begin to converge on $r = 1$ (H_T^{-1}). In our simulation we will see that our bubbles approach H_F^{-1} and *not* H_T^{-1} as is suggested by this naive coordinate system. It is key to remember that the flat coordinate r is a comoving coordinate. If we want to consider physical size we need to tack on $e^{H_T t}$ (see top panel of Fig. 4.11).

We also depict three red curves in each plot, which are constant time surfaces in the opposite coordinate system (compact $\leftrightarrow$ flat). This helps to show the non-trivial conversion between the two coordinate systems.

4.3.3.3 Flat(ish) Embedding

Starting with the basic form of Eq. 4.11 we introduce some unknown functions:

$$\begin{aligned} X_0 &= f_0(t) + H_T^{-1} g_0(t, r)\, e^{H_T t}, \\ X_4 &= X_4^S + f_4(t) - H_T^{-1} g_4(t, r)\, e^{H_T t}, \\ X_i &= H_T^{-1} r e^{H_T t} \omega_i. \end{aligned} \tag{4.12}$$

Importantly, our new embedding retains the X_i component as we still want $b = 1$ solution for limits matching flat FLRW.

Substituting the embedding definitions into the Minkowski metric and com-

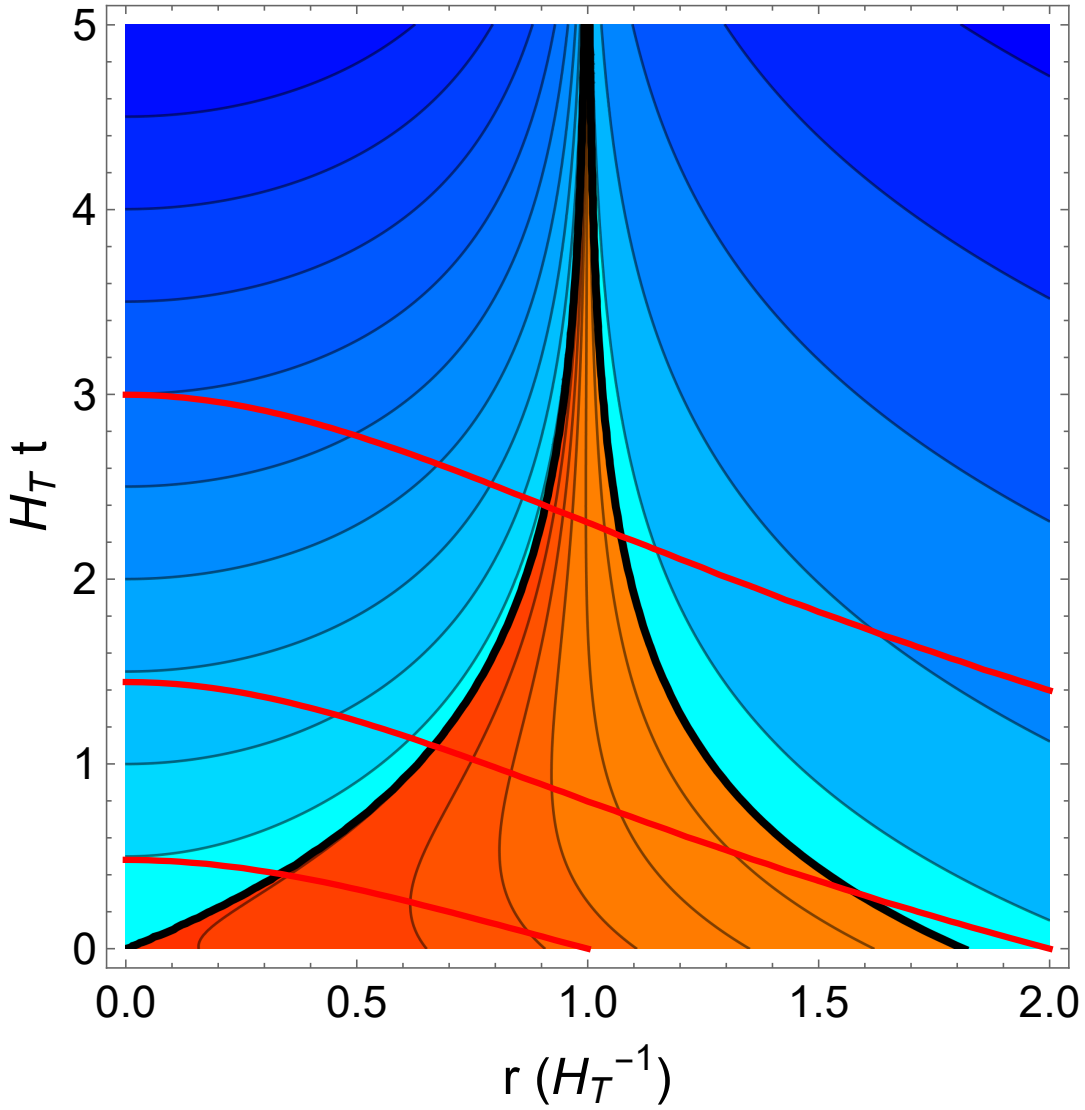

Figure 4.5: Open coordinates cover the *true* (left) and *false* (right) regions, and wall coordinates cover the region between. Three compact times (T) drawn in red. Contours are constant X_4, largest in the top left true vacuum region and decreasing counterclockwise.

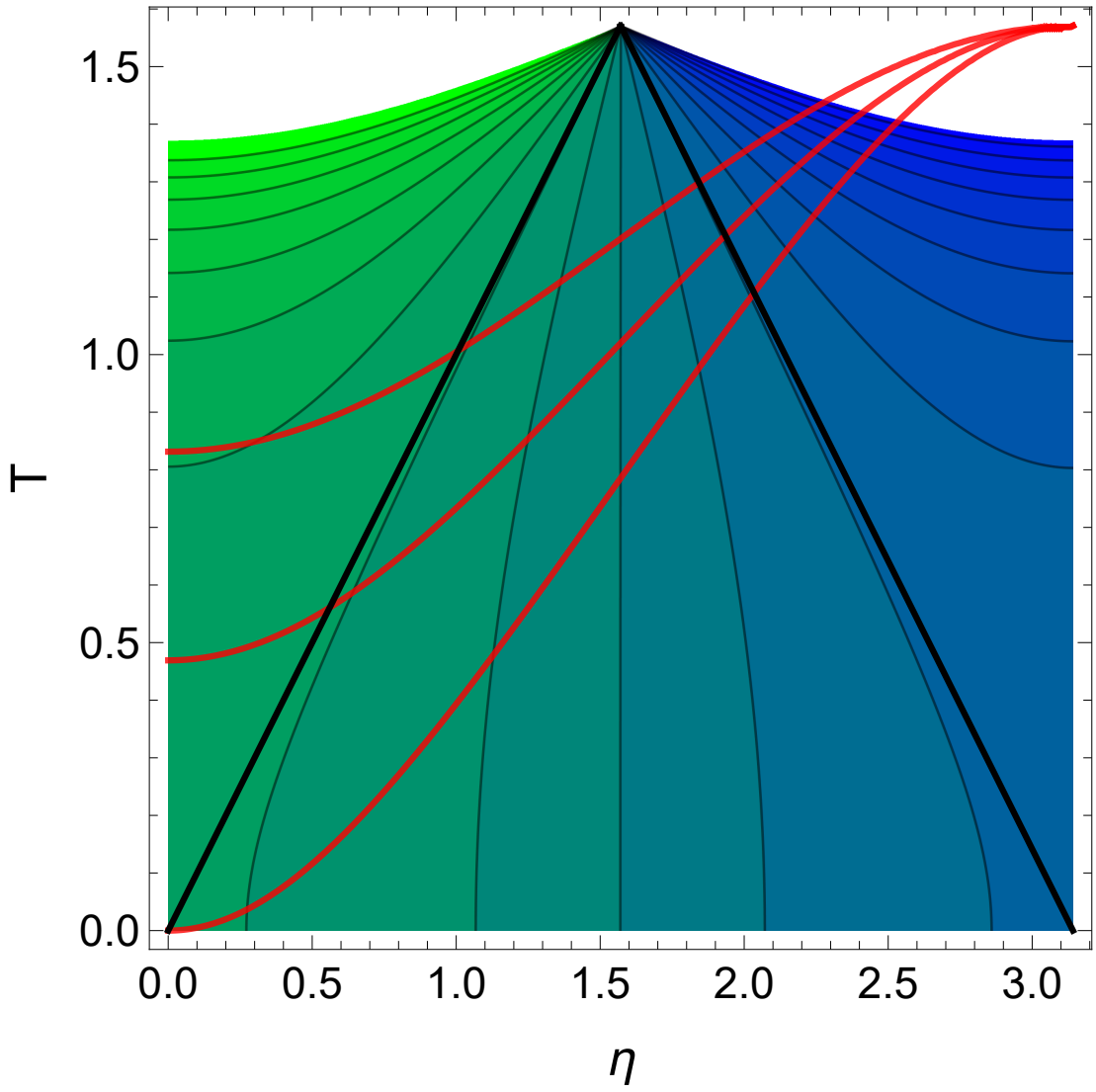

Figure 4.6: Compact coordinates (T, η) defined in **Eq. 12** of [8]. Three flat slicing times (t) drawn in red. Contours are constant X_4 and decrease counterclockwise, starting in the top left true vacuum region toward the central wall region, and top right false vacuum.

paring to Eq. 4.9, we get the following for the dr^2 component:

$$a^2 = 1 - g_0'^2 + g_4'^2. \tag{4.13}$$

We would like the flat-slice property where $X_0 + X_4$ has no radial dependence, but we will have to settle for this being accurate in the limit of small (large) radius, where we are in pure de Sitter.

This implies that if we have pure de Sitter ($a = 1$, $\alpha = const.$) then $g_0(t, r) - g_4(t, r)$ is a function of t only. Now, if we consider $X_0 + X_4$ at small radius we should agree with the naive embedding, Eq. 4.11, because we are deep in the true vacuum regime. Because f_0, f_4 are radially independent, we can set them to their naive solutions of $f_0 = H_T^{-1} \sinh H_T t,\ f_4 = H_T^{-1} \cosh H_T t$.

Furthermore, there is an equation for α^2 (dt^2 component) analogous to Eq. 4.13 that contains temporal derivatives of functions $g_0,\ g_4$. After running the simulation to determine $\{a,\ \alpha\}$, we can combine these equations to write a differential equation for our unknown functions g_0 and g_4.[4]

4.3.4 Initial Slice Coordinate Transformation

The instanton provides us with field and metric components in all three regions. In order to find initial conditions for the bubble in our flat(ish) coordinates (t, r), we will need to relate them to the coordinates (ξ, r_E) in the wall region, on the initial $(t = 0)$

[4]In practice, we need to make some more simplifying assumptions, such as temporal derivatives tending to zero at late times, to solve this differential equation. See Appendix 4.B for more discussion.

slice.

We can characterize this $t = 0$ slice in the wall region by finding ξ as a function of r_E by matching the embeddings Eqs. 4.8 and 4.12 with $t = 0$. To do this, we first match the X_i pieces between the embeddings, to get $H_T^{-1} r = H_F^{-1} \rho(r_E) \cosh(\xi)$, then we match $X_0 + X_4$ to get $f_0(0) + f_4(0) + X_4^S = H_F^{-1} \rho(r_E) \sinh(\xi) + H_F^{-1} h(r_E)$. We finally combine the two equations and substitute in our solutions for $f_0,\ f_4$ to solve for ξ at $t = 0$.

$$\xi_{t=0}(r_E) = \operatorname{arcsinh}\left[\frac{H_T^{-1} + X_4^S - h(r_E)}{H_F^{-1}\rho(r_E)}\right]. \tag{4.14}$$

Then, we obtain the mapping between r and r_E using our X_i matching again:

$$H_T^{-1} r_{t=0}(r_E) = \sqrt{[H_T^{-1} + X_4^S - H_F^{-1} h(r_E)]^2 + H_F^{-2} \rho(r_E)^2}. \tag{4.15}$$

This mapping is plotted in Fig. 4.7. We now have the coordinate transformations at $t = 0$ and we will return to solve for all metric functions and derivatives on the initial slice in Sec. 4.4.3.

4.4 Simulation Setup

4.4.1 Simulation Coordinates

For simulating the bubble we will redefine our time coordinate to $N \equiv H_T\, t$, making it dimensionless and in units of the true vacuum de Sitter radius, like r. As

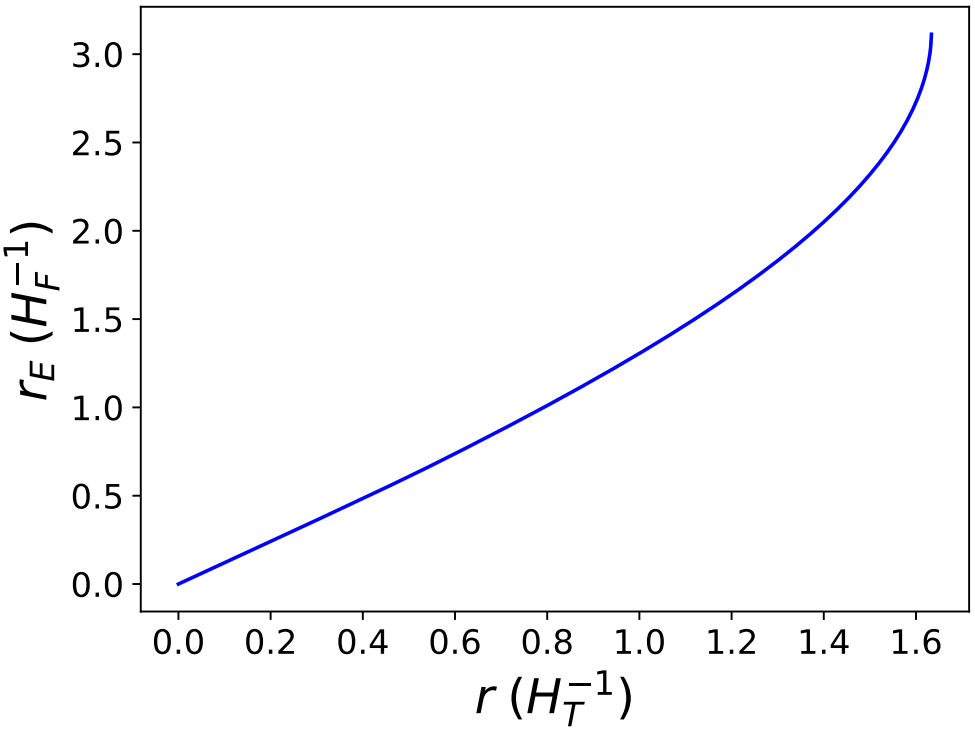

Figure 4.7: Conversion of Euclidean radial coordinate to flat radial coordinate on $t = 0$ surface for V1 of Table 4.2.

mentioned in Sec. 4.2, we scale the scalar field potential such that the true vacuum has value $V_T = \frac{3}{8\pi}$. This gives us a de Sitter radius of $H_T^{-1} = 1$ for $M_{\rm Pl} = 1$, which we will use for the remainder of the simulation. We will continue to write H_T^{-1} instead of setting it equal to 1, but the important scale is now H_F^{-1} / H_T^{-1} or just H_F^{-1}.

We rewrite our metric of Eq. 4.9 with $t \to N$:

$$H_T^2\, ds^2 = -\alpha(N,r)^2 dN^2 + e^{2N} \times \left[a(N,r)^2\, dr^2 + b(N,r)^2\, r^2 d\Omega^2 \right]. \tag{4.16}$$

Our next task is to write out the equations of motion for our new coordinates.

4.4.2 Equations of Motion

We follow the method of Johnson et. al (see **App. A** in [155], a discussion on the ADM formalism [64], and a review of numerical relativity [175]) in deriving the time evolution equations for our metric functions and scalar fields using the metric Eq. 4.16.

4.4.2.1 Lapse and Shift Gauge Choices

Choosing a coordinate system does not fully specify the initial state of the system, and we are required to make additional gauge choices for the lapse and shift [28].

First, we make the simplifying gauge choice of zero shift, $\beta^r = 0$.

In line with [155], we write the time derivatives of a and b as:

$$\begin{aligned} \dot{a} &= -a\,(1 + K^{r}{}_{r}\,\alpha), \\ \dot{b} &= -b\,(1 + K^{\theta}{}_{\theta}\,\alpha), \end{aligned} \tag{4.17}$$

which come from the definition of extrinsic curvature (K) found in [28].

Next, we make another simplifying gauge choice for the lapse, $\alpha = -1/K^{\theta}{}_{\theta}$. This results in b being a constant in time.

4.4.2.2 Evolution Equations

All of the following functions are functions of (N, r) unless otherwise stated. Note that here $V = V(N, r)$, which is equivalent to $V(\varphi_1(N, r), \varphi_2(N, r), \ldots, \varphi_n(N, r))$. We define the derivatives of the kth scalar field:

$$\begin{aligned} \Phi_k &\equiv \varphi_k', \\ \Pi_k &\equiv \frac{a}{\alpha}\dot{\varphi}_k \end{aligned} \tag{4.18}$$

We denote the derivatives of f as $f'(N, r) \equiv \partial_r f(N, r)$ and $\dot{f}(N, r) \equiv \partial_N f(N, r)$.

We now write the time evolution equations:

$$\dot{a} = e^{-2N} \times \alpha^2 \Bigg\{ \frac{1}{2r^2a^2b^2}\, a\, (-a^2+b^2) + \frac{1}{ra^2b}\, (-ba' + 3ab') + \frac{1}{2a^2b^2}\, (-2ba'b' + ab'^2 + 2abb'') + \frac{2\pi}{a^2}\, a \sum_k \Phi_k^2 \Bigg\} + \frac{1}{2}\, (-a)\, [3 - 8\pi V\alpha^2] + \frac{2\pi\alpha^2}{a^2}\, a \sum_k \Pi_k^2 \tag{4.19}$$

$$\dot{b} = 0 \tag{4.20}$$

$$\dot{\alpha} = e^{-2N} \times \alpha^2 \Bigg\{ \frac{1}{2r^2a^2b^2}\, \alpha\, (a^2-b^2) + \frac{1}{ra^2b}\, (-b\alpha' - \alpha b') + \frac{1}{2a^2b^2}\, (-2bb'\alpha' - \alpha b'^2) + \frac{2\pi}{a^2}\, \alpha \sum_k \Phi_k^2 \Bigg\} + \frac{1}{2}\, \alpha\, [3 - 8\pi V\alpha^2] + \frac{2\pi\alpha^2}{a^2}\, \alpha \sum_k \Pi_k^2 \tag{4.21}$$

$$\dot{\varphi}_k = \frac{\alpha}{a}\Pi_k \tag{4.22}$$

$$\dot{\Pi}_k = e^{-2N} \times \frac{1}{a}\left\{\frac{2}{r}\alpha\Phi_k + \frac{1}{ab}\alpha\Phi_k(-a'b + 2ab') + \alpha'\Phi_k + \alpha\Phi_k'\right\} - 3\Pi_k - a\alpha\frac{\partial V}{\partial\varphi_k} \tag{4.23}$$

There are many similarities between the forms $\dot{a}$ and $\dot{\alpha}$ equations (Eq. 4.19, 4.21). However, there are some sign differences that have important consequences for the shapes of a, α during evolution. The signs of the potential terms ($\propto V$) are opposite for a and α. For α evolution, this results in a cancellation of the term proportional to V and the terms proportional to the field derivatives (Φ, Π), while for the evolution of a, there is an additive effect.

In each of the evolution equations, the terms grouped in curly braces have a e^{-2N} suppression factor. The terms proportional to $1/r, 1/r^2$ are deemed transients because their contribution to evolution dies quickly over time, especially for $N > 1$. Although there are different time regimes for which terms are relevant, all terms are included in the calculation at all times during the simulation. For the purposes of our simulation, all b derivatives are zero because of our choice of initial state and gauge fixing.

Finally, our last evolution equation, Eq. 4.23 is derived from the Klein Gordon equation for scalar field evolution.

4.4.3 Initial Conditions

We need to solve for the initial state of the system that has the correct symmetries to match the CDL instanton and solve our derived evolution equations. We take our metric functions and scalar fields as Taylor expansions in N.

$$a(N, r) = a_0(r) + a_1(r)N + \mathcal{O}(N^2) \tag{4.24}$$

From here on out, we will use subscripts to represent the order in the Taylor series in time N. To not confuse with the Sec. 4.4.2 usage of subscript k to represent scalar field k, we will only consider the case of two scalar fields φ, χ, where the latter does not participate in the dynamics in this work.

We would like to retain FLRW limits, so we enforce $a_0, b_0 = 1$. This defines $N = 0$ as a space-like spatially flat (3-curvature) surface. The rest of the choices for our simulation parameters can be found in Table 4.2. We take Taylor expansions of Eqs. 4.19 - 4.23 to 2nd order in all functions except for φ, which we can calculate to 3rd order. This allows us to satisfy all evolution and constraint equations to at least 1st order. Satisfying these gives us the initial state functions which we write down for $\{\alpha_0', a_1, b_1, \alpha_1, \varphi_2\}$ in Eq. 4.25. To solve these equations, we now need to add in the initial data for the instanton initial state.

$$\alpha_0'(r) = -\alpha_0(r)\,\frac{1}{2r}\left\{-3\,+4\pi\,\alpha_0(r)^2\,[2V(r)+\varphi_0'(r)^2]+4\pi[\varphi_1(r)^2-2r\varphi_1(r)\varphi_0'(r)]\right\},$$

$$a_1(r) = -\frac{3}{2}\,+2\pi\,\alpha_0(r)^2\,[2V(r)+\varphi_0'(r)^2]+2\pi\varphi_1(r)^2,$$

$$b_1(r) = 0,$$

$$\alpha_1(r) = -\frac{1}{r}\alpha_0'(r)\alpha_0(r)^2+\frac{1}{2}\,\alpha_0(r)\big\{3-4\pi\alpha_0(r)^2[2V(r)-\varphi_0'(r)^2]+4\pi\varphi_1(r)^2\big\},$$

$$\varphi_2(r) = -\alpha_0(r)\,\frac{1}{2r}\left\{-2\varphi_0'(r)\alpha_0(r)-r\alpha_0'(r)\varphi_0'(r)-r\varphi_0''(r)\alpha_0(r)+r\alpha_0(r)\frac{V'(r)}{\varphi_0'(r)}\right.$$
$$\left.+\,8\pi rV(r)\alpha_0(r)\varphi_1(r)+\varphi_1\alpha_0'(r)\right\} \tag{4.25}$$

Notice that each of these equations depends on the undetermined α_0 and φ_1. We can use the fact that we know the wall region metric (Eq. 4.5) at $t = N = 0$ to calculate the Ricci curvature in the wall region coordinates (ξ, r_E) and then convert to our simulation coordinates using Eq. 4.15. Next, we can calculate the Ricci curvature using the simulation metric (Eq. 4.16) at $N = 0$ and set these equal to each other to solve for our unknowns.

The first step is to solve for α_0 as a function of φ_1 using $R^{(4)}$ written in our Taylor expanded functions, then substitute it into the α_0' equation, Eq. 4.25. We can then rewrite the α_0' equation into a φ_1' equation and solve for φ_1. Interestingly, there is some degeneracy of solutions because $R^{(4)}$ depends on the ratio of $(\varphi_1/\alpha_0)^2$, so we need an extra piece of information to nail down the overall sign of φ_1 and thus the shape of α_0. Knowing φ_1, we can solve for α_0 using our knowledge of $R^{(4)}$.[5]

[5] Additionally, we can calculate the Kretschmann scalar to confirm we have the correct overall scale

To find the appropriate sign for φ_1, we will use our naive picture for intuition. The scalar field in the coordinates of the wall region should follow a constant $r_E \leftrightarrow X_4$ [6]. If we could plot the path $X_4 = X_4^{\text{wall}}$ follows, we would have our answer. Consider Fig. 4.5 and look at the contours in the wall region (constant X_4). They are decreasing in radius for small t (N). However, remember this is a naive picture using the embedding Eq. 4.11 which we know only has a limited domain of $r \lesssim r^{\text{wall}}$. We expect to have a reasonable agreement between the naive and flat(ish) embeddings at small radius at early time because we are close to pure true vacuum de Sitter space (see Fig. 4.14).

Now, we look at dt/dr of the contours in Fig. 4.5 for $r \lesssim r^{\text{wall}}$ and see that they are initially negative, meaning that the comoving radius initially contracts. We believe it reasonable to expect a smooth change in the slope of dt/dr as we change the radius in both directions. This means that smaller instantons will decrease less in radius compared to larger ones. Eventually, we expect the initial decrease to go to zero for minuscule bubbles, and we return to the original infinitesimally thin CDL bubble of [65, 66]. However, in this work, we will only consider bubbles with $R_0 > 0.5$ (H_F^{-1}) radius of curvature.

We know that our bubble initially decreases in time, but what does this mean for the sign of φ_1? Looking at Fig. 4.8, we include a dashed red lines which is the approximate shape of φ at $N \gtrsim 0$, $\varphi_0 + \varphi_1 \times 0.05$. Because φ_1 is positive, the bubble wall moves to the left, to smaller radius. This result depends on whether the field

for φ_1 and shape for α_0. However, we only need $R^{(4)}$ to fully solve for our initial state. Other scalars are zero for this metric due to the high level of symmetry.

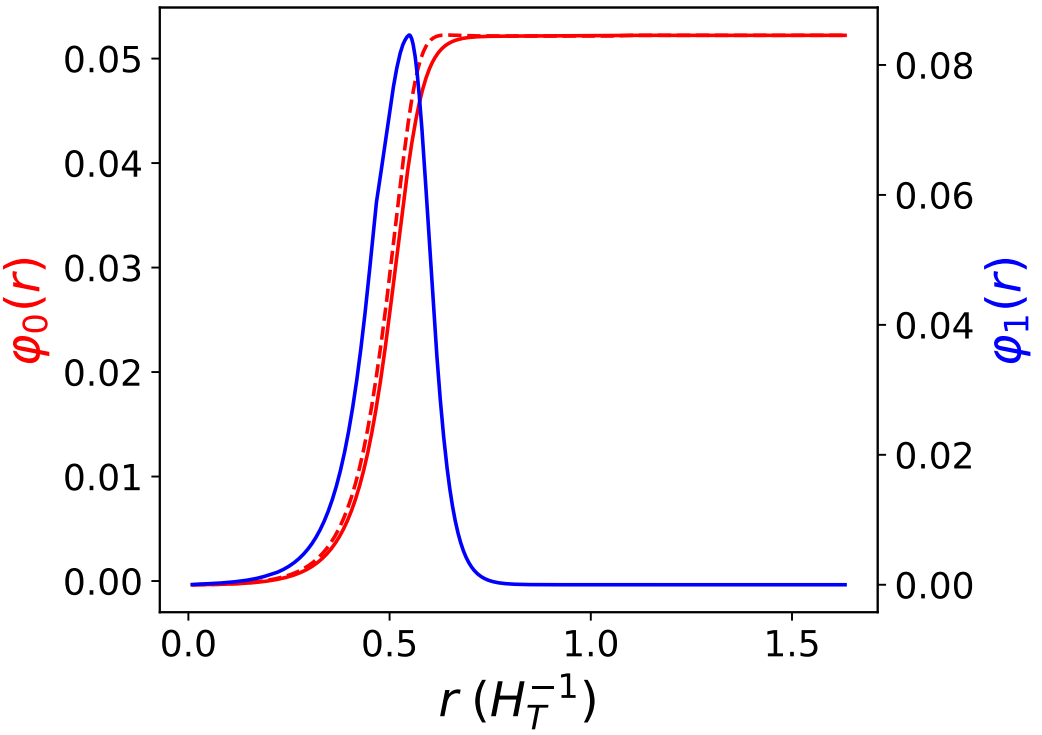

Figure 4.8: Initial field and time derivative profiles for V1 of Table 4.2. In dashed red, we draw $\varphi_0 + \varphi_1 \times 0.05$ to show the initial leftward movement of the field.

tunnels to a larger or smaller field value, where the sign would flip for φ_1. Finally, we can say that we want the positive solution for φ_1 for initially shrinking bubbles, and our initial state is solved for.

4.4.4 Numerical Method

The numerical code used in this work was first developed in [269]. For a detailed description of the algorithm, see the previous work. We will summarize the relevant information here.

The code employs the method of lines [28] with adaptive mesh refinement (AMR) [1, 176]. As we will see, the bubble wall becomes length-contracted during the simulation and our functions develop large gradients. We need a non-uniform grid that has higher density near large gradients, so that we can properly resolve the details. The grid density is set by the gradient of the scalar field, $|d\varphi/dr|$. At the start of the simulation, the grid is uniform with the number of grid points $\mathcal{O}(100)$. As the gradients sharpen, the number of grid points grows to $\mathcal{O}(10^3) - \mathcal{O}(10^4)$. Finite difference first and second derivatives are calculated using the stencils developed in [96]. First derivatives have error $\propto \Delta r^4$ and second derivatives have error $\propto \Delta r^3$. Due to the large gradients, we enforce a stringent Courant-Friedrichs-Lewy (CFL) condition [179] of $c\Delta N \sim 0.01\Delta r$. Our coordinate system requires a time step smaller by an order of magnitude compared to the previous work.

4.5 Simulation Results

4.5.1 Bubble Walls and Metric Functions

Unless stated otherwise, we use the parameters for V1 in Table 4.2 for the following results. We also include some results for three other simulation runs with increasing instanton radius (V2, V3, V4). In Fig. 4.9 we show the scalar field in (N, r). The true vacuum is red, the false vacuum is black, and the transition region is white. Initially, the wall moves toward smaller r, much like the constant X_4 seen in the naive coordinates of Fig. 4.5. After the initial decrease in radius, the wall moves back toward

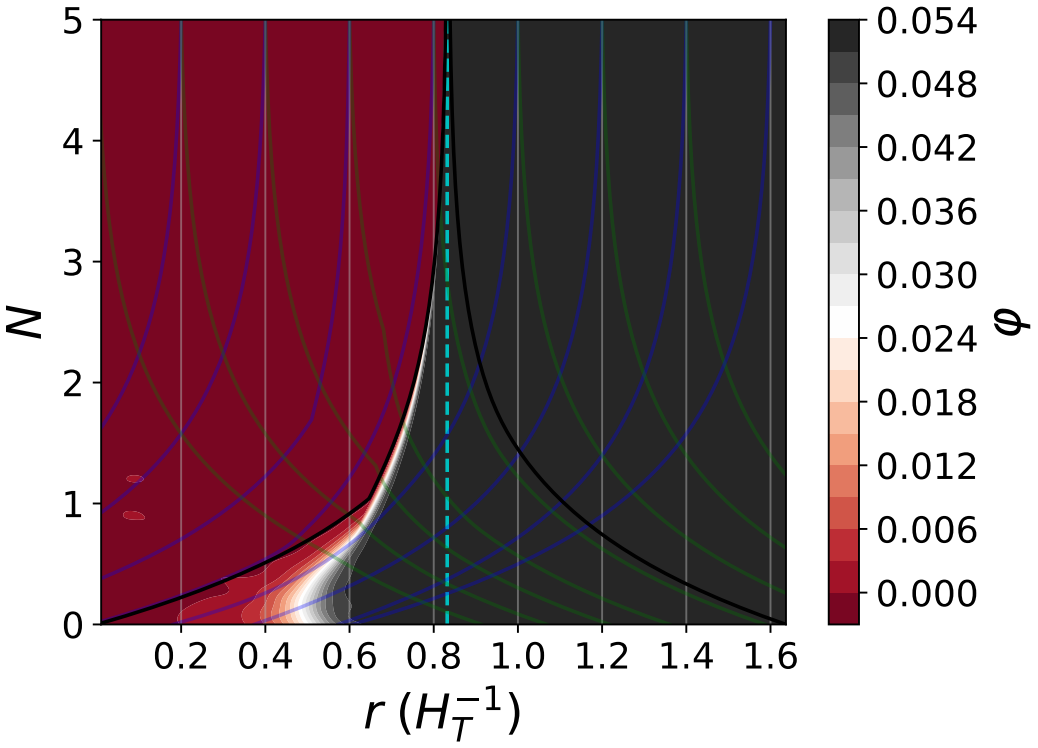

Figure 4.9: Instanton field in r and N. Ingoing and outgoing null paths are in green and blue, respectively. Boundary nulls are drawn in black analogous to Fig. 4.5. This result is for V1 of Table 4.2.

larger radius and thins due to length-contraction in co-moving coordinates. From previous simulations and junction conditions, we expect our bubble wall to asymptote to the false vacuum radius, $r \to H_F^{-1}/H_T^{-1}$ [6, 26, 155, 269], which we draw in dashed cyan.

Next, we plot the metric functions a and α in Fig. 4.10. a is initially constant equal to 1, but quickly starts to form a sharp peak at the location of the transition region in φ. As mentioned previously (Sec. 4.4.2), $\dot{a}$ contains terms that are additive, which causes the sharp spikes to remain long after they form. The initial peak follows the transition region of φ over time and eventually asymptotes to two roughly vertical lines, with the right line at the bubble wall location and the left line at $\sim H_T^{-1} - H_F^{-1}$ smaller radius. The initial plateau region seen in blue at $N = 0.71$ remains at late times because of the additive $\dot{a}$ equation. At small and large radii a retains the FLRW limits of $a \to 1$. Fig. 4.10 tells us that the bubble wall has an outsized effect on the spacetime compared to its thickness, as seen in Fig. 4.9. This has important consequences for forcing boundary null paths to asymptote to H_F^{-1} as we will see below.

α has the same initial peak structure as a, but as mentioned before, $\dot{\alpha}$ has terms that cancel each other out, causing the peak to decay after the transient terms die out. α approaches a step function with limits $\alpha \to 1$ for true vacuum and $\alpha \to H_F^{-1}/H_T^{-1}$ for false vacuum. Note that all of $\{\varphi, a, \alpha\}$ evolve more and more slowly as time elapses for $N > 1$. This is the effect of co-moving coordinates where the temporal derivatives tend to zero.

We calculated the ingoing (green) and outgoing (blue) null paths for 0.2 (H_T^{-1}) intervals (defined at $N = 5$) and overlayed them on Fig. 4.9. In pure de Sitter space, we

would predict an outgoing null path that begins at $r = 0$ to reach H^{-1} (for our setup, this would be H_T^{-1}). In the case of the bubble spacetime, the $r = 0$ boundary null reaches $r = H_F^{-1}/H_T^{-1}$ (left black line). The ingoing boundary null (right black line) starting at the right edge of our boundary, $X_4 = -H_F^{-1}$, also reaches $r = H_F^{-1}/H_T^{-1}$. These two nulls are analogous to the thick black lines in Fig. 4.5 that bound the wall region. Solving for these nulls and seeing that they asymptote to the same position as the bubble wall, H_F^{-1}, gives credence to the predictions mentioned previously and to the numerical simulation. The functions a and α define these null paths, so the fact that they follow the expected behavior should be further confirmation that we obtained the correct forms for our metric functions in the simulation.

	V1	V2	V3	V4
H_F^{-1}/H_T^{-1}	0.832	0.867	0.948	0.977
r_0 (H_T^{-1})	0.501	0.674	1.107	1.248
r_f (H_T^{-1})	0.824	0.860	0.945	0.978

Table 4.1: Simulation results for four samples, see Table 4.2. r_0 (H_T^{-1}) is the initial bubble radius for each sample in coordinates of Eq. 4.16. r_f (H_T^{-1}) is the final bubble radius.

Next, we show the radius of curvature for our four simulations in the top plot of Fig. 4.11. As expected of flat coordinates, our bubble walls grow in size like e^N, as can be seen by the linear curves on a logarithmic scale. Looking at the red curve, V1, and comparing it to the path of the wall in Fig. 4.9, the initial decrease of the wall in co-moving coordinates is compensated for by the exponential, e^N, and we get monotonic

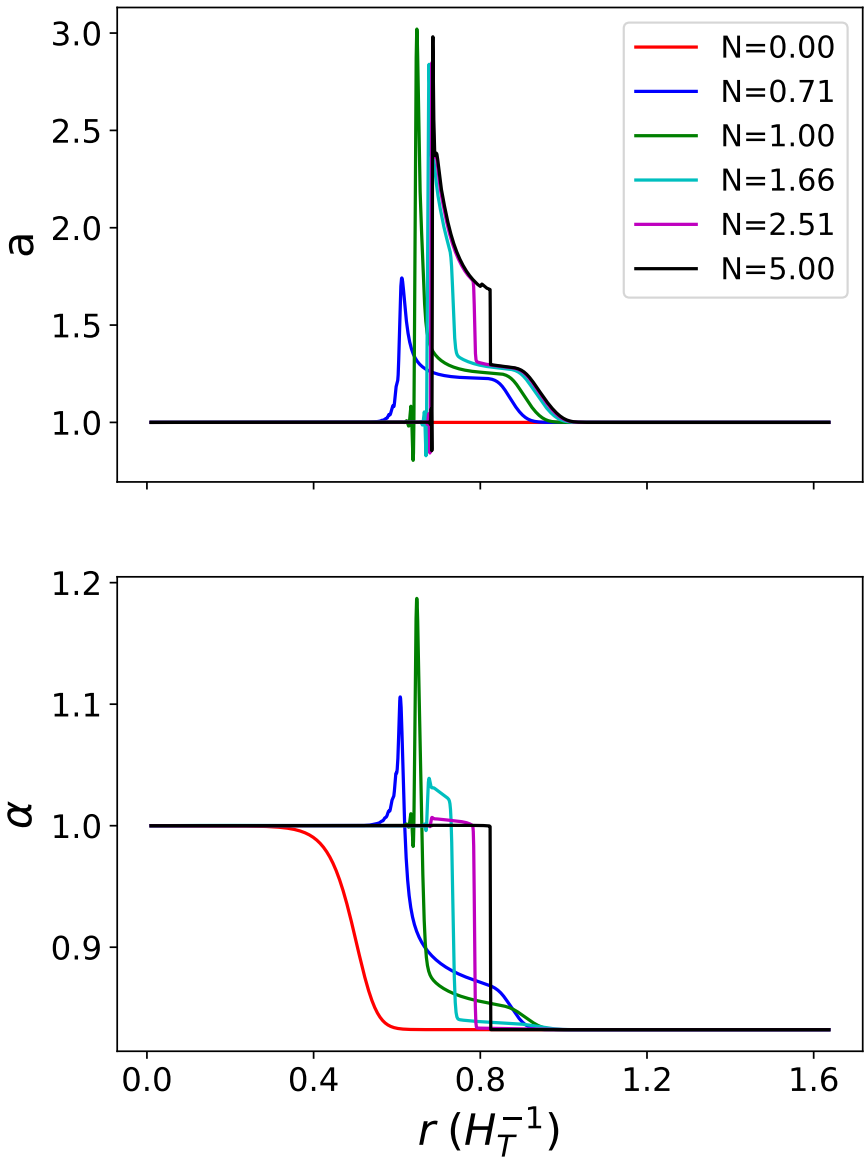

Figure 4.10: a and α in r and N. This result is for V1 of Table 4.2.

growth of the physical size of the bubble.[6]

In the bottom panel of Fig. 4.11, we plot the ending positions of our four simulated bubble walls (r_f) vs. their de Sitter radius ratios (H_F^{-1}/H_T^{-1}). We also tabulate these results in Table 4.1. We see a difference between predicted and simulated that is less than 1%.

4.5.2 Constraint Violation

If we satisfy the constraint equations on the initial slice, we are guaranteed to satisfy them at later times by the Bianchi Identity [28, 175]. We will use this to estimate the accuracy of the simulation by observing the momentum constraint violation over time.

The momentum constraint equation in this coordinate system with $b = 1$ is

$$C_P(N, r) \equiv \alpha \dot{a} - 4\pi r \alpha^2 \, \Pi \, \Phi + r a \alpha' = 0, \tag{4.26}$$

where we ignore the derivatives of the constant scalar field, χ.

Due to the length contraction of the bubble wall, spatial derivatives become divergent quickly (see Fig. 4.10). To account for this, we scale the momentum constraint violation, Eq. 4.26, by $1/\max(a'(N))$ on each time slice. This gives us a relevant physical scale to compare our violation to, as the constraint equation is dominated by spatial

[6] For smaller bubbles, the initial contraction can overcome the exponential factor to cause the physical size of the bubble to initially decrease before exponential growth.

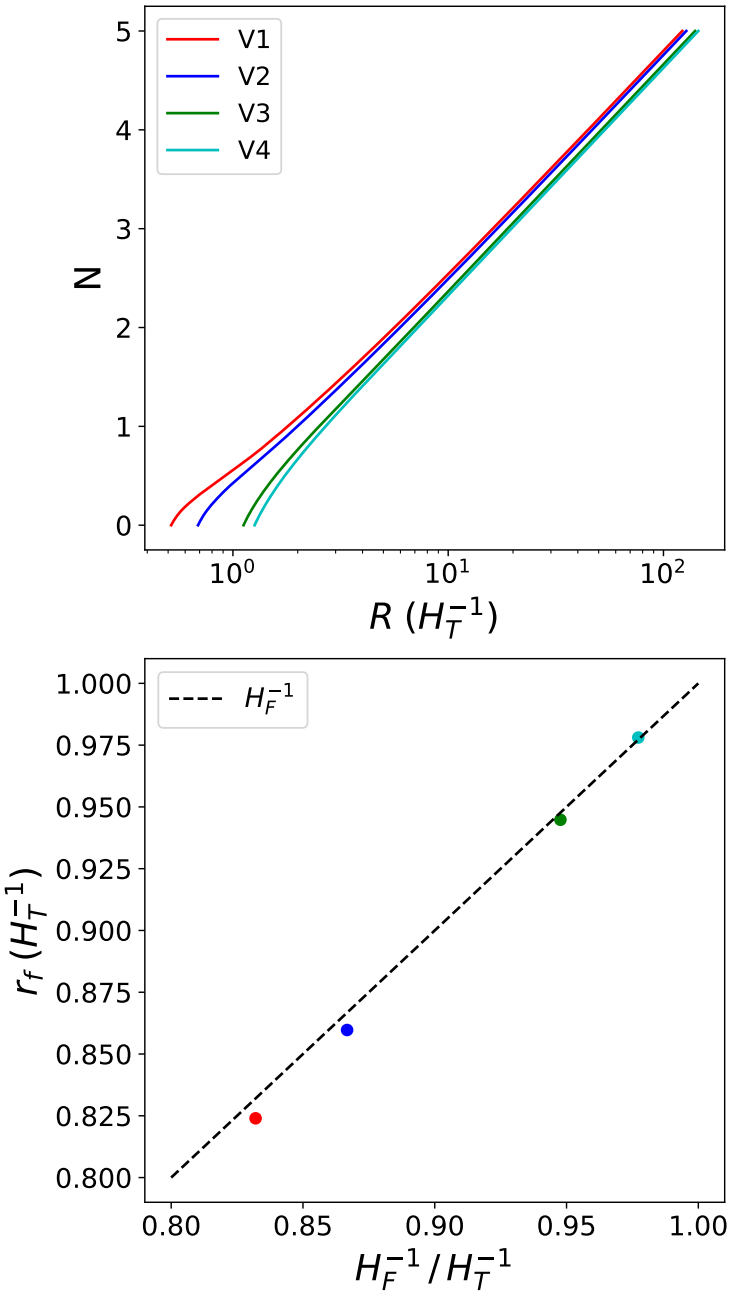

Figure 4.11: The top plot shows the radius of curvature for the four potential choices of Table 4.2. The bottom plot shows the final positions of the walls for the four samples. Additionally, we plot the predicted line of $r_f = H_F^{-1}\,/\,H_T^{-1}$.

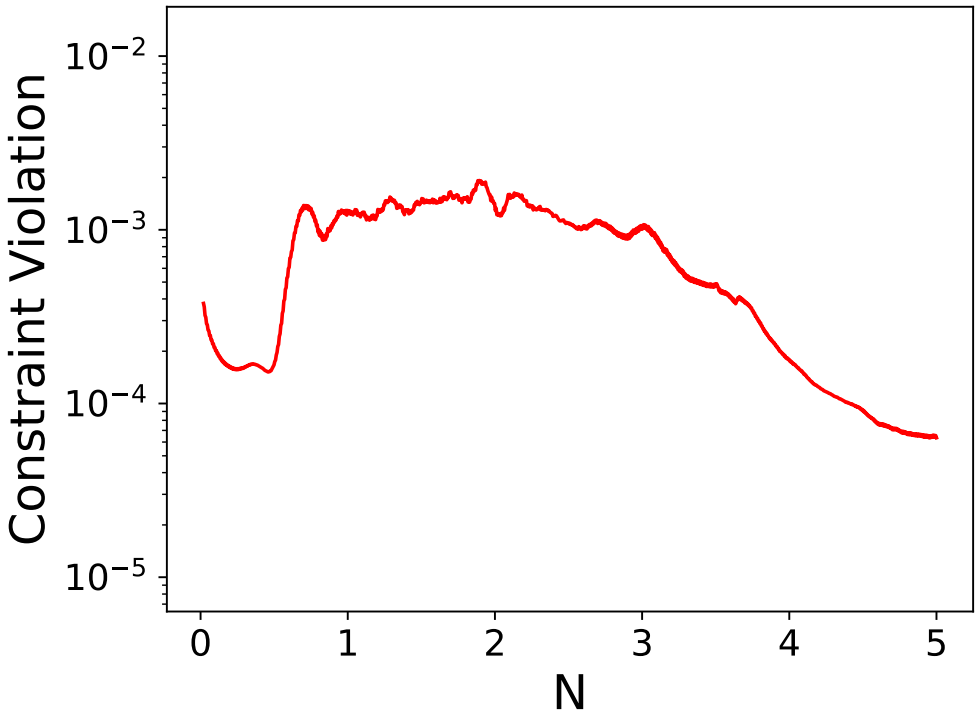

Figure 4.12: L^2 norm of rescaled momentum constraint, Eq. 4.26. This result is for V1 of Table 4.2.

derivatives. We take the L^2 norm of the rescaled momentum constraint over the spatial extent and plot as a function of N in Fig. 4.12.

We see that there is an initial rise in violation caused by the transient $1/r$ and $1/r^2$ terms seen in Eqs. 4.19 - 4.23. These terms have a large effect early, causing the spikes seen in Fig. 4.10 at $N < 1$. As time increases, the importance of these terms falls off like e^{-2N}, and we see that reflected in the leveling off and eventual decrease in violation.

If we wanted to decrease the overall violation of the simulation, we could make a few alterations to our methods. The first is to calculate more orders in the Taylor Expansion of the initial state and begin the simulation at a time earlier than $N = 10^{-6}$. The second and more effective method would be to more accurately calculate the initial state functions $\{\varphi_1, \alpha_0\}$, as these are the overwhelming source of the *initial* violation. Finally, different numerical methods beyond the method of lines and AMR could be used to better constrain the initial sharp increase in violation and spikes in the metric functions.

4.5.3 Convergence

We check the simulation convergence by calculating the self-convergence factor [49, 155, 177, 269]

$$2^q = \frac{||\varphi_p - \varphi_{2p}||_2}{||\varphi_{2p} - \varphi_{4p}||_2}. \tag{4.27}$$

We expect order $q \sim 3$ because finite difference second derivatives in this setup

have an error of Δr^3 in Runge-Kutta integration [155, 269].

The subscript p represents the grid spacing in Eq. 4.27, and to calculate the self convergence we ran three simulations of V1 with doubling grid density, $[p, 2p, 4p]$, and plotted in Fig. 4.13.

The result is convergence between 2nd and 3rd order after the initial transients of $N \lesssim 1$ die away. For this particular coordinate choice, we get large gradients in our metric functions and scalar field. These large gradients require more mesh density, resulting in a non-uniform mesh that becomes more non-uniform as time elapses. In [269], they noted that a uniform mesh results in a higher convergence order, and we are seeing the opposite effect here. This non-uniformity of the mesh due to large gradients accounts for the lower-than-expected convergence. Much like in the constraint violation, improvements to the numerical methods that better suit this coordinate system would likely improve convergence.

4.6 Discussion

In this article, we started with the Euclidean instanton, then we wrote a patchwork of coordinates to describe the space-time of the Lorentzian instanton. We defined a new flat(ish) coordinate system and solved for the transformation between these coordinates. Next, we solved for the initial state satisfying the Einstein equations and scalar equations of motion. Finally, we numerically simulated the system in full general relativity. The result was a better than 1% agreement with the prediction that bubbles

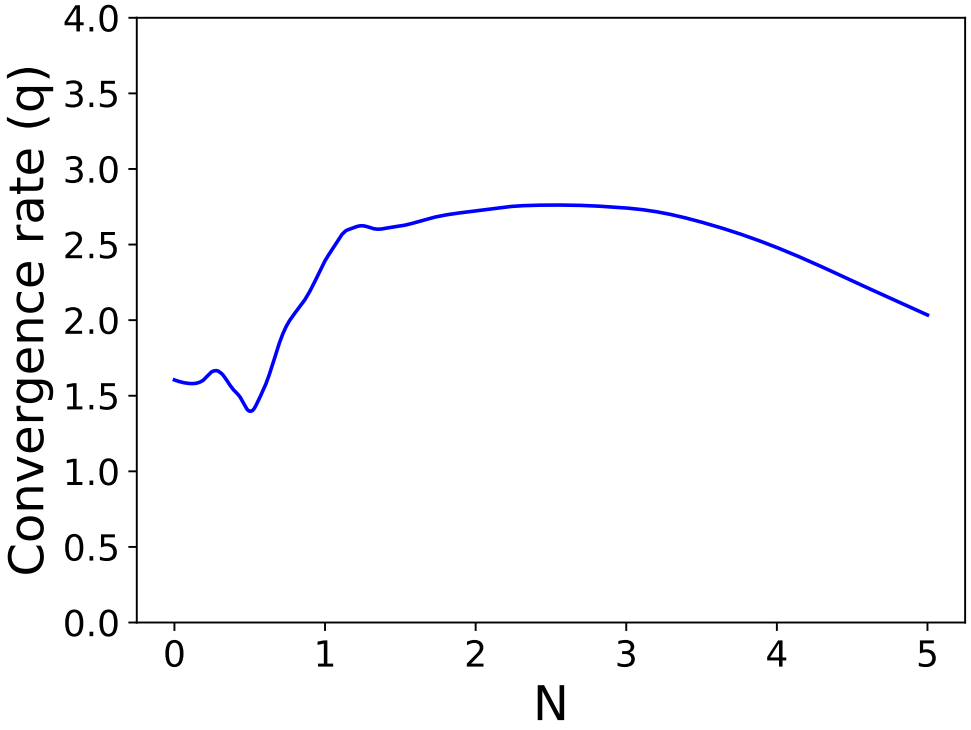

Figure 4.13: Convergence rate of scalar field. This result is for V1 of Table 4.2. After initial transient behavior, the simulation converges to between 2nd and 3rd order.

approach the false vacuum de Sitter radius (H_F^{-1}). We have validated our simulation for a single scalar field, which opens the door for simulating multi-field potentials to get more interesting behavior and possibly form black holes or wormholes. Additionally, we would like to simulate smaller radius instantons, especially those that do not reach the true minimum initially (more discussion can be found in App. 4.A). Simulating this expanded class of instantons would inform us of how a generic instanton evolves in general relativity.

4.A Potential Variables

	V1	V2	V3	V4
$m/M_{\rm Pl}$	10^{-4}	10^{-4}	10^{-4}	10^{-4}
c	1.04×10^{-3}	10^{-3}	0.94×10^{-3}	0.94×10^{-3}
a	6.1×10^{-6}	6.1×10^{-6}	6.1×10^{-6}	6.15×10^{-6}
g	10^{-11}	10^{-11}	10^{-11}	10^{-11}
j	10^{-10}	10^{-10}	10^{-10}	10^{-10}
h	$8. \times 10^{-12}$	$8. \times 10^{-12}$	$8. \times 10^{-12}$	$8. \times 10^{-12}$
$\chi/M_{\rm Pl}$	10^{-3}	10^{-3}	10^{-3}	10^{-3}

Table 4.2: Simulation variable choices for four samples, see Eq. 4.2.

We run four samples (V1 - V4), each with increasing H_F^{-1}, but the same H_T^{-1}. The ratio of Hubble radii can be seen in the first row of Table 4.1. For this particular potential, Eq. 4.2, the instanton radius increases as the true and false vacua become more degenerate.

At a certain point, as the false vacuum is raised away from the true vacuum, the instanton does not travel all the way to the true minimum ($\varphi(r = 0) > 0.0$). For

this work, we chose four instantons that reach vacuum to vacuum to avoid the issue of choosing the initial de Sitter radii for matching hyperboloids. For the case where the instanton does not reach the true vacuum initially, it is unclear if we can accurately picture the spacetime as two hyperboloids like in Figs. 4.3, 4.4. Assuming the initial instanton defines the energy density of the hyperboloids, we simulated such an example and saw that during the simulation, the scalar field rolled into the true vacuum over time, as expected. This question deserves more attention in future work.

4.B Return to Embedding

After determining the initial state in Sec. 4.4.3 we can match our metric components with those predicted by Eq. 4.12 to determine the functions $g_0(t,r),\ g_4(t,r)$. We will start by comparing $g_0(0,r)$ to the naive prediction of $\frac{r^2}{2}$ from Eq. 4.11. This will give us an idea of how accurate the naive picture (Fig. 4.5) is for $t = 0$. We do this for our four samples in Table 4.2.

As we can see in Fig. 4.14, the difference between naive prediction and generalized result improves as bubble size increases (from V1 to V4). This is in line with the claims made in Sec. 4.3.3.2. Notice that no matter the bubble size we start to diverge from the naive result at large r. This is no surprise because we are no longer in a pure, true vacuum regime as r increases, and thus Eq. 4.11 is inadequate for describing the spacetime.

As $N \to \infty$, we can solve the generalized embedding equations using our

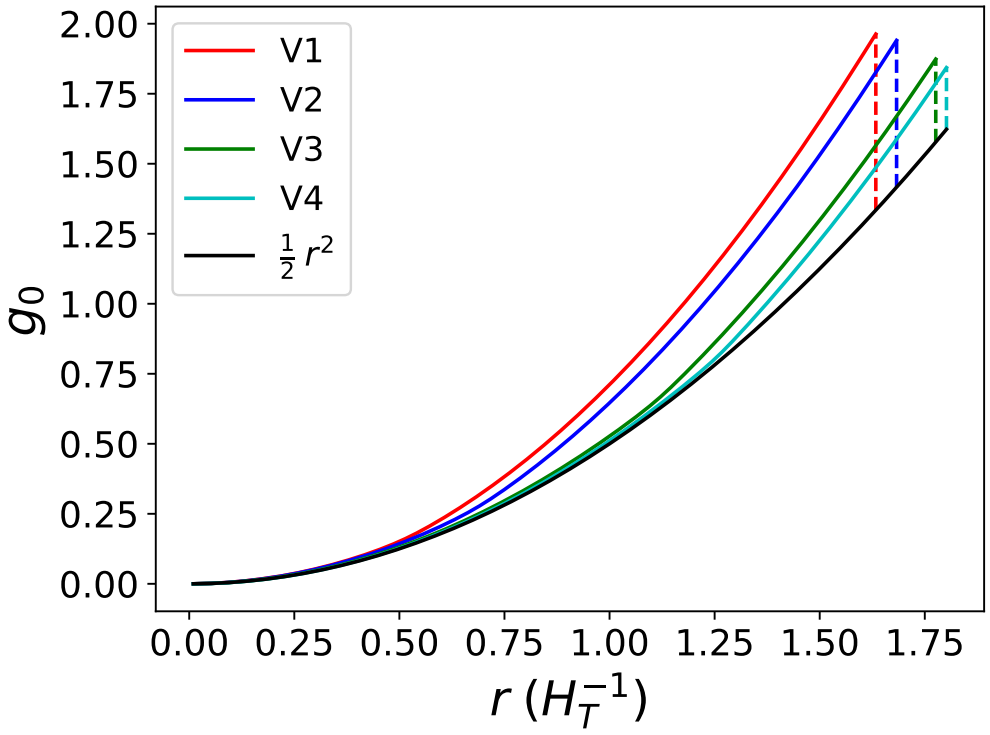

Figure 4.14: Initial state g_0 (Eq. 4.12) for the samples of Table 4.2 compared to the naive embedding result $\frac{1}{2}r^2$, Eq. 4.11. Dashed lines illustrate the disparity between the generalized and naive results. Smaller bubbles are more different from the naive result than larger bubbles and thus we see a decreasing discrepancy as we move from V1 to V4.

simulated metric functions a and α. Using Eq. 4.13 and the equivalent α equation with the simplification that as $N \to \infty$ we find $\dot{g_0}\ \dot{g_4} \to 0$, we are able to solve for X_4 at $N = 5$. As mentioned in [6], Israel Junction conditions predict a CDL bubble will follow a constant X_4 (r_E) trajectory. We are able to estimate the X_4 value of the bubble wall at $N = 5$, and we overestimate the prediction given by $N = 0$ calculation by $\sim 10\%$. This overestimate is caused in part by $r_f \lesssim H_F^{-1}$ (H_T^{-1}) as seen in Table 4.1. While this may at first seem large compared to better than 1% of matching r_f to H_F^{-1}, consider that $X_4^{\text{wall}} = 0.849$ (H_T^{-1}) and $X_4(N = 5)$ varies from 74 (H_T^{-1}) to -150 (H_T^{-1}). Given the large range of $X_4(N = 5)$, 10% difference from prediction seems more reasonable than at first glance.

Chapter 5

Conclusion

In this thesis, we looked at three research avenues related to black hole and bubble physics. In the first project, we outlined a novel search for Primordial Black Holes using microlensing simulations of the Nancy Grace Roman Space Telescope. In the second project, we analyzed the black hole information problem in the context of an explicitly defined evaporation diagram. In the final project, we developed a coordinate system for bubble nucleation and evolution and numerically simulated the system in full general relativity.

Bibliography

[1] Adaptive mesh refinement for hyperbolic partial differential equations. Journal of Computational Physics, 53(3):484–512, 1984.

[2] Debiasing the neowise cryogenic mission comet populations. The Astronomical Journal, 154(2):53, jul 2017.

[3] F. Abe et al. MOA II Gravitational Microlensing Survey — A new generation microlensing survey —. In 17th Workshop on General Relativity and Gravitation in Japan, pages 62–74, 2008.

[4] Fred C. Adams, Katherine Freese, and Lawrence M. Widrow. Evolution of Nonspherical Bubbles. Phys. Rev. D, 41:347, 1990.

[5] Anthony Aguirre and Matthew C. Johnson. Dynamics and instability of false vacuum bubbles. Phys. Rev. D, 72:103525, 2005.

[6] Anthony Aguirre and Matthew C Johnson. Towards observable signatures of other

bubble universes. II: Exact solutions for thin-wall bubble collisions. Phys. Rev. D, 77:123536, 2008.

[7] Anthony Aguirre and Matthew C Johnson. A status report on the observability of cosmic bubble collisions. Reports on Progress in Physics, 74(7):074901, jun 2011.

[8] Anthony Aguirre, Matthew C Johnson, and Assaf Shomer. Towards observable signatures of other bubble universes. Phys. Rev. D, 76:063509, 2007.

[9] Chris Akers, Netta Engelhardt, and Daniel Harlow. Simple holographic models of black hole evaporation. JHEP, 08:032, 2020.

[10] C. Alcock et al. The MACHO project: Microlensing results from 5.7 years of LMC observations. Astrophys. J., 542:281–307, 2000.

[11] C. Alcock et al. The MACHO project: microlensing detection efficiency. Astrophys. J. Suppl., 136:439–462, 2001.

[12] Ahmed Almheiri, Netta Engelhardt, Donald Marolf, and Henry Maxfield. The entropy of bulk quantum fields and the entanglement wedge of an evaporating black hole. JHEP, 12:063, 2019.

[13] Ahmed Almheiri, Thomas Hartman, Juan Maldacena, Edgar Shaghoulian, and Amirhossein Tajdini. The entropy of Hawking radiation. 6 2020.

[14] Ahmed Almheiri, Raghu Mahajan, Juan Maldacena, and Ying Zhao. The Page curve of Hawking radiation from semiclassical geometry. JHEP, 03:149, 2020.

[15] Ahmed Almheiri, Donald Marolf, Joseph Polchinski, and James Sully. Black Holes: Complementarity or Firewalls? JHEP, 02:062, 2013.

[16] Lautaro Amadei, Hongguang Liu, and Alejandro Perez. Unitarity and information in quantum gravity: a simple example. 12 2019.

[17] Lautaro Amadei and Alejandro Perez. Hawking's information puzzle: a solution realized in loop quantum cosmology. 11 2019.

[18] A. Ashtekar and A. Magnon. Quantum Fields in Curved Space-Times. Proc. Roy. Soc. Lond. A, 346:375–394, 1975.

[19] Abhay Ashtekar. Black Hole evaporation: A Perspective from Loop Quantum Gravity. Universe, 6(2):21, 2020.

[20] E. Bachelet, D. Specht, M. Penny, M. Hundertmark, S. Awiphan, J.-P. Beaulieu, M. Dominik, E. Kerins, D. Maoz, E. Meade, A. A. Nucita, R. Poleski, C. Ranc, J. Rhodes, and A. C. Robin. Euclid-roman joint microlensing survey: Early mass measurement, free floating planets, and exomoons. Astronomy and Astrophysics, 664:A136, aug 2022.

[21] Guillermo Ballesteros and Marco Taoso. Primordial black hole dark matter from single field inflation. Phys. Rev. D, 97(2):023501, 2018.

[22] T. Banks. Heretics of the false vacuum: Gravitational effects on and of vacuum decay. 2. 11 2002.

[23] James M. Bardeen. Black hole evaporation without an event horizon. 6 2014.

[24] James M. Bardeen. Interpreting the semi-classical stress-energy tensor in a Schwarzschild background, implications for the information paradox. 8 2018.

[25] C. Barrabes and W. Israel. Thin shells in general relativity and cosmology: The Lightlike limit. Phys. Rev. D, 43:1129–1142, 1991.

[26] C. Barrabès and W. Israel. Thin shells in general relativity and cosmology: The lightlike limit. Physical Review D, 43(4):1129–1142, Feb 1991.

[27] Virginie Batista, A. Gould, S. Dieters, Subo Dong, I. Bond, J. P. Beaulieu, D. Maoz, B. Monard, G. W. Christie, J. McCormick, M. D. Albrow, K. Horne, Y. Tsapras, M. J. Burgdorf, S. Calchi Novati, J. Skottfelt, J. Caldwell, S. Kozlowski, D. Kubas, B. S. Gaudi, C. Han, D. P. Bennett, J. An, the MOA Collaboration, the PLANET Collaboration, the MicroFUN Collaboration, the MiNDSTEp Consortium, and the RoboNet Collaboration. MOA-2009-BLG-387Lb: A massive planet orbiting an M dwarf. Astronomy & Astrophysics, 529:A102, May 2011. arXiv:1102.0558 [astro-ph].

[28] T.W. Baumgarte and S.L. Shapiro. Numerical Relativity: Solving Einstein's Equations on the Computer. Cambridge University Press, 2010.

[29] Jacob D. Bekenstein. A Universal Upper Bound on the Entropy to Energy Ratio for Bounded Systems. Phys. Rev. D, 23:287, 1981.

[30] Jacob D. Bekenstein. How fast does information leak out from a black hole? Phys. Rev. Lett., 70:3680–3683, 1993.

[31] Nicola Bellomo, José Luis Bernal, Alvise Raccanelli, and Licia Verde. Primordial Black Holes as Dark Matter: Converting Constraints from Monochromatic to Extended Mass Distributions. Journal of Cosmology and Astroparticle Physics, 2018(01):004–004, January 2018. arXiv:1709.07467 [astro-ph].

[32] Saloni Bhatiani, Xinyu Dai, and Eduardo Guerras. Confirmation of Planet-mass Objects in Extragalactic Systems. apj, 885(1):77, November 2019.

[33] Saloni Bhatiani, Xinyu Dai, and Eduardo Guerras. Confirmation of planet-mass objects in extragalactic systems. The Astrophysical Journal, 885(1):77, nov 2019.

[34] Eugenio Bianchi and Matteo Smerlak. Entanglement entropy and negative energy in two dimensions. Phys. Rev. D, 90(4):041904, 2014.

[35] N.D. Birrell and P.C.W. Davies. Quantum Fields in Curved Space. Cambridge Monographs on Mathematical Physics. Cambridge Univ. Press, Cambridge, UK, 2 1984.

[36] N.D. Birrell and J.G. Taylor. Analysis of Interacting Quantum Field Theory in Curved Space-time. J. Math. Phys., 21:1740–1760, 1980.

[37] Jose J. Blanco-Pillado, Martin Bucher, Sima Ghassemi, and Frederic Glanois. When do colliding bubbles produce an expanding universe? Phys. Rev. D, 69:103515, 2004.

[38] Joss Bland-Hawthorn and Ortwin Gerhard. The galaxy in context: Struc-

tural, kinematic, and integrated properties. Annual Review of Astronomy and Astrophysics, 54(1):529–596, 2016.

[39] Steven K. Blau, E. I. Guendelman, and Alan H. Guth. Dynamics of false-vacuum bubbles. Physical Review D, 35(6):1747–1766, Mar 1987.

[40] G. V. Borisov and B. M. Shustov. Discovery of the First Interstellar Comet and the Spatial Density of Interstellar Objects in the Solar Neighborhood. Solar System Research, 55(2):124–131, March 2021.

[41] Raphael Bousso. A Covariant entropy conjecture. JHEP, 07:004, 1999.

[42] Raphael Bousso and Marija Tomašević. Unitarity From a Smooth Horizon? 11 2019.

[43] Jo Bovy. Stellar Inventory of the Solar Neighborhood using Gaia DR1. Monthly Notices of the Royal Astronomical Society, 470(2):1360–1387, September 2017. arXiv:1704.05063 [astro-ph].

[44] Jonathan Braden, Matthew C. Johnson, Hiranya V. Peiris, and Anthony Aguirre. Constraining cosmological ultralarge scale structure using numerical relativity. Phys. Rev. D, 96(2):023541, 2017.

[45] Peter G. Brown and Jiří Borovička. On the proposed interstellar origin of the usg 20140108 fireball, 2023.

[46] Ram Brustein. Origin of the blackhole information paradox. Fortsch. Phys., 62:255–265, 2014.

[47] Christian T. Byrnes, Mark Hindmarsh, Sam Young, and Michael R. S. Hawkins. Primordial black holes with an accurate QCD equation of state. JCAP, 08:041, 2018.

[48] Qing-yu Cai, Baocheng Zhang, Ming-sheng Zhan, and Li You. Comment on 'What the information loss is not'. 10 2012.

[49] Gioel Calabrese, Luis Lehner, Oscar Reula, Olivier Sarbach, and Manuel Tiglio. Summation by parts and dissipation for domains with excised regions. Classical and Quantum Gravity, 21(24):5735–5757, November 2004.

[50] Pasquale Calabrese and John L. Cardy. Entanglement entropy and quantum field theory. J. Stat. Mech., 0406:P06002, 2004.

[51] S. Calchi Novati, S. Mirzoyan, Ph. Jetzer, and G. Scarpetta. Microlensing towards the SMC: a new analysis of OGLE and EROS results. Mon. Not. Roy. Astron. Soc., 435:1582, 2013.

[52] Robert D. Carlitz and Raymond S. Willey. REFLECTIONS ON MOVING MIRRORS. Phys. Rev. D, 36:2327–2335, 1987.

[53] Robert D. Carlitz and Raymond S. Willey. The Lifetime of a Black Hole. Phys. Rev. D, 36:2336, 1987.

[54] Christopher D. Carone and Alan H. Guth. THE DYNAMICS OF THICK DOMAIN WALLS IN AN INHOMOGENEOUS INFLATIONARY MODEL. Phys. Rev. D, 42:2446–2457, 1990.

[55] Bernard Carr, Kazunori Kohri, Yuuiti Sendouda, and Jun'ichi Yokoyama. Constraints on primordial black holes. Rept. Prog. Phys., 84(11):116902, 2021.

[56] Bernard Carr and Florian Kuhnel. Primordial black holes as dark matter candidates. SciPost Phys. Lect. Notes, 48:1, 2022.

[57] Bernard Carr and Florian Kühnel. Primordial black holes as dark matter candidates. SciPost Physics Lecture Notes, may 2022.

[58] Bernard J. Carr and S. W. Hawking. Black holes in the early Universe. Mon. Not. Roy. Astron. Soc., 168:399–415, 1974.

[59] Bernard J. Carr and James E. Lidsey. Primordial black holes and generalized constraints on chaotic inflation. Phys. Rev. D, 48:543–553, 1993.

[60] H. Casini. Relative entropy and the Bekenstein bound. Class. Quant. Grav., 25:205021, 2008.

[61] Sumanta Chakraborty and Kinjalk Lochan. Black Holes: Eliminating Information or Illuminating New Physics? Universe, 3(3):55, 2017.

[62] Hong Zhe Chen, Zachary Fisher, Juan Hernandez, Robert C. Myers, and Shan-Ming Ruan. Information Flow in Black Hole Evaporation. JHEP, 03:152, 2020.

[63] Pisin Chen, Misao Sasaki, and Dong-han Yeom. A path(-integral) toward non-perturbative effects in Hawking radiation. 5 2020.

[64] Matthew W. Choptuik. Universality and scaling in gravitational collapse of a massless scalar field. Phys. Rev. Lett., 70:9–12, 1993.

[65] Sidney Coleman and Frank De Luccia. Gravitational effects on and of vacuum decay. Phys. Rev. D, 21:3305–3315, Jun 1980.

[66] Sidney R. Coleman. The Fate of the False Vacuum. 1. Semiclassical Theory. Phys. Rev. D, 15:2929–2936, 1977. [Erratum: Phys.Rev.D 16, 1248 (1977)].

[67] Eric Cotner and Alexander Kusenko. Primordial black holes from scalar field evolution in the early universe. Phys. Rev. D, 96(10):103002, 2017.

[68] Eric Cotner and Alexander Kusenko. Primordial black holes from supersymmetry in the early universe. Phys. Rev. Lett., 119(3):031103, 2017.

[69] Eric Cotner, Alexander Kusenko, Misao Sasaki, and Volodymyr Takhistov. Analytic Description of Primordial Black Hole Formation from Scalar Field Fragmentation. JCAP, 10:077, 2019.

[70] Eric Cotner, Alexander Kusenko, and Volodymyr Takhistov. Primordial Black Holes from Inflaton Fragmentation into Oscillons. Phys. Rev. D, 98(8):083513, 2018.

[71] Matt Crawford and David N. Schramm. Spontaneous Generation of Density Perturbations in the Early Universe. Nature, 298:538–540, 1982.

[72] Djuna Croon, David McKeen, Nirmal Raj, and Zihui Wang. Subaru through a

different lens: microlensing by extended dark matter structures. Physical Review D, 102(8):083021, October 2020. arXiv:2007.12697 [astro-ph, physics:hep-ph].

[73] Xinyu Dai and Eduardo Guerras. Probing extragalactic planets using quasar microlensing. The Astrophysical Journal, 853(2):L27, feb 2018.

[74] P.C.W. Davies, S.A. Fulling, and W.G. Unruh. Energy Momentum Tensor Near an Evaporating Black Hole. Phys. Rev. D, 13:2720–2723, 1976.

[75] Heling Deng. Primordial black hole formation by vacuum bubbles. Part II. JCAP, 09:023, 2020.

[76] Heling Deng, Jaume Garriga, and Alexander Vilenkin. Primordial black hole and wormhole formation by domain walls. Journal of Cosmology and Astroparticle Physics, 2017(04):050–050, Apr 2017.

[77] Heling Deng and Alexander Vilenkin. Primordial black hole formation by vacuum bubbles. JCAP, 12:044, 2017.

[78] W. DeRocco, M. Kunimoto, and N. Smyth. ——, 2023.

[79] William DeRocco and Peter W. Graham. Constraining Primordial Black Hole Abundance with the Galactic 511 keV Line. Phys. Rev. Lett., 123(25):251102, 2019.

[80] William DeRocco, Nolan Smyth, and Stefano Profumo. Constraints on sub-terrestrial free-floating planets from Subaru microlensing observations, August 2023. arXiv:2308.13593 [astro-ph, physics:hep-ph].

[81] Bryce S. DeWitt. Quantum Field Theory in Curved Space-Time. Phys. Rept., 19:295–357, 1975.

[82] Aaron Do, Michael A. Tucker, and John Tonry. Interstellar interlopers: Number density and origin of 'oumuamua-like objects. The Astrophysical Journal, 855(1):L10, mar 2018.

[83] J. S. Dohnanyi. Collisional Model of Asteroids and Their Debris. In Lubor Kresak and Peter Mackenzie Millman, editors, Physics and Dynamics of Meteors, volume 33, page 486, January 1968.

[84] Alexandre Dolgov and Joseph Silk. Baryon isocurvature fluctuations at small scales and baryonic dark matter. Phys. Rev. D, 47:4244–4255, 1993.

[85] Xi Dong, Daniel Harlow, and Aron C. Wall. Reconstruction of Bulk Operators within the Entanglement Wedge in Gauge-Gravity Duality. Phys. Rev. Lett., 117(2):021601, 2016.

[86] Tevian Dray and Gerard 't Hooft. The Effect of Spherical Shells of Matter on the Schwarzschild Black Hole. Commun. Math. Phys., 99:613–625, 1985.

[87] Netta Engelhardt and Aron C. Wall. Quantum Extremal Surfaces: Holographic Entanglement Entropy beyond the Classical Regime. JHEP, 01:073, 2015.

[88] Toni Engelhardt, Robert Jedicke, Peter Vereš , Alan Fitzsimmons, Larry Denneau, Ed Beshore, and Bonnie Meinke. An observational upper limit on the interstellar

number density of asteroids and comets. The Astronomical Journal, 153(3):133, feb 2017.

[89] Sonja Engmann and Denis Cousineau. Comparing distributions: the two-sample anderson–darling test as an alternative to the kolmogorov–smirnov test. Journal of Applied Quantitative Methods, 6:1–17, 09 2011.

[90] Albert Escrivà, Vicente Atal, and Jaume Garriga. Formation of trapped vacuum bubbles during inflation, and consequences for PBH scenarios. JCAP, 10:035, 2023.

[91] Sergio B. Fajardo-Acosta, Andreas Faisst, Carl J. Grillmair, Ranga-Ram Chary, Roberta Paladini, Ben Rusholme, and Nathaniel Stickley. Joint Survey Processing. II. Stellar Proper Motions in the COSMOS Field from Hubble Space Telescope ACS and Subaru Telescope HSC Observations. The Astrophysical Journal, 930(1):71, May 2022. Publisher: The American Astronomical Society.

[92] Edward Farhi, Alan H. Guth, and Jemal Guven. Is it possible to create a universe in the laboratory by quantum tunneling? Nuclear Physics B, 339(2):417–490, Jul 1990.

[93] Y.R. Fernández, M.S. Kelley, P.L. Lamy, I. Toth, O. Groussin, C.M. Lisse, M.F. A'Hearn, J.M. Bauer, H. Campins, A. Fitzsimmons, J. Licandro, S.C. Lowry, K.J. Meech, J. Pittichová, W.T. Reach, C. Snodgrass, and H.A. Weaver. Thermal

properties, sizes, and size distribution of jupiter-family cometary nuclei. Icarus, 226(1):1138–1170, 2013.

[94] Alan Fitzsimmons, Karem Meech, Luca Matrà, and Susanne Pfalzner. Interstellar objects and exocomets, 2023.

[95] Eirik Grude Flekkøy and Renaud Toussaint. Statistical implications of the n = 1 observation of 1I/'Oumuamua. Monthly Notices of the Royal Astronomical Society: Letters, 523(1):L9–L14, 04 2023.

[96] Bengt Fornberg. Generation of finite difference formulas on arbitrarily spaced grids. Mathematics of Computation, 51(184):699–706, 1988.

[97] Ben Freivogel, Gary T. Horowitz, and Stephen Shenker. Colliding with a crunching bubble. JHEP, 05:090, 2007.

[98] Nava Gaddam and Nico Groenenboom. Soft graviton exchange and the information paradox. 12 2020.

[99] Nava Gaddam, Nico Groenenboom, and Gerard 't Hooft. Quantum gravity on the black hole horizon. 12 2020.

[100] Wen-Cong Gan and Fu-Wen Shu. Information loss paradox revisited: farewell firewall? 5 2020.

[101] Juan Garcia-Bellido and Ester Ruiz Morales. Primordial black holes from single field models of inflation. Phys. Dark Univ., 18:47–54, 2017.

[102] Jaume Garriga and Alexander Vilenkin. Perturbations on domain walls and strings: A Covariant theory. Phys. Rev. D, 44:1007–1014, 1991.

[103] Jaume Garriga and Alexander Vilenkin. Quantum fluctuations on domain walls, strings and vacuum bubbles. Phys. Rev. D, 45:3469–3486, 1992.

[104] Jaume Garriga and Alexander Vilenkin. Recycling universe. Phys. Rev. D, 57:2230–2244, Feb 1998.

[105] Jaume Garriga, Alexander Vilenkin, and Jun Zhang. Black holes and the multiverse. Journal of Cosmology and Astroparticle Physics, 2016(02):064, Feb 2016.

[106] Andrá s Gáspár, Dimitrios Psaltis, George H. Rieke, and Feryal Özel. MODELING COLLISIONAL CASCADES IN DEBRIS DISKS: STEEP DUST-SIZE DISTRIBUTIONS. The Astrophysical Journal, 754(1):74, jul 2012.

[107] B. Scott Gaudi. The Roman Galactic Bulge Time Domain Survey. In Bulletin of the American Astronomical Society, volume 54, page 102.146, June 2022.

[108] F. F. Gautason, Lukas Schneiderbauer, Watse Sybesma, and Lárus Thorlacius. Page Curve for an Evaporating Black Hole. JHEP, 05:091, 2020.

[109] Shuailiang Ge. Sublunar-Mass Primordial Black Holes from Closed Axion Domain Walls. Phys. Dark Univ., 27:100440, 2020.

[110] Cristiano Germani and Tomislav Prokopec. On primordial black holes from an inflection point. Phys. Dark Univ., 18:6–10, 2017.

[111] G.W. Gibbons. Quantum Field Theory In Curved Space-time, pages 639–679. 4 1978.

[112] Steven B. Giddings. Black hole information, unitarity, and nonlocality. Phys. Rev. D, 74:106005, 2006.

[113] Steven B. Giddings and Matthew Lippert. The Information paradox and the locality bound. Phys. Rev. D, 69:124019, 2004.

[114] Michael R. R. Good, Paul R. Anderson, and Charles R. Evans. Mirror Reflections of a Black Hole. Phys. Rev. D, 94(6):065010, 2016.

[115] Michael R.R. Good, Paul R. Anderson, and Charles R. Evans. Time Dependence of Particle Creation from Accelerating Mirrors. Phys. Rev. D, 88:025023, 2013.

[116] Michael R.R. Good, Eric V. Linder, and Frank Wilczek. Moving mirror model for quasithermal radiation fields. Phys. Rev. D, 101(2):025012, 2020.

[117] Andrew Gould, Youn Kil Jung, Kyu-Ha Hwang, Subo Dong, Michael D. Albrow, Sun-Ju Chung, Cheongho Han, Yoon-Hyun Ryu, In-Gu Shin, Yossi Shvartzvald, Hongjing Yang, Jennifer C. Yee, Weicheng Zang, Sang-Mok Cha, Dong-Jin Kim, Seung-Lee Kim, Chung-Uk Lee, Dong-Joo Lee, Yongseok Lee, Byeong-Gon Park, and Richard W. Pogge. Free-Floating Planets, the Einstein Desert, and 'Oumuamua. Journal of The Korean Astronomical Society, 55(5):173–194, October 2022. arXiv:2204.03269 [astro-ph].

[118] Andrew Gould, JungYoun Kil, HwangKyu-Ha, DongSubo, AlbrowMichael D.,

ChungSun-Ju, HanCheongho, RyuYoon-Hyun, ShinIn-Gu, ShvartzvaldYossi, YangHongjing, YeeJennifer C., ZangWeicheng, ChaSang-Mok, KimDong-Jin, KimSeung-Lee, LeeChung-Uk, LeeDong-Joo, LeeYongseok, ParkByeong-Gon, and PoggeRichard W. Free-floating planets, the einstein desert, and 'oumuamua. Journal of The Korean Astronomical Society, 55(5):173–194, 10 2022.

[119] Andrew Gould, Yoon-Hyun Ryu, Jennifer C. Yee, Michael D. Albrow, Sun-Ju Chung, Cheongho Han, Kyu-Ha Hwang, Youn Kil Jung, In-Gu Shin, Yossi Shvartzvald, Hongjing Yang, Weicheng Zang, Sang-Mok Cha, Dong-Jin Kim, Seung-Lee Kim, Chung-Uk Lee, Dong-Joo Lee, Yongseok Lee, Byeong-Gon Park, and Richard W. Pogge. KMT-2022-BLG-2397: Brown Dwarf at the Upper Shore of the Einstein Desert. arXiv e-prints, page arXiv:2306.04870, June 2023.

[120] Andrew Gould, Wei-Cheng Zang, Shude Mao, and Su-Bo Dong. Masses for free-floating planets and dwarf planets. Research in Astronomy and Astrophysics, 21(6):133, August 2021.

[121] Anne M. Green. Microlensing and dynamical constraints on primordial black hole dark matter with an extended mass function. Phys. Rev. D, 94(6):063530, 2016.

[122] Kim Griest, Agnieszka M. Cieplak, and Matthew J. Lehner. New Limits on Primordial Black Hole Dark Matter from an Analysis of Kepler Source Microlensing Data. Phys. Rev. Lett., 111(18):181302, 2013.

[123] Hal M. Haggard and Carlo Rovelli. Quantum-gravity effects outside the horizon spark black to white hole tunneling. Phys. Rev. D, 92(10):104020, 2015.

[124] P. Hajicek. What simplified models say about unitarity and gravitational collapse. Nucl. Phys. B Proc. Suppl., 88:114–123, 2000.

[125] Daniel Harlow. Jerusalem Lectures on Black Holes and Quantum Information. Rev. Mod. Phys., 88:015002, 2016.

[126] S. W. Hawking. Black hole explosions. Nature, 248:30–31, 1974.

[127] S. W. Hawking. Black Holes From Cosmic Strings. Phys. Lett. B, 231:237–239, 1989.

[128] S. W. Hawking, I. G. Moss, and J. M. Stewart. Bubble Collisions in the Very Early Universe. Phys. Rev. D, 26:2681, 1982.

[129] Stephen Hawking. Gravitationally collapsed objects of very low mass. Mon. Not. Roy. Astron. Soc., 152:75, 1971.

[130] Stephen W. Hawking, Malcolm J. Perry, and Andrew Strominger. Soft Hair on Black Holes. Phys. Rev. Lett., 116(23):231301, 2016.

[131] S.W. Hawking. Particle Creation by Black Holes. Commun. Math. Phys., 43:199–220, 1975. [Erratum: Commun.Math.Phys. 46, 206 (1976)].

[132] S.W. Hawking. Breakdown of Predictability in Gravitational Collapse. Phys. Rev. D, 14:2460–2473, 1976.

[133] S.W. Hawking. The Unpredictability of Quantum Gravity. Commun. Math. Phys., 87:395–415, 1982.

[134] S.W. Hawking. Information loss in black holes. Phys. Rev. D, 72:084013, 2005.

[135] Patrick Hayden and John Preskill. Black holes as mirrors: Quantum information in random subsystems. JHEP, 09:120, 2007.

[136] Sean A. Hayward. Formation and evaporation of regular black holes. Phys. Rev. Lett., 96:031103, 2006.

[137] Thomas Helfer, Josu C. Aurrekoetxea, and Eugene A. Lim. Cosmic String Loop Collapse in Full General Relativity. Phys. Rev. D, 99(10):104028, 2019.

[138] Mark P. Hertzberg and Masaki Yamada. Primordial Black Holes from Polynomial Potentials in Single Field Inflation. Phys. Rev. D, 97(8):083509, 2018.

[139] W.A. Hiscock. Models of Evaporating Black Holes. II. Effects of the Outgoing Created Radiation. Phys. Rev. D, 23:2823–2827, 1981.

[140] Christoph Holzhey, Finn Larsen, and Frank Wilczek. Geometric and renormalized entropy in conformal field theory. Nucl. Phys. B, 424:443–467, 1994.

[141] Devin J. Hoover, Darryl Z. Seligman, and Matthew J. Payne. The population of interstellar objects detectable with the lsst and accessible for *In Situ* rendezvous with various mission designs, 2022.

[142] Gary T. Horowitz and Juan Martin Maldacena. The Black hole final state. JHEP, 02:008, 2004.

[143] Gary T. Horowitz and Donald Marolf. Where is the information stored in black holes? Phys. Rev. D, 55:3654–3663, 1997.

[144] Sabine Hossenfelder. Comment on the black hole firewall. 10 2012.

[145] Sabine Hossenfelder and Lee Smolin. Conservative solutions to the black hole information problem. Phys. Rev. D, 81:064009, 2010.

[146] Veronika E. Hubeny, Mukund Rangamani, and Tadashi Takayanagi. A Covariant holographic entanglement entropy proposal. JHEP, 07:062, 2007.

[147] Man-To Hui, Quan-Zhi Ye, Dora Föhring, Denise Hung, and David J. Tholen. Physical characterization of interstellar comet 2i/2019 q4 (borisov). The Astronomical Journal, 160(2):92, jul 2020.

[148] Dong-il Hwang, Bum-Hoon Lee, Wonwoo Lee, and Dong-han Yeom. Bubble collision with gravitation. JCAP, 07:003, 2012.

[149] P. Ivanov, P. Naselsky, and I. Novikov. Inflation and primordial black holes as dark matter. Phys. Rev. D, 50:7173–7178, 1994.

[150] Chloe James-Turner, Danton P. B. Weil, Anne M. Green, and Edmund J. Copeland. Constraints on the cosmic string loop collapse fraction from primordial black holes. Phys. Rev. D, 101(12):123526, 2020.

[151] Karsten Jedamzik. Primordial black hole formation during the QCD epoch. Phys. Rev. D, 55:5871–5875, 1997.

[152] Ross J. Jennings, James M. Cordes, and Shami Chatterjee. Detecting gravitational scattering of interstellar objects using pulsar timing. The Astrophysical Journal, 889(2):145, feb 2020.

[153] David Jewitt, Jane Luu, Jayadev Rajagopal, Ralf Kotulla, Susan Ridgway, Wilson Liu, and Thomas Augusteijn. Interstellar interloper 1i/2017 u1: Observations from the not and wiyn telescopes. The Astrophysical Journal Letters, 850(2):L36, nov 2017.

[154] David Jewitt and Darryl Z. Seligman. The interstellar interlopers, 2022.

[155] Matthew C. Johnson, Hiranya V. Peiris, and Luis Lehner. Determining the outcome of cosmic bubble collisions in full general relativity. Physical Review D, 85(8), apr 2012.

[156] Matthew C. Johnson, Carroll L. Wainwright, Anthony Aguirre, and Hiranya V. Peiris. Simulating the Universe(s) III: Observables for the full bubble collision spacetime. JCAP, 07:020, 2016.

[157] Samson A. Johnson, Matthew Penny, B. Scott Gaudi, Eamonn Kerins, Nicholas J. Rattenbury, Annie C. Robin, Sebastiano Calchi Novati, and Calen B. Henderson. Predictions of the nancy grace roman space telescope galactic exoplanet survey.

II. free-floating planet detection rates. The Astronomical Journal, 160(3):123, aug 2020.

[158] Kristjan Kannike, Luca Marzola, Martti Raidal, and Hardi Veermäe. Single Field Double Inflation and Primordial Black Holes. JCAP, 09:020, 2017.

[159] M. Karami, A. E. Broderick, S. Rahvar, and M. Reid. Resolving Microlensing Events with Triggered VLBI. Astrophys. J., 833(2):169, 2016.

[160] Bradley J. Kavanagh. bradkav/pbhbounds: Release version, November 2019.

[161] M. Yu. Khlopov and A. G. Polnarev. PRIMORDIAL BLACK HOLES AS A COSMOLOGICAL TEST OF GRAND UNIFICATION. Phys. Lett. B, 97:383–387, 1980.

[162] Claus Kiefer. Aspects of Quantum Black Holes. J. Phys. Conf. Ser., 1612(1):012017, 2020.

[163] Hyoun-Woo Kim, Kyu-Ha Hwang, Andrew Gould, Jennifer C. Yee, Yoon-Hyun Ryu, Michael D. Albrow, Sun-Ju Chung, Cheongho Han, Youn Kil Jung, Chung-Uk Lee, In-Gu Shin, Yossi Shvartzvald, Weicheng Zang, Sang-Mok Cha, Dong-Jin Kim, Seung-Lee Kim, Dong-Joo Lee, Yongseok Lee, Byeong-Gon Park, and Richard W. Pogge. Kmt-2019-blg-2073: Fourth free-floating planet candidate with $\theta_e < 10\mu as$. The Astronomical Journal, 162(1):15, jun 2021.

[164] Seung-Lee Kim, Chung-Uk Lee, Byeong-Gon Park, Dong-Jin Kim, Sang-Mok Cha, Yongseok Lee, Cheongho Han, Moo-Young Chun, and Insoo Yuk. KMTNET:

A Network of 1.6 m Wide-Field Optical Telescopes Installed at Three Southern Observatories. Journal of Korean Astronomical Society, 49(1):37–44, February 2016.

[165] Rain Kipper, Elmo Tempel, and Peeter Tenjes. A method to calculate the local density distribution of the Galaxy from the Tycho-Gaia Astrometric Solution data. Monthly Notices of the Royal Astronomical Society, 473(2):2188–2197, January 2018.

[166] Matthew Kleban and Cameron E. Norton. Monochromatic Mass Spectrum of Primordial Black Holes. 10 2023.

[167] Anatoly Klypin, HongSheng Zhao, and Rachel S. Somerville. LCDM-based models for the Milky Way and M31 I: Dynamical Models, October 2001. arXiv:astro-ph/0110390.

[168] Mrunal Korwar and Stefano Profumo. Updated constraints on primordial black hole evaporation. JCAP, 05:054, 2023.

[169] Naoki Koshimoto, Junichi Baba, and David P. Bennett. A Parametric Galactic Model toward the Galactic Bulge Based on Gaia and Microlensing Data. The Astrophysical Journal, 917(2):78, August 2021. arXiv:2104.03306 [astro-ph].

[170] Naoki Koshimoto, Takahiro Sumi, David P. Bennett, Valerio Bozza, Przemek Mróz, Andrzej Udalski, Nicholas J. Rattenbury, Fumio Abe, Richard Barry, Aparna Bhattacharya, Ian A. Bond, Hirosane Fujii, Akihiko Fukui, Ryusei

Hamada, Yuki Hirao, Stela Ishitani Silva, Yoshitaka Itow, Rintaro Kirikawa, Iona Kondo, Yutaka Matsubara, Shota Miyazaki, Yasushi Muraki, Greg Olmschenk, Clément Ranc, Yuki Satoh, Daisuke Suzuki, Mio Tomoyoshi, Paul J. Tristram, Aikaterini Vandorou, Hibiki Yama, and Kansuke Yamashita. Terrestrial and neptune mass free-floating planet candidates from the moa-ii 9-year galactic bulge survey, 2023.

[171] Chethan Krishnan, Vaishnavi Patil, and Jude Pereira. Page Curve and the Information Paradox in Flat Space. 5 2020.

[172] Alexander Kusenko, Misao Sasaki, Sunao Sugiyama, Masahiro Takada, Volodymyr Takhistov, and Edoardo Vitagliano. Exploring Primordial Black Holes from the Multiverse with Optical Telescopes. Phys. Rev. Lett., 125:181304, 2020.

[173] Alexander Kusenko, Misao Sasaki, Sunao Sugiyama, Masahiro Takada, Volodymyr Takhistov, and Edoardo Vitagliano. Exploring primordial black holes from the multiverse with optical telescopes. Physical Review Letters, 125(18), October 2020.

[174] M. Landgraf, W. J. Baggaley, E. Grün, H. Krüger, and G. Linkert. Aspects of the mass distribution of interstellar dust grains in the solar system from in situ measurements. Journal of Geophysical Research: Space Physics, 105(A5):10343–10352, may 2000.

[175] Luis Lehner. Numerical relativity: a review. Classical and Quantum Gravity, 18(17):R25, aug 2001.

[176] Luis Lehner, Steven L. Liebling, and Oscar Reula. AMR, stability and higher accuracy. Class. Quant. Grav., 23:S421–S446, 2006.

[177] Luis Lehner, David Neilsen, Oscar Reula, and Manuel Tiglio. The discrete energy method in numerical relativity: towards long-term stability. Classical and Quantum Gravity, 21(24):5819–5848, November 2004.

[178] W. Garrett Levine, Aster G. Taylor, Darryl Z. Seligman, Devin J. Hoover, Robert Jedicke, Jennifer B. Bergner, and Gregory P. Laughlin. Interstellar comets from post-main sequence systems as tracers of extrasolar oort clouds, 2023.

[179] H. Lewy, K. Friedrichs, and R. Courant. Über die partiellen differenzengleichungen der mathematischen physik. Mathematische Annalen, 100:32–74, 1928.

[180] Jing Liu, Zong-Kuan Guo, and Rong-Gen Cai. Primordial Black Holes from Cosmic Domain Walls. Phys. Rev. D, 101(2):023513, 2020.

[181] Kinjalk Lochan, Sumanta Chakraborty, and T. Padmanabhan. Information retrieval from black holes. Phys. Rev. D, 94(4):044056, 2016.

[182] Kinjalk Lochan and T. Padmanabhan. Extracting information about the initial state from the black hole radiation. Phys. Rev. Lett., 116(5):051301, 2016.

[183] Torsten Lohne, Alexander V. Krivov, and Jens Rodmann. Long-term collisional evolution of debris disks. The Astrophysical Journal, 673(2):1123, feb 2008.

[184] K. Maeda. Bubble dynamics in the expanding universe. General Relativity and Gravitation, 18(9):931–951, Sep 1986.

[185] Juan Maldacena. Black holes and quantum information. Nature Rev. Phys., 2(3):123–125, 2020.

[186] Juan Martin Maldacena. The Large N limit of superconformal field theories and supergravity. Int. J. Theor. Phys., 38:1113–1133, 1999.

[187] Daniel Malmberg, Melvyn B. Davies, and Douglas C. Heggie. The effects of fly-bys on planetary systems. Monthly Notices of the Royal Astronomical Society, 411(2):859–877, 02 2011.

[188] Donald Marolf. The Black Hole information problem: past, present, and future. Rept. Prog. Phys., 80(9):092001, 2017.

[189] Donald Marolf and Henry Maxfield. Observations of Hawking radiation: the Page curve and baby universes. 10 2020.

[190] Samir D. Mathur. The Information paradox: A Pedagogical introduction. Class. Quant. Grav., 26:224001, 2009.

[191] Samir D. Mathur. What the information paradox is not. 8 2011.

[192] Norihito Matsunaga and Kazuhiro Yamamoto. The finite source size effect and wave optics in gravitational lensing. Journal of Cosmology and Astroparticle Physics, 2006(01):023–023, January 2006.

[193] Thomas A. McGlynn and Robert D. Chapman. On the Nondetection of Extrasolar Comets. apjl, 346:L105, November 1989.

[194] Karen J. Meech, Robert Weryk, Marco Micheli, Jan T. Kleyna, Olivier R. Hainaut, Robert Jedicke, Richard J. Wainscoat, Kenneth C. Chambers, Jacqueline V. Keane, Andreea Petric, Larry Denneau, Eugene Magnier, Travis Berger, Mark E. Huber, Heather Flewelling, Chris Waters, Eva Schunova-Lilly, and Serge Chastel. A brief visit from a red and extremely elongated interstellar asteroid. nat, 552(7685):378–381, December 2017.

[195] K.J. Meech, O.R. Hainaut, and B.G. Marsden. Comet nucleus size distributions from hst and keck telescopes. Icarus, 170(2):463–491, 2004.

[196] Aleksandar R. Mikovic. Unitary theory of evaporating 2-D black holes. Class. Quant. Grav., 13:209–220, 1996.

[197] Aleksandar R. Mikovic. General solution for self-gravitating spherical null dust. Phys. Rev. D, 56:6067–6070, 1997.

[198] Aleksandar R. Mikovic and Voja Radovanovic. Two loop back reaction in 2-D dilaton gravity. Nucl. Phys. B, 481:719–742, 1996.

[199] Núria Miret-Roig. The origin of free-floating planets. Astrophysics and Space Science, 368(3), mar 2023.

[200] Amaya Moro-Martí n. Origin of 1i/'oumuamua. i. an ejected protoplanetary disk object? The Astrophysical Journal, 866(2):131, oct 2018.

[201] Amaya Moro-Martín, Edwin L. Turner, and Abraham Loeb. Will the Large Synoptic Survey Telescope Detect Extra-Solar Planetesimals Entering the Solar System? apj, 704(1):733–742, October 2009.

[202] Amaya Moro-Martín. Origin of 1i/'oumuamua. ii. an ejected exo-oort cloud object? The Astronomical Journal, 157(2):86, feb 2019.

[203] P. Mroz, M. Ban, P. Marty, and R. Poleski. Free-floating or wide-orbit? keck adaptive-optics observations reveal no host stars near free-floating planet candidates, 2023.

[204] P. Mroz and R. Poleski. Exoplanet occurrence rates from microlensing surveys, 2023.

[205] Przemek Mró z, Radosław Poleski, Andrew Gould, Andrzej Udalski, Takahiro Sumi, Michał K. Szymański, Igor Soszyński, Paweł Pietrukowicz, Szymon Kozłowski, Jan Skowron, Krzysztof Ulaczyk, Michael D. Albrow, Sun-Ju Chung, Cheongho Han, Kyu-Ha Hwang, Youn Kil Jung, Hyoun-Woo Kim, Yoon-Hyun Ryu, In-Gu Shin, Yossi Shvartzvald, Jennifer C. Yee, Weicheng Zang, Sang-Mok Cha, Dong-Jin Kim, Seung-Lee Kim, Chung-Uk Lee, Dong-Joo Lee, Yongseok Lee, Byeong-Gon Park, and Richard W. Pogge. A terrestrial-mass rogue planet candidate detected in the shortest-timescale microlensing event. The Astrophysical Journal Letters, 903(1):L11, oct 2020.

[206] Przemek Mró z, Radosław Poleski, Cheongho Han, Andrzej Udalski, Andrew

Gould, Michał K. Szymański, Igor Soszyński, Paweł Pietrukowicz, Szymon Kozłowski, Jan Skowron, Krzysztof Ulaczyk, Mariusz Gromadzki, Krzysztof Rybicki, Patryk Iwanek, Marcin Wrona, Michael D. Albrow, Sun-Ju Chung, Kyu-Ha Hwang, Yoon-Hyun Ryu, Youn Kil Jung, In-Gu Shin, Yossi Shvartzvald, Jennifer C. Yee, Weicheng Zang, Sang-Mok Cha, Dong-Jin Kim, Hyoun-Woo Kim, Seung-Lee Kim, Chung-Uk Lee, Dong-Joo Lee, Yongseok Lee, Byeong-Gon Park, Richard W. Pogge, and and. A free-floating or wide-orbit planet in the microlensing event OGLE-2019-BLG-0551. The Astronomical Journal, 159(6):262, may 2020.

[207] Przemek Mróz, Andrzej Udalski, David P. Bennett, Yoon-Hyun Ryu, Takahiro Sumi, Yossi Shvartzvald, Jan Skowron, Radosław Poleski, Paweł Pietrukowicz, Szymon Kozłowski, Michał K. Szymański, Łukasz Wyrzykowski, Igor Soszyński, Krzysztof Ulaczyk, Krzysztof Rybicki, Patryk Iwanek, Michael D. Albrow, Sun-Ju Chung, Andrew Gould, Cheongho Han, Kyu-Ha Hwang, Youn Kil Jung, In-Gu Shin, Jennifer C. Yee, Weicheng Zang, Sang-Mok Cha, Dong-Jin Kim, Hyoun-Woo Kim, Seung-Lee Kim, Chung-Uk Lee, Dong-Joo Lee, Yongseok Lee, Byeong-Gon Park, Richard W. Pogge, Fumio Abe, Richard Barry, Aparna Bhattacharya, Ian A. Bond, Martin Donachie, Akihiko Fukui, Yuki Hirao, Yoshitaka Itow, Kohei Kawasaki, Iona Kondo, Naoki Koshimoto, Man Cheung Alex Li, Yutaka Matsubara, Yasushi Muraki, Shota Miyazaki, Masayuki Nagakane, Clément Ranc, Nicholas J. Rattenbury, Haruno Suematsu, Denis J. Sullivan, Daisuke Suzuki,

Paul J. Tristram, Atsunori Yonehara, Dan Maoz, Shai Kaspi, and Matan Friedmann. Two new free-floating or wide-orbit planets from microlensing. A&A, 622:A201, February 2019.

[208] Przemek Mróz, Andrzej Udalski, Jan Skowron, Radosław Poleski, Szymon Kozłowski, Michał K. Szymański, Igor Soszyński, Łukasz Wyrzykowski, Paweł Pietrukowicz, Krzysztof Ulaczyk, Dorota Skowron, and Michał Pawlak. No large population of unbound or wide-orbit jupiter-mass planets. Nature, 548(7666):183–186, jul 2017.

[209] Przemek Mróz, Radosław Poleski, Andrew Gould, Andrzej Udalski, Takahiro Sumi, , , Michał K. Szymański, Igor Soszyński, Paweł Pietrukowicz, Szymon Kozłowski, Jan Skowron, Krzysztof Ulaczyk, (OGLE Collaboration), Michael D. Albrow, Sun-Ju Chung, Cheongho Han, Kyu-Ha Hwang, Youn Kil Jung, Hyoun-Woo Kim, Yoon-Hyun Ryu, In-Gu Shin, Yossi Shvartzvald, Jennifer C. Yee, Weicheng Zang, Sang-Mok Cha, Dong-Jin Kim, Seung-Lee Kim, Chung-Uk Lee, Dong-Joo Lee, Yongseok Lee, Byeong-Gon Park, Richard W. Pogge, and (KMT Collaboration). A terrestrial-mass rogue planet candidate detected in the shortest-timescale microlensing event. The Astrophysical Journal Letters, 903(1):L11, oct 2020.

[210] Przemek Mróz, Y.-H. Ryu, J. Skowron, A. Udalski, A. Gould, M. K. Szymański, I. Soszyński, R. Poleski, P. Pietrukowicz, S. Kozłowski, M. Pawlak, K. Ulaczyk, (The OGLE Collaboration), M. D. Albrow, S.-J. Chung, Y. K. Jung, C. Han, K.-

H. Hwang, I.-G. Shin, J. C. Yee, W. Zhu, S.-M. Cha, D.-J. Kim, H.-W. Kim, S.-L. Kim, C.-U. Lee, D.-J. Lee, Y. Lee, B.-G. Park, R. W. Pogge, and (The KMTNet Collaboration). A neptune-mass free-floating planet candidate discovered by microlensing surveys. The Astronomical Journal, 155(3):121, feb 2018.

[211] Takahiro T. Nakamura and Shuji Deguchi. Wave Optics in Gravitational Lensing. Progress of Theoretical Physics Supplement, 133:137–153, January 1999.

[212] Hiroko Niikura et al. Microlensing constraints on primordial black holes with Subaru/HSC Andromeda observations. Nature Astron., 3(6):524–534, 2019.

[213] Hiroko Niikura, Masahiro Takada, Naoki Yasuda, Robert H. Lupton, Takahiro Sumi, Surhud More, Toshiki Kurita, Sunao Sugiyama, Anupreeta More, Masamune Oguri, and Masashi Chiba. Microlensing constraints on primordial black holes with the Subaru/HSC Andromeda observation. Nature Astronomy, 3(6):524–534, June 2019. arXiv: 1701.02151.

[214] Hiroko Niikura, Masahiro Takada, Shuichiro Yokoyama, Takahiro Sumi, and Shogo Masaki. Constraints on earth-mass primordial black holes from OGLE 5-year microlensing events. Physical Review D, 99(8), apr 2019.

[215] Hiroko Niikura, Masahiro Takada, Shuichiro Yokoyama, Takahiro Sumi, and Shogo Masaki. Constraints on Earth-mass primordial black holes from OGLE 5-year microlensing events. Phys. Rev. D, 99(8):083503, 2019.

[216] Yasunori Nomura. Interior of a unitarily evaporating black hole. Phys. Rev. D, 102(2):026001, 2020.

[217] S. Calchi Novati. Pixel lensing. General Relativity and Gravitation, 42(9):2101–2126, dec 2009.

[218] S. Calchi Novati, V. Bozza, F. De Paolis, M. Dominik, G. Ingrosso, Ph Jetzer, L. Mancini, A. Nucita, G. Scarpetta, M. Sereno, F. Strafella, and A. Gould. CANDIDATE MICROLENSING EVENTS FROM M31 OBSERVATIONS WITH THE LOIANO TELESCOPE. The Astrophysical Journal, 695(1):442, March 2009. Publisher: The American Astronomical Society.

[219] B. Paczynski. Gravitational Microlensing at Large Optical Depth. ApJ, 301:503, February 1986.

[220] Don N. Page. IS BLACK HOLE EVAPORATION PREDICTABLE? Phys. Rev. Lett., 44:301, 1980.

[221] Don N. Page. Average entropy of a subsystem. Phys. Rev. Lett., 71:1291–1294, 1993.

[222] Don N. Page. Information in black hole radiation. Phys. Rev. Lett., 71:3743–3746, 1993.

[223] Don N. Page. Time Dependence of Hawking Radiation Entropy. JCAP, 09:028, 2013.

[224] Geoffrey Penington. Entanglement Wedge Reconstruction and the Information Paradox. JHEP, 09:002, 2020.

[225] M. T. Penny, E. Kerins, N. Rattenbury, J.-P. Beaulieu, A. C. Robin, S. Mao, V. Batista, S. Calchi Novati, A. Cassan, P. Fouqué, I. McDonald, J. B. Marquette, P. Tisserand, and M. R. Zapatero Osorio. ExELS: an exoplanet legacy science proposal for the ESA Euclid mission – I. Cold exoplanets. Monthly Notices of the Royal Astronomical Society, 434(1):2–22, 07 2013.

[226] Matthew T. Penny, B. Scott Gaudi, Eamonn Kerins, Nicholas J. Rattenbury, Shude Mao, Annie C. Robin, and Sebastiano Calchi Novati. Predictions of the WFIRST Microlensing Survey I: Bound Planet Detection Rates. The Astrophysical Journal Supplement Series, 241(1):3, February 2019. arXiv:1808.02490 [astro-ph].

[227] Joseph Polchinski. String theory and black hole complementarity. In STRINGS 95: Future Perspectives in String Theory, pages 417–426, 7 1995.

[228] Joseph Polchinski. The Black Hole Information Problem. In Theoretical Advanced Study Institute in Elementary Particle Physics: New Frontiers in Fields and Strings, pages 353–397, 2017.

[229] John Preskill. Do black holes destroy information? In International Symposium on Black holes, Membranes, Wormholes and Superstrings, pages 22–39, 1 1992.

[230] K. Pruett, W. Dawson, M. S. Medford, C. Lam, J. R. Lu, N. Golovich, and G. Chapline. Primordial Black Hole Dark Matter Simulations Using PopSyCLE, November 2022. arXiv:2211.06771 [astro-ph].

[231] Lisa Randall, Marin Soljacic, and Alan H. Guth. Supernatural inflation: Inflation from supersymmetry with no (very) small parameters. Nucl. Phys. B, 472:377–408, 1996.

[232] Frederic A. Rasio and Eric B. Ford. Dynamical instabilities and the formation of extrasolar planetary systems. Science, 274(5289):954–956, 1996.

[233] I. H. Redmount. Blue-Sheet Instability of Schwarzschild Wormholes. Progress of Theoretical Physics, 73(6):1401–1426, June 1985.

[234] Carlo Rovelli. The Subtle Unphysical Hypothesis of the Firewall Theorem. Entropy, 21(9):839, 2019.

[235] Sergei G. Rubin, Alexander S. Sakharov, and Maxim Yu. Khlopov. The Formation of primary galactic nuclei during phase transitions in the early universe. J. Exp. Theor. Phys., 91:921–929, 2001.

[236] Jorge G. Russo. The Information problem in black hole evaporation: Old and recent results. In 27th Spanish Relativity Meeting: Beyond General Relativity (ERE 2004), 1 2005.

[237] Shinsei Ryu and Tadashi Takayanagi. Holographic derivation of entanglement entropy from AdS/CFT. Phys. Rev. Lett., 96:181602, 2006.

[238] Yoon-Hyun Ryu, Przemek Mróz, Andrew Gould, Kyu-Ha Hwang, Hyoun-Woo Kim, Jennifer C. Yee, Michael D. Albrow, Sun-Ju Chung, Youn Kil Jung, In-Gu Shin, Yossi Shvartzvald, Weicheng Zang, Sang-Mok Cha, Dong-Jin Kim, Seung-Lee Kim, Chung-Uk Lee, Dong-Joo Lee, Yongseok Lee, Byeong-Gon Park, Cheongho Han, Richard W. Pogge, KMTNet Collaboration, Andrzej Udalski, Radek Poleski, Jan Skowron, Michał K. Szymański, Igor Soszyński, Paweł Pietrukowicz, Szymon Kozłowski, Krzysztof Ulaczyk, Krzysztof A. Rybicki, Patryk Iwanek, and OGLE Collaboration. KMT-2017-BLG-2820 and the Nature of the Free-floating Planet Population. aj, 161(3):126, March 2021.

[239] J.C. Schindler and A. Aguirre. Algorithms for the explicit computation of Penrose diagrams. Class. Quant. Grav., 35(10):105019, 2018.

[240] Joseph Schindler, Dominik Šafránek, and Anthony Aguirre. Entanglement entropy from coarse-graining in pure and mixed multipartite systems. arXiv e-prints, page arXiv:2005.05408, May 2020.

[241] Joseph C. Schindler, Anthony Aguirre, and Amita Kuttner. Understanding black hole evaporation using explicitly computed Penrose diagrams. Phys. Rev. D, 101(2):024010, 2020.

[242] F. W. Scholz and M. A. Stephens. K-sample anderson-darling tests. Journal of the American Statistical Association, 82(399):918–924, 1987.

[243] Darryl Seligman and Gregory Laughlin. Evidence that 1i/2017 u1 ('oumuamua) was composed of molecular hydrogen ice. The Astrophysical Journal Letters, 896(1):L8, jun 2020.

[244] A. K. Sen and N. C. Rana. On the missing interstellar comets. A&A, 275:298, August 1993.

[245] Amir Siraj and Abraham Loeb. Probing Extrasolar Planetary Systems with Interstellar Meteors. arXiv e-prints, page arXiv:1906.03270, June 2019.

[246] Amir Siraj and Abraham Loeb. The 2019 discovery of a meteor of interstellar origin, 2022.

[247] Nolan Smyth, Stefano Profumo, Samuel English, Tesla Jeltema, Kevin McKinnon, and Puragra Guhathakurta. Updated Constraints on Asteroid-Mass Primordial Black Holes as Dark Matter. Phys. Rev. D, 101(6):063005, 2020.

[248] Nolan Smyth, Stefano Profumo, Samuel English, Tesla Jeltema, Kevin McKinnon, and Puragra Guhathakurta. Updated Constraints on Asteroid-Mass Primordial Black Holes as Dark Matter. Physical Review D, 101(6):063005, March 2020. arXiv:1910.01285 [astro-ph, physics:hep-th].

[249] C. Snodgrass, A. Fitzsimmons, S. C. Lowry, and P. Weissman. The size distribu-

tion of Jupiter Family comet nuclei. Monthly Notices of the Royal Astronomical Society, 414(1):458–469, 06 2011.

[250] Mark Srednicki. Entropy and area. Phys. Rev. Lett., 71:666–669, 1993.

[251] Christopher R. Stephens, Gerard 't Hooft, and Bernard F. Whiting. Black hole evaporation without information loss. Class. Quant. Grav., 11:621–648, 1994.

[252] Veerle J. Sterken, Andrew J. Westphal, Nicolas Altobelli, David Malaspina, and Frank Postberg. Interstellar Dust in the Solar System. ssr, 215(7):43, October 2019.

[253] Ovidiu Cristinel Stoica. Revisiting the black hole entropy and the information paradox. Adv. High Energy Phys., 2018:4130417, 2018.

[254] Louis E. Strigari, Matteo Barnabè , Philip J. Marshall, and Roger D. Blandford. Nomads of the galaxy. Monthly Notices of the Royal Astronomical Society, 423(2):1856–1865, may 2012.

[255] Andrew Strominger. Unitary rules for black hole evaporation. In 7th Marcel Grossmann Meeting on General Relativity (MG 7), pages 59–74, 10 1994.

[256] Sunao Sugiyama, Toshiki Kurita, and Masahiro Takada. Revisiting the wave optics effect on primordial black hole constraints from optical microlensing search. arXiv:1905.06066 [astro-ph], May 2019. arXiv: 1905.06066.

[257] Takahiro Sumi, Naoki koshimoto, David P. Bennett, Nicholas J. Rattenbury, Fumio Abe, Richard Barry, Aparna Bhattacharya, Ian A. Bond, Hirosane Fujii, Akihiko Fukui, Ryusei Hamada, Yuki Hirao, Stela Ishitani Silva, Yoshitaka Itow, Rintaro Kirikawa, Iona Kondo, Yutaka Matsubara, Shota Miyazaki, Yasushi Muraki, Greg Olmschenk, Clement Ranc, Yuki Satoh, Daisuke Suzuki, Mio Tomoyoshi, Paul . J. Tristram, Aikaterini Vandorou, Hibiki Yama, and Kansuke Yamashita. Free-floating planet mass function from moa-ii 9-year survey towards the galactic bulge, 2023.

[258] Leonard Susskind, Larus Thorlacius, and John Uglum. The Stretched horizon and black hole complementarity. Phys. Rev. D, 48:3743–3761, 1993.

[259] Gerard 't Hooft. The Scattering matrix approach for the quantum black hole: An Overview. Int. J. Mod. Phys. A, 11:4623–4688, 1996.

[260] A. Tamm, E. Tempel, P. Tenjes, O. Tihhonova, and T. Tuvikene. Stellar mass map and dark matter distribution in M 31. Astronomy & Astrophysics, 546:A4, October 2012.

[261] David E. Trilling, Tyler Robinson, Alissa Roegge, Colin Orion Chandler, Nathan Smith, Mark Loeffler, Chad Trujillo, Samuel Navarro-Meza, and Lori M. Glaspie. Implications for planetary system formation from interstellar object 1i/2017 u1 ('oumuamua). The Astrophysical Journal, 850(2):L38, nov 2017.

[262] A. Udalski, M. K. Szymański, and G. Szymański. Ogle-iv: Fourth phase of the optical gravitational lensing experiment, 2015.

[263] William G. Unruh and Robert M. Wald. Information Loss. Rept. Prog. Phys., 80(9):092002, 2017.

[264] J. Vaubaillon. Hyperbolic meteors: is CNEOS 2014-01-08 interstellar? WGN, Journal of the International Meteor Organization, 50(5):140–143, October 2022.

[265] Dominik Šafránek, J. M. Deutsch, and Anthony Aguirre. Quantum coarse-grained entropy and thermalization in closed systems. pra, 99(1):012103, January 2019.

[266] Dominik Šafránek, J. M. Deutsch, and Anthony Aguirre. Quantum coarse-grained entropy and thermodynamics. pra, 99(1):010101, January 2019.

[267] Carroll L. Wainwright. Cosmotransitions: Computing cosmological phase transition temperatures and bubble profiles with multiple fields. Computer Physics Communications, 183(9):2006–2013, 2012.

[268] Carroll L. Wainwright, Matthew C. Johnson, Anthony Aguirre, and Hiranya V. Peiris. Simulating the universe(s) II: phenomenology of cosmic bubble collisions in full General Relativity. JCAP, 10:024, 2014.

[269] Carroll L. Wainwright, Matthew C. Johnson, Hiranya V. Peiris, Anthony Aguirre, Luis Lehner, and Steven L. Liebling. Simulating the universe(s): from cosmic bubble collisions to cosmological observables with numerical relativity. Journal of Cosmology and Astroparticle Physics, 2014(03):030–030, March 2014.

[270] David Wallace. Why Black Hole Information Loss is Paradoxical, pages 209–236. 4 2020.

[271] Harrison Winch, Jack Setford, Jo Bovy, and David Curtin. Using LSST Microlensing to Constrain Dark Compact Objects in Spherical and Disk Configurations. The Astrophysical Journal, 933(2):177, July 2022.

[272] Hans J. Witt and Shude Mao. Can lensed stars be regarded as pointlike for microlensing by MACHOs? The Astrophysical Journal, 430:505–510, August 1994.

[273] R. L. Workman et al. Review of Particle Physics. PTEP, 2022:083C01, 2022.

[274] Zhong-Chao Wu. GRAVITATIONAL EFFECTS IN BUBBLE COLLISIONS. Phys. Rev. D, 28:1898–1906, 1983.

[275] L. Wyrzykowski et al. The OGLE View of Microlensing towards the Magellanic Clouds. III. Ruling out sub-solar MACHOs with the OGLE-III LMC data. Mon. Not. Roy. Astron. Soc., 413:493, 2011.

[276] L. Wyrzykowski et al. The OGLE View of Microlensing towards the Magellanic Clouds. IV. OGLE-III SMC Data and Final Conclusions on MACHOs. Mon. Not. Roy. Astron. Soc., 416:2949, 2011.

[277] Jun'ichi Yokoyama. Chaotic new inflation and formation of primordial black holes. Phys. Rev. D, 58:083510, 1998.

[278] W.H. Zurek. Entropy Evaporated by a Black Hole. Phys. Rev. Lett., 49:1683–1686, 1982.